Differential Interferometry on Valsamiotis Dam Area (Chania Prefecture, Crete) Using SENTINEL-1 Synthetic Aperture Radar (SAR) data

by Sotirios Panagou

Chania 2019

Hellenic Mediterranean University

Department of Electronic Engineering

(for the Department of Environmental & Natural Resources Engineering)

Master of Science in GeoEnvironmental Risks and Resources

Differential Interferometry on Valsamiotis Dam Area (Chania Prefecture, Crete) Using SENTINEL-1 Synthetic Aperture Radar (SAR) data

Sotirios Panagou

Committee

Dr. Maria Kouli (Supervisor)

Dr. Antonio Pepe

Dr. Filippos Vallianatos

Chania, 2019

Index

Abstract

In this work, Sentinel-1 (S1) imagery and SAR interferometry techniques were used for dam monitoring purposes. The aforementioned method was applied in the study-area of the Valsamiotis dam, located in the prefecture of Chania, Crete. The Valsamiotis dam probable deformation was calculated since the whole structure undergoes severe problems. The ground deformation at several points of the dam was measured for a time period of 18 months while it was correlated to water level variations. European Space Agency (ESA) satellite with radar capabilities Sentinel-1 was chosen, due to its mapping capacity and acquisition, namely Terrain Observation by Progressive Scans (TOPS). Sentinel-1 is composed of two radar units S1A and S1B, and the SAR satellite images are provided for free from their online platform Copernicus. SAR images allows a vast range of geophysical applications to be performed, such as mapping of surface deformation (e.g. caused by tectonic processes, landslides, ground subsidence). Interferometry (InSAR) techniques exploit the radar phase difference between two different SAR images forming an interferometric pair.

Differential SAR interferometry (D-InSAR) is used for the generation of the map of deformation which occurs in the temporal time period between the two flight passes of the sensors on the same area. More recently, DInSAR is improved to allow the generation of time-series of deformation by combining the information embedded in sequences of DInSAR interferograms spanning a chosen time-period.

With D-InSAR methodology and techniques advancing, there are two main approaches in the differential sequence; Persistent scatterers interferometry (PSI) and small baseline (SB) technique. PSI uses a dominant scatterer (single master for co-registration and interferogram formation) and exploits the full resolution of the SAR image, while SB uses different targets with small baseline, allowing for the usage of more ground points in urban and rural areas which can be monitored (multiple master strategy).

Abstract

This work is organized as follows:

- Chapter I – Introduction to the Study area and SAR, brief introduction on the S1-TOPS and its capabilities, SAR basics and image formation, presentation of the InSAR estimation for topography.

- Chapter II – D-InSAR methodology is used to calculate the difference in the topography by using a set of multiple interferograms. This method is using complex mathematics used in chain for the calculation of the deformations present in the topography. This chapter presents the involved procedures.

- Chapter III – Phase Unwrapping (PhU) procedure for the recovery of the full phase from the D-InSAR pairs and the SB technique.

- Chapter IV – The products of the techniques presented in the above chapters were used on the study. For this purpose, several data sets over the course of 2017-2018 are investigated.

- Chapter V – The deformation time-series and water level and volume changes are presented in this chapter.

- Chapter VI – Discussion and Conclusions.

Chapter 1

1.1 Dam Monitoring

Monitoring of large water reservoirs is a common practice that is used from the government agencies and/or companies that are responsible for them. There are well-established monitoring approaches ranging from continuous instrumental monitoring to simple visual inspection, such as:

- Seismicity monitoring
- Embankment temperature monitoring
- Inverted and simple pendulums responsible for the monitoring of the dam's displacement
- Water level monitoring
- Measuring devices for provision infiltration
- Embankment temperature monitoring devices
- Pressure monitoring devices in joints
- Triaxial measuring instruments for joints and perimeter cracks (internal), VINCHON type
- Vertical foundation displacement measuring instruments

The water level of those reservoirs can significantly change over the course of a single year, depending on the water demand for agricultural use or for water supply. Due to the change of the water level, the crust is subject to periodic loading and unloading that can lead to pore pressure and may result on unloading the resulting stress to underlying fractures or nearby faults.

The ground deformation of a water reservoir's can either be measured (i) on specific points with leveling or Global Navigation Satellite Systems GNSS. Or (ii) in a spatially

continuous manner by Differential Synthetic Aperture Radar Interferometry (DInSAR). The latter measures the resulting ground deformation with an accuracy of a few millimeters. Due to DInSAR archives available from the early 1990's (several SAR satellites), the measurement results can offer a detailed documentation of ground deformations through the time-series calculation which can show if a trend in the ground deformation is recurring or unique.

1.2 Area of Interest – Valsamiotis dam

Valsamiotis dam is located in the Keritis Waterbasin (figure 1) in the municipality of Chania, Crete. Although a lot of studies were conducted before the construction of the dam, regarding the geology, seismicity, type of construction materials to be used and technical construction, the Valsamiotis dam is facing a lot of problems since the start of its operation. These problems resulted in severe financial losses due to the repairing projects. There are a lot of well documented articles in both the local and national newspapers about those problems and the projects that took and are taking place to amend the situation and repair them.

The dam building project (figure 2) was carried out by the Cretan Development Agency (https://oakae.gr/). The project was finished in the start of 2014 and the dam started its operation in March 2014. The dam collects the surplus of water from the natural springs of Meskla and from the torrents created by rainfalls. Its purpose is the supply of water in the broader area of Chania, for agricultural use or supplying water in the rural areas at times of drought. The potential capacity of the dam is estimated at 6 million m^3 of water. The dam is connected, through a pipeline of total length of 3.52 km, to the main pipeline of Agia-Mylonianon-Meskla.
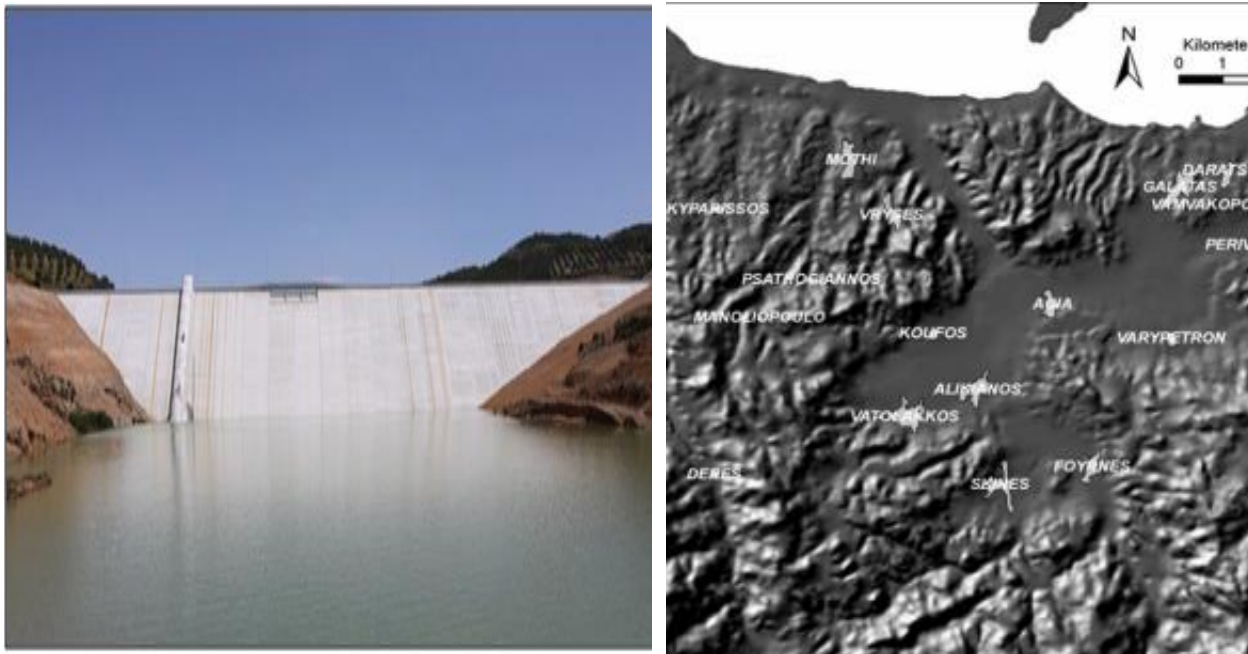
Figure 1. Left image: Valsamiotis Dam (Source: Cretan Development Agency). Right image: Keritis Basin [1].

Table 1.1. Valsamiotis Dam Characteristics and Dimensions

Total Length in the upper area	335m
Height	67.20m
Maximum level of water	+190
Total width in the lowest area	80m
Potential capacity	6 million m^3
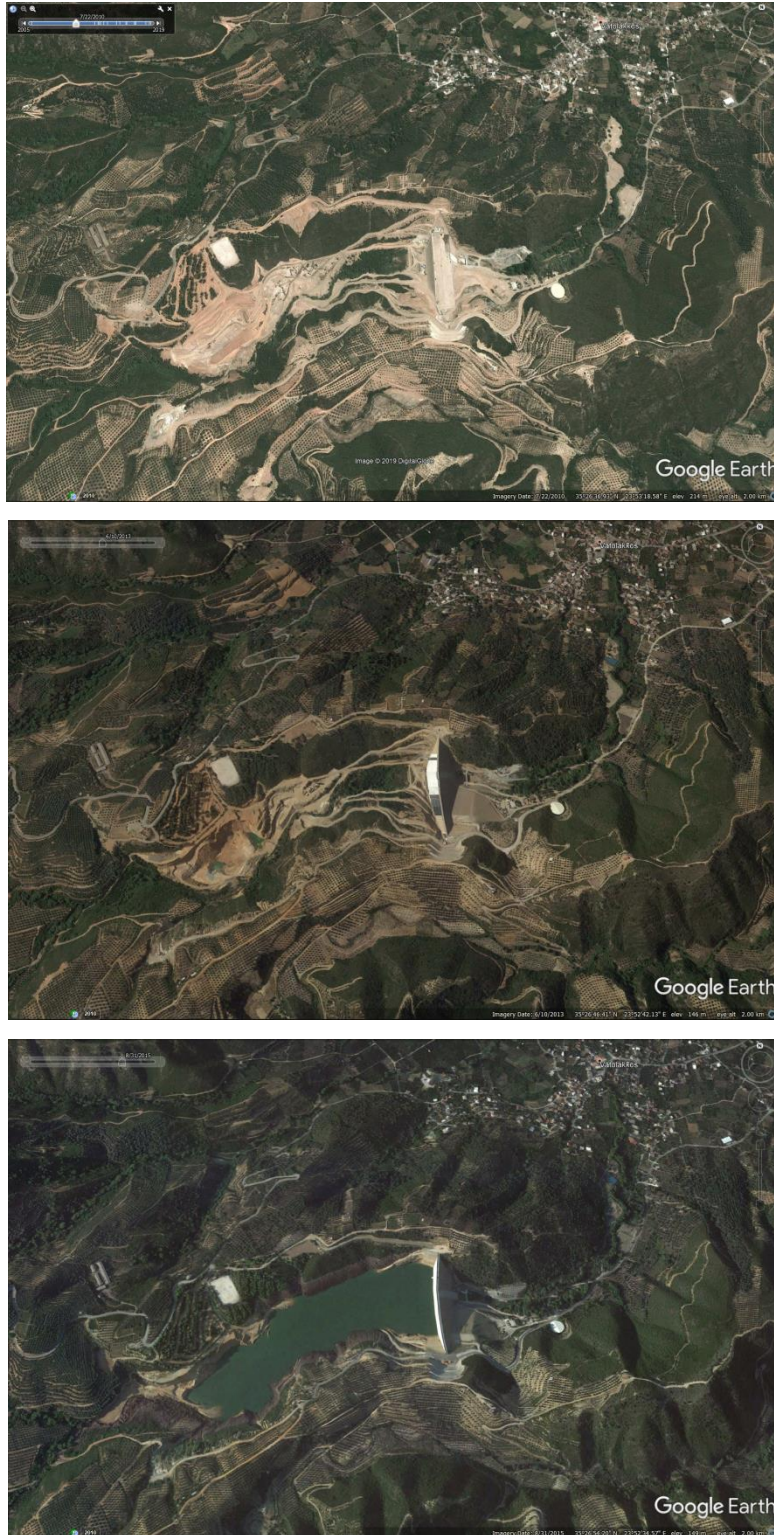
Figure 2. Top image: dam construction area (2005). Middle image: completed dam structure (2013). Bottom image: Valsamiotis dam at the starting months of its operation (April 2015). (Source: Google Earth).

Figure 3. Top: Representation of the Hydro-lithological map of the Keritis Basin. The black rectangle represents the Valsamiotis dam and its broadened area (modified from [1]). Bottom: Geological map of the Valsamiotis Dam and its broadened area.

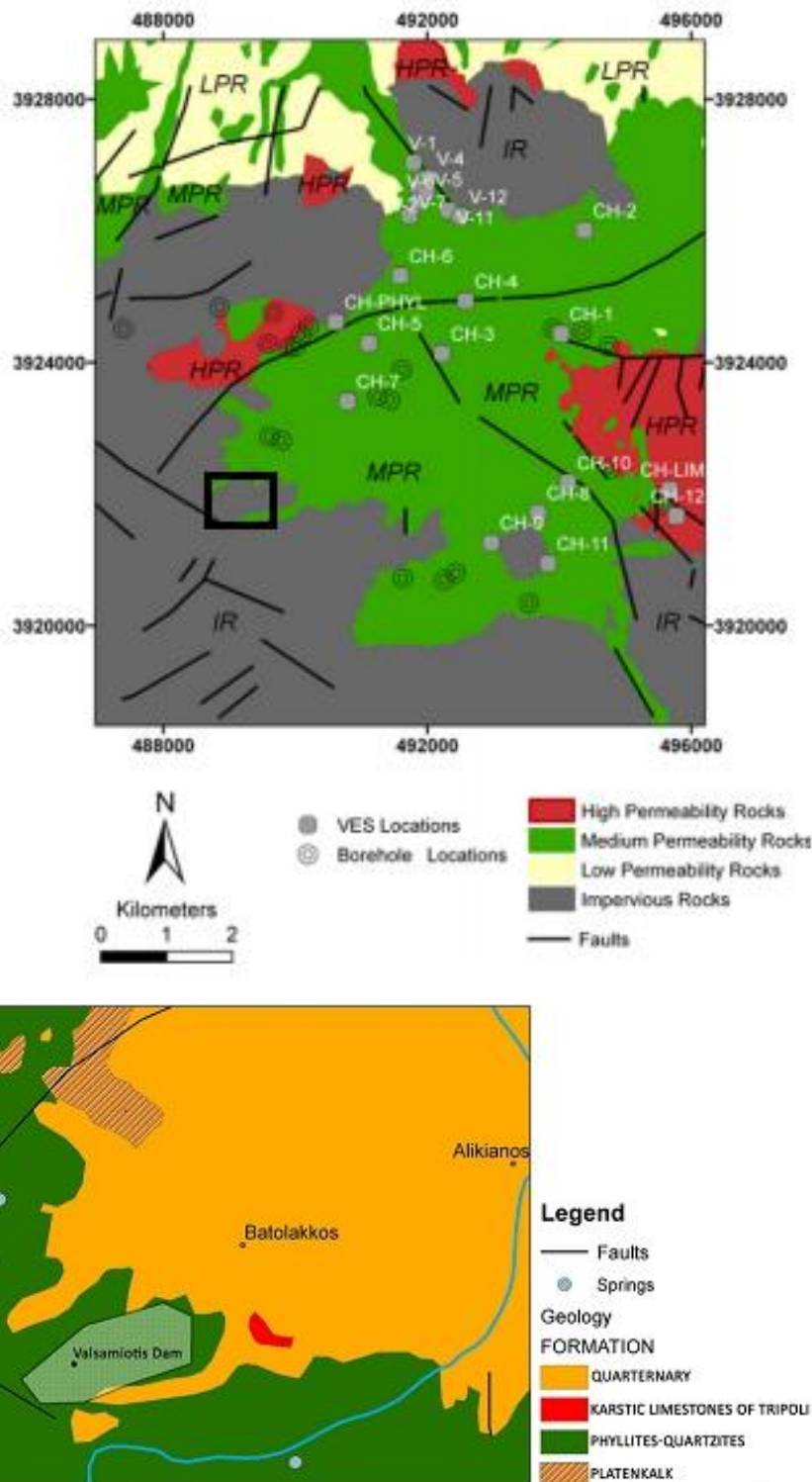The Keritis Basin presents an interesting geotectonic and hydro-lithological context (figure 3). The larger part of the area consists of Quaternary deposits, medium permeability rocks with a direction from North to South. The southwestern and southeastern part of the area is dominated by the presence of dissected hills of phyllites and quartzites, which are Late Carboniferous to Late Triassic package sedimentary rocks that are hydro-geologically characterized as impervious rocks. There is also a small area covered by the high permeability rocks of the karstic Triassic limestones of Tripolis and Trypalion nappes. Close to the central area there is a small occurrence of Platenkalk formation (finely grained limestone), which is also characterized by high permeability.

Concerning its seismicity, Valsamiotis dam is located in one of the most active seismically active regions due to the subduction of the African lithosphere beneath the Aegean lithosphere and is characterized by major seismic events. The collision between the African and Eurasian plates has uplifted Crete about 2–3 km in the last 13 m.y. This uplift continues today as is shown by the uplifted marine sediments of the Last Interglacial and Late Holocene shorelines [2, 6-7]. In general, the western part of Crete seems to behave as a rigid block because faulting is rather limited [3-4]. The faults that have and are developed on land vary from small to 20 km long segments, which in turn is considered one of the most unique tectonic features. A mega-earthquake equivalent to an Mw 8.3–8.5 event [5] struck the west Chania area on July 21, 365AD which is probably the strongest historical European event. According to historical and archeological evidence, the earthquake and the tsunami triggered after the shock destroyed many cities, inundated coastal sites (from Alexandria to the Sicily) and caused numerous fatalities. During the operation period of the Valsamiotis dam there was not recorded any major earthquake.
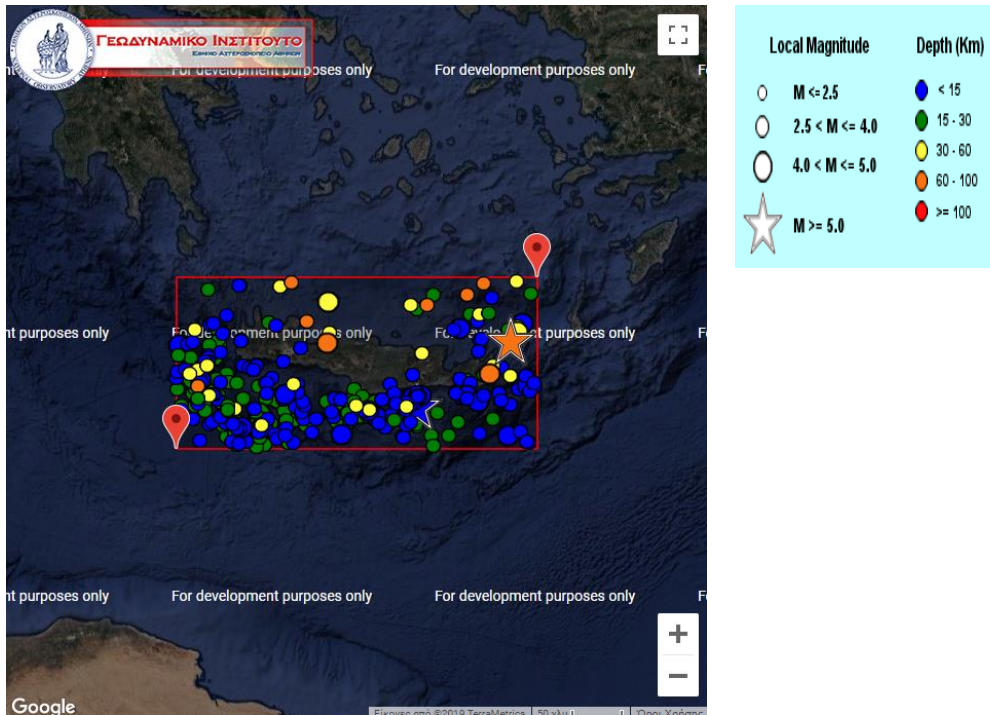
Figure 4. Earthquake activity on the island of Crete between January 2017 and January 2019 (Source: Geodynamic Institute of National Athens Observatory).

The purpose of this thesis is to (i) investigate the existence of probable deformation that affected the dam and its broadened area in the timespan between June 2017 and December 2018, (ii) measure the deformation, (iii) compare the measured deformation and its variations with the historical monthly volume fluctuations since information of the total volume for the full range of water levels was provided from Cretan Development Agency (https://oakae.gr/) between 2017 and 2018.

1.3 Sentinel-1

Sentinel-1 is the first of ESA's Copernicus Programme, which comprises the constellation of two polar-orbiting satellites and are part of GMES (Global Monitoring for Environment and Security). Alongside, Sentinel-2 and -3, they contribute to the GEOSS (Global Earth Observation System of Systems). The Sentinel-1 mission is to provide imaging radar data continuously in all-weather, day-and-night situations. For this purpose, the twin satellites, -1A and -1B, are both fitted with a C-band synthetic aperture radar that transmits at the microwave frequency of 5.405 GHz with a frequency accuracy of 1 dB. They operate at incidence angles between 20° and 45°, and are able to provide a wide variety of polarization (VV+VH, HH+HV, HH, VV).

Figure 5. Sentinel-1 (Source: ESA).

Sentinel-1 has two operation goals, the primary is the coverage of land and the secondary is the coverage of oceans. The coverage is carried by a wide swath (250km) with high radiometric as well as geometric resolutions. The data can be acquired in four different modes. The Stripmap mode (SM), where the illumination of the fixed (both in azimuth

and in elevation) area is done with a continuous sequence of pulses, the Interferometric Wide Swath (IW), data is acquired in three sub-swaths through the TOPSAR (Terrain Observation with Progressive Scanning SAR) technique, the Extra Wide Swath (EW), where data is acquired in five different sub-swaths (larger area coverage with smaller spatial resolution), and the wave mode (WV), where data is acquired in smaller stripmap scenes and is mainly used for the coverage of open oceans. The data products of Sentinel-1 are distributed by ESA, with free access to the public by their platform Copernicus, in the following formats:

- Level-0 data (raw)
- Level-1 data, Single-Look Complex (SLC), complex imagery with amplitude and phase
- Level-1 data, Ground Range Detected (GRD), multi-looked intensity only
- Level-2 data, Ocean (OCN), used for the retrieval of geophysical parameters of the ocean

In the context of this thesis, Level-1 SLC data acquired through the interferometric wide swatch (IW) mode, were used. As stated above, this mode uses the novel TOPSAR mode that provides imaging through three sub-swaths with a total swath width of 250 km. The Sentinel-1 system provides repeat-pass interferometry in the medium resolution (C-Band) area, with the repeat cycle of each satellite of the constellation being 12-days but when working together the repeat-cycle time is reduced to 6-days. [8]. The repeat-cycle is significantly reduced from the previous satellites of the European Space Agency, from 35 days of ERS-1 and ERS-2 and the 30/35 days for the ENVISAT. The small repeat cycle along with the temporal sampling provided by the twin-satellites provide a wide range for geophysical applications and land coverage. The small ground-track strategy of 120 m result in small orbital InSAR baselines on the order of 150m [9].
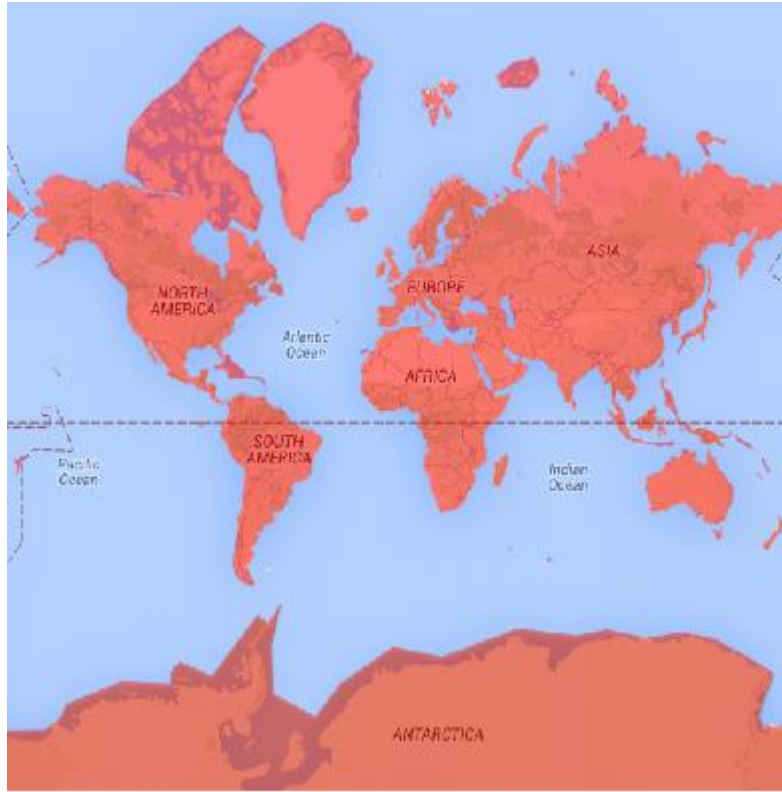
Figure 6. Land Coverage of Sentinel-1. (Source: ESA).

Table 1.2 Sentinel-1A/1B Characteristics

Launch	Sentinel-1A was launched on 3 April 2014 Sentinel-1B was launched on 25 April 2016
Lifetime	7 years
Orbit	Near polar (98.18°), sun-synchronous 693 km orbit height

Orbit cycle	Each one has a 12-day cycle
	Working together they provide
	6-day cycle
Dimensions	3.9m x 2.6m x 2.5m
Launch Mass	2.300 kg
	3-axis altitude stabilization

1.4 SAR Interferometry

1.4.1 SAR History

Synthetic Aperture Radar (SAR), was first developed in the 1950's, as a solution for 24-hour all-weather aerial remote surveillance device. By using microwave remote sensing system, the SAR devices could see through clouds at any hour of the day, but the size needed for the SAR device to be effective would have to be really large. In 1954, Carl Wiley [10] observed that each object in the radar beam has a different speed relative to the antenna, thus each object has its own "Doppler shift", which meant that an antenna a meter or so could acquire an image through beam-sharpening. This observation led to the rapid development of SAR system designs and its application.

The first step in satellite SAR missions began in 1974, when Jet Propulsion Laboratories (JPL) and National Oceanic and Atmospheric Administration (NOAA) started exploring the possibilities for SAR oceanic observations from a satellite. From this collaboration, the first satellite with SAR capabilities, SEASAT, was launched in June 1978. SEASAT operated since October 1978 and although it was first designed for oceanic applications, it provided SAR data for Earth observation interferometry analysis [11-12]. Due to the data obtained from the SEASAT mission, Goldstein and Zebker demonstrated the topographic mapping capabilities of SAR [13], while Gabriel et al. the detection and mapping of small

elevation changes [14]. Despite the short-lived SEASAT mission, in 1981 and 1984, two variations of the model, SIR-A and SIR-B (Shuttle Imaging Radar), were launched operating at L-Band (low frequency) and HH (horizontal transmit and horizontal receive) polarization. The expansion of SAR-satellite missions came in the 1990's. Five Earth-oriented SAR-satellites were launched with the addition of NASA's Magellan SAR oriented on the mapping of Venus. The next step on SAR missions, came with the launch of the novel radar system, named SIR-C [15], which was developed from JPL, ASI (Italian Space Agency) and DLR (German Aerospace Centre). It operated in three different sequences (L-band, C-band, X-band), while transmitting and receiving at both horizontal and vertical polarizations. The breakthrough in SAR interferometry and SAR satellite missions, came with the launch of the twin European ERS-1/2 (European Remote Sensing Satellite) in 1991 and 1995 respectively [16], due to the stability and calibration achieved the most with SAR in respect to the interferometry aspect. In 1992 and 1995, Japan and Canada launched their own SAR systems (JERS and Radarsat).

In the period between 2000 and 2010, Canada launched its second SAR system (Radarsat-2), and alongside with Italian Cosmos-Skymed, Japan's Advanced Land Observing Satellite (ALOS) and DLR's TerraSAR-X, represented the growth and evolution of the first SAR missions, embodying novel features such as high resolution and polarimetry among other features. The newer additions to the SAR-satellite missions came with the launch of ESA's Sentinel-1a in 2014 and Sentinel-1b in 2016, which featured a novel system of antenna-installment; Terrain Observation by Progressive Scans (TOPS).
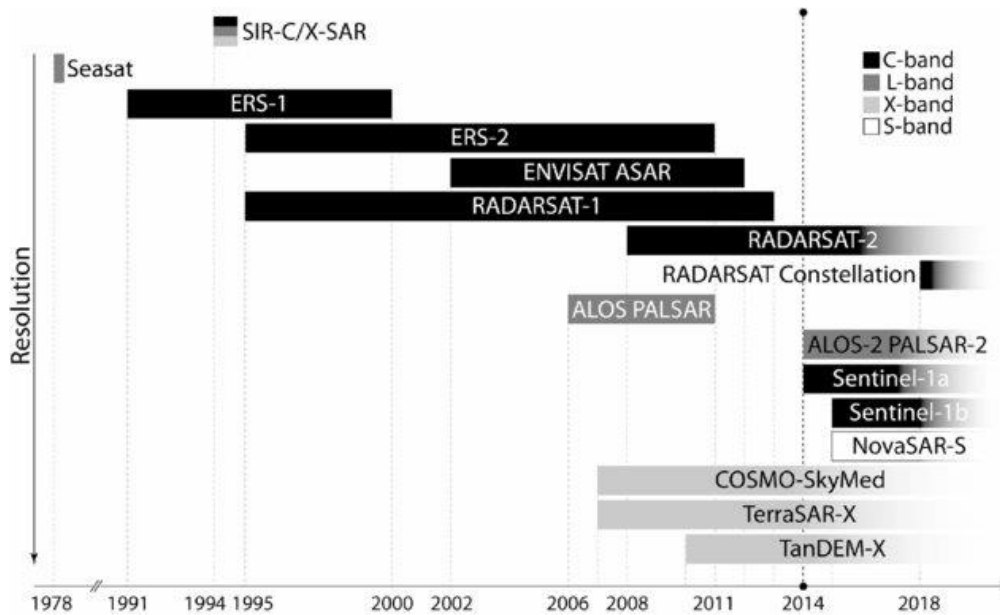
Figure 7. SAR-Satellite missions, historical and ongoing [17].

1.4.2 Basic Principles

Synthetic Aperture Radar uses the same principles of a conventional radar. It transmits electromagnetic waves and collects the backscattering echo (figure 8). After the measurement of the time delay between the transmitted wave and the receiving echoes, it is able to calculate the distance (slant range) between the antenna along the flight path (azimuth) and the ground target. The ability of the radar to properly distinguish two objects, characterizes its spatial resolution. If the two objects are sufficiently separated, each one will be located in a different resolution cell, if not then the radar returns a complex resolution of the backscattering echo (reflected energy).
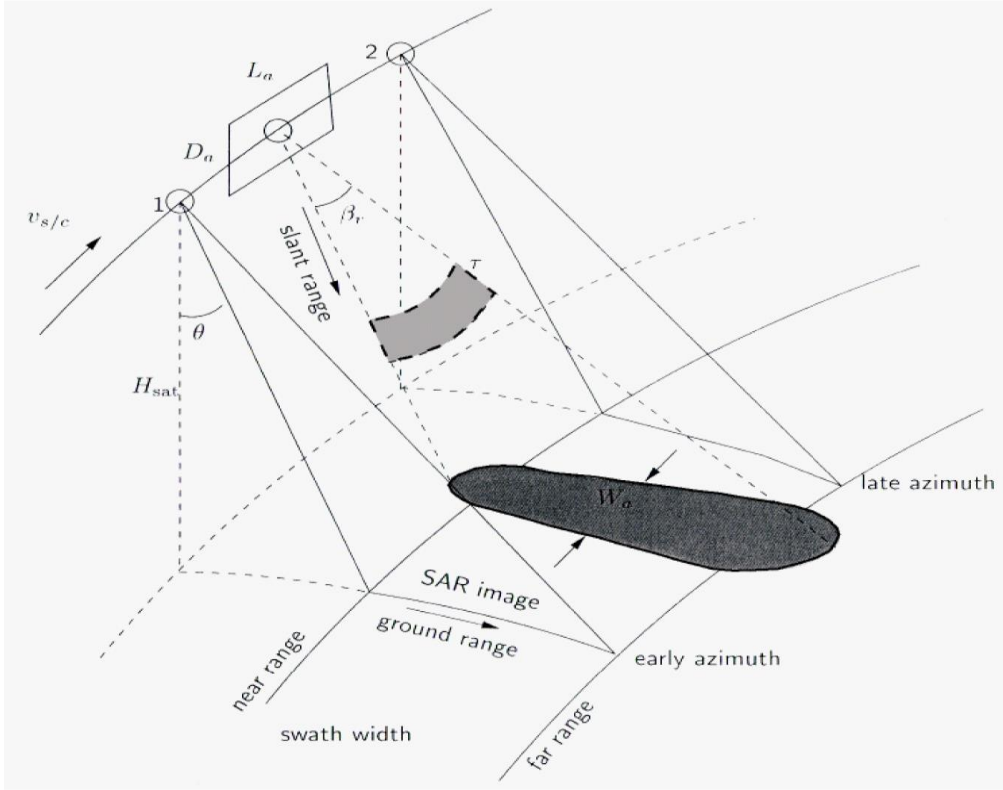
Figure 8. Illustration of SAR imaging geometry.

The distance between the moving radar, constant velocity v, and a point in the ground can be calculated by applying the Pythagorean theorem, at any given time t (which is related to the movement of the platform). Assuming the point is described by the coordinates $(x,y,z) = (x_0,0,\Delta H)$ then:

$$r(t) = \sqrt{r_0^2 + (vt)^2} = r_0 + \frac{(vt)^2}{2r_0} , where \frac{vt}{r_0} \ll 1 \tag{1}$$

For two objects to be properly distinguished, the received pulses must be completely separated. Assuming their distance is δr and the time difference between them is Δt=2δr/c, c is the speed of light, then:

$$\delta r \geq \Delta r_{SR} = \frac{ct}{2} \tag{2}$$

Δr_{SR} is the slant range resolution, which can be expressed via the corresponding pulse bandwidth (Δf=1/τ). Ground range resolution is usually referred as the minimum

distance needed for two objects to be properly recognized, which with the above expression can be translated as slant resolution projection on the ground

$$\Delta r_{GR} \cong \frac{c}{2 \cdot \Delta f \cdot \sin(\theta)} \tag{3}$$

To achieve higher resolutions, modern radar systems transmit long linear frequency modulated pulses (chirp, figure 9).

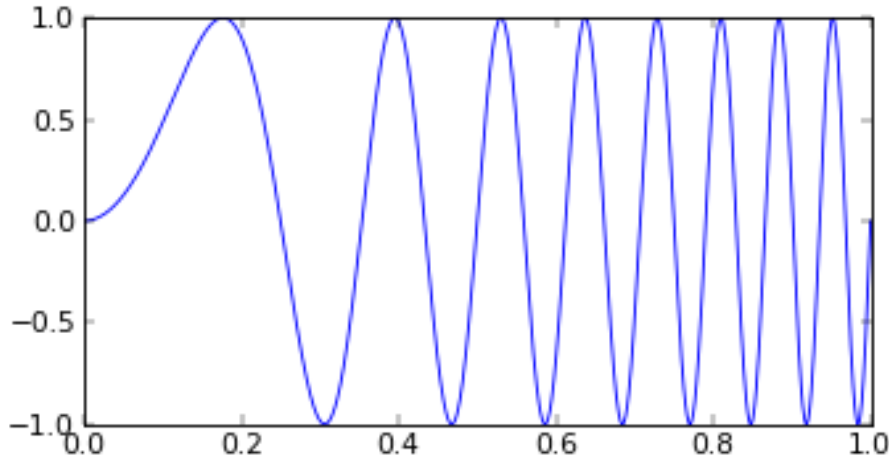$$p(t) = \cos\left(2\pi f_0 t + \frac{a}{2} t^2\right) rect\left(\frac{t}{\tau}\right) \tag{4}$$

Figure 9. Chirp pulse.

Where f_0 is the frequency of the signal, a is the chirp rate and rect(t/τ) is the rectangular pulse. The returning signal is sampled both in fast time (range) and slow time (azimuth). The compression is required because in the raw data the information related to one pixel is spread all over the image. Each range line is multiplied by the conjugate spectrum of the chirp line. The resulted image is range compressed and can give the relative distance between ground and radar antenna. Azimuth compression follows the same reasoning. Assuming elemental scatterer at range r(t), the azimuth signal is given by:

$$s_a(t) = A\sqrt{\sigma_0} \exp(i\varphi^{scatt}) \exp\left(-i\frac{4\pi}{\lambda} r(t)\right) \tag{5}$$

17

A is the dependency of the signal, received on parameters of the system, while the antenna pattern weighs as the azimuth and elevation angles function. The azimuth signal frequency variation is similar to the range domain (azimuth chirp):

$$f_D = -\frac{1}{2\pi}\frac{\partial}{\partial t}\frac{4\pi}{\lambda}r(t) = -\frac{2v^2}{\lambda r_0}t \qquad (6)$$

The azimuth frequency is called Doppler frequency in analogy to the Doppler effect [18]. With the reconstructed chirp signal, the azimuth resolution is improved by being independent of the target to sensor distance and only dependent of the actual antenna dimension along the azimuth direction.

$$\Delta x_{SAR} = \frac{L_{azimuth}}{2} \qquad (7)$$

1.4.3 Image Formation

SAR images are displayed in values of intensity, and as such every image pixel gives an indication of the reflection index of the specific point on the ground. With the reflectivity known, calibration can be used in the image for a radar cross section normalization of the area. Calibration involves internal instrument calibration and external calibration using targets on the ground with well-known reflectivity [19]. With the calibration finished, geocoding is used in the SAR image, to ensure that every pixel representing a target on the ground is directly associated to its actual position on the ground.

It is known that a radar system can project a three-dimensional scene on the radar coordinates (slant range, azimuth range), which is the reason an image directly obtained from the radar cannot be identified clearly, as it is geometrically distorted.
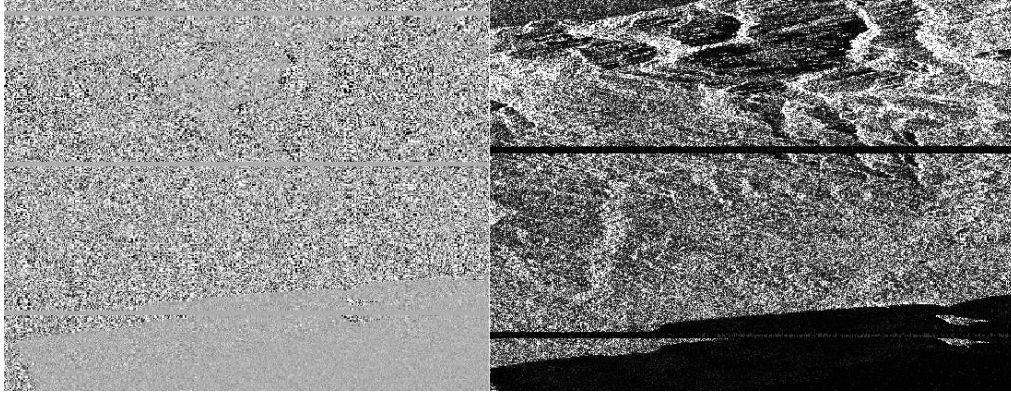
Figure 10. Sentinel-1 SAR images of the Prefecture of Chania. Left) Real part of the scene, Right) Intensity map of the scene (the straight lines in the images are the burst result of the acquisition mode).

The formation of the raw SAR imagery can be described by simple geometrical properties. Assuming a cylindrical system as our reference point with its axis being the flight direction, let us denote the following parameters:

- x, r: azimuth and slant range coordinates
- $\theta(x, r)$: the look angle of SAR
- R: target-antenna distance relevant to the antenna position

The distance R, can be expanded to the position of x' (azimuth coordinate of antenna):

$$R \cong \frac{r}{cos\varphi} - sin\varphi[x' - x + rtan\varphi] + \frac{cos^3\varphi}{2r}[x' - x + rtan\varphi]^2 \tag{8}$$
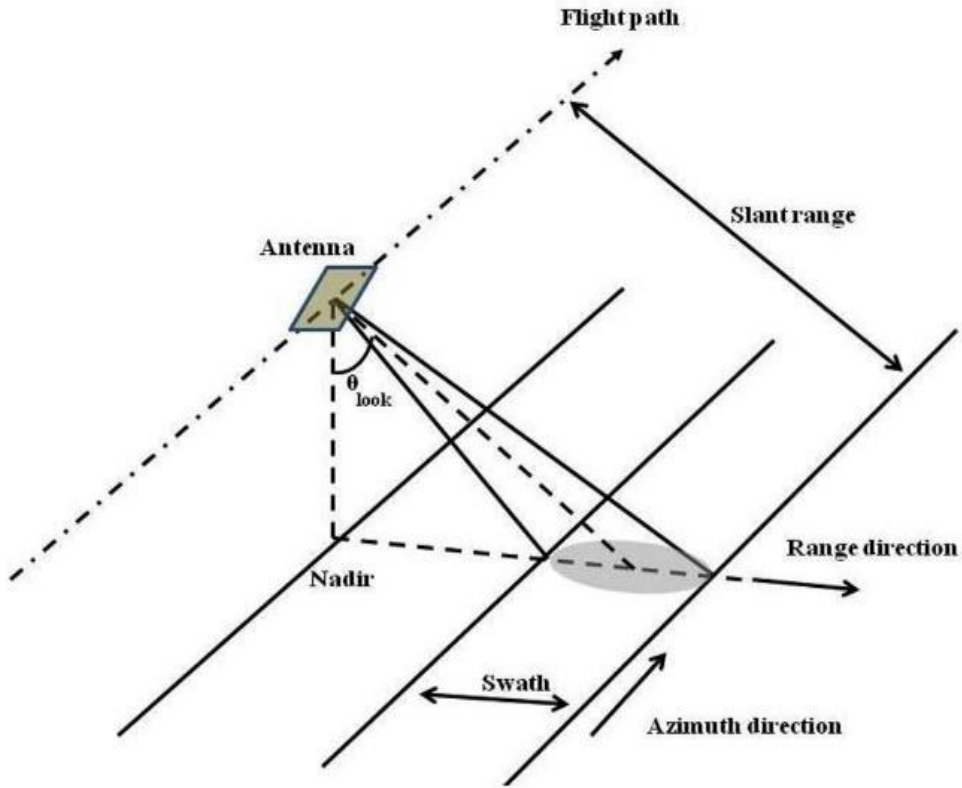
$$R = r + \Delta R$$

Figure 11. Typical side-looking radar geometry (Source: NASA).

The raw SAR signal can be described by the reflectivity pattern RP(x, r) and the elementary return echo from the surface as:

$$recorded\ signal(x,r) = \iint RP(x,r)g(x' - x, r' - r, r)dxdr \qquad (9)$$

g(x′-x, r′-r, r) represents the system impulse response. Calculation of total complex reflectivity for each resolution cell is given by:

$$\Phi = \sum_i \sqrt{\sigma_i} \exp(i\varphi_i^{scatt}) \cdot \exp(-i\frac{4\pi}{\lambda}r_{0,i}) \qquad (10)$$

where i is the number of elemental scatterers. By the equations above, it is shown that the SAR imaging is managed through a filter operation that uses the reflectivity pattern and the recorded signal [20-22].

One of SAR problems is   the signal sampling; the sampling rate of the converter must be larger than the transmitted chirp, which is also the problem in azimuth translation. For the sampling rate, improving the range resolution leads to an increased data rate and volume, thus solving this case. For the azimuth, due to various parameter the problem become more complex. Using a higher Doppler bandwidth of the received echo signal to improve the resolution leads to a higher sampling. This leads to the reduction of the echo length, which means reduced swath width. Thus, azimuth resolution and wide swath cannot be obtained simultaneously by a single-channel SAR. Modern SAR satellites can operate in different imaging modes, which is done by dividing the antenna into sub-apertures where each one employs different phase and amplitude. If a wider swath is required, the system is operated in ScanSAR mode, using different elevations angle for the antenna corresponding to multiple sub-swaths. If a better azimuth resolution is required, the system utilizes Spotlight mode, where the antenna pattern is steered in azimuth towards a fixed point [23].

1.4.4 SAR interferometry

SAR interferometry is a technique that enables accurate measurement of geophysical parameters (such as ground deformation and surface topography) [24-25]. It exploits the phase difference of two or more SAR images, acquired at different times and/or from different orbit positions, calculating the path differences on the ground position, with an accuracy in the range of centimeters or even in the range of millimeters. There is one drawback to this operation, concerning the ambiguity between the measured range difference and the wavelength, which is resolved by using the phase unwrapping operation. The phase unwrapping technique is discussed in a later part of this thesis. The acquisition of SAR images, involving two antennas, can be done in three different ways:

- Same time and from different positions, the antennas are spaced in the across-track range (across-track interferometry)

- Same position and at different times, (along-track interferometry)
- Different times and from different positions (repeat-pass across-track interferometry)

For the purpose of this thesis, repeat-pass across-track interferometry is the focus, by using the Sentinel-1A and -1B satellites. Although the analysis and mathematics used in the operations can be found in several published papers [27-31], the basic parameters are presented. In this acquisition mode, the antennas are separated by the baseline vector **b**, which in turn is decomposed to parallel and perpendicular components $(b_{\parallel}, b_{\perp})$. From the geometry observed in Fig. 13, the components can be calculated as:

$$b_{\perp} = b\cos(\theta - \alpha) \tag{11}$$

$$b_{\parallel} = -b\sin(\theta - \alpha) \tag{12}$$

where θ and α, are the side-looking angle and elevation angle respectively. The height difference Δh between the two antennas can be directly linked to the range difference Δr and the perpendicular baseline by the following equation:

$$\Delta r \cong \frac{B_{\perp}}{r_0 \sin \theta_i} \cdot \Delta h_i \tag{13}$$

With the range difference being related to the phase difference:

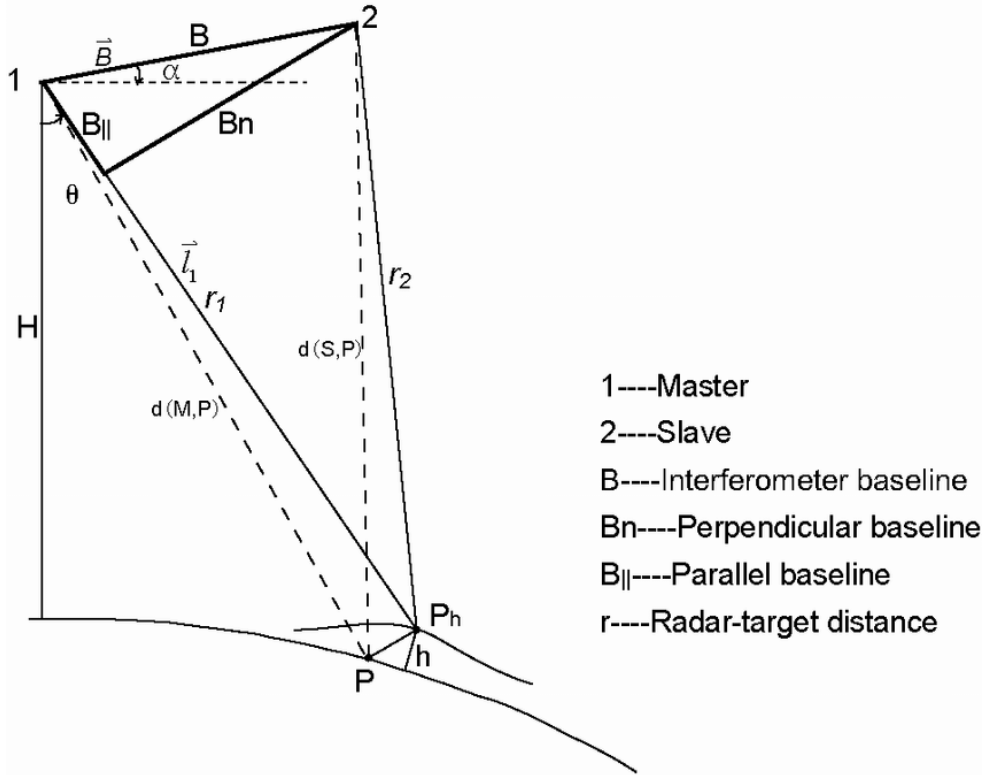$$\Delta \varphi = m \frac{2\pi}{\lambda} \Delta r \tag{14}$$

Figure 12. Repeat-pass Across track interferometry geometry [26].

where λ is the wavelength and m is the factor of the receiving paths. It is equal to one, for a single-pass SAR interferometry, one antenna transmits and two antennas receive the echoes, and is equal to two for the repeat-pass interferometry. The receiving focused echoes of the images $(\hat{\gamma})$, are related to the reflectivity functions $(r(\cdot))$ of the illuminated area at different times. Assuming a zero-valued spatial resolution and pixel SAR coordinates (x', r'), the SAR images can be expressed as:

$$\hat{\gamma}_1(x',r') = r_1(x',r') \exp\left(-j\frac{4\pi}{\lambda}r'\right)$$

$$\hat{\gamma}_2(x',r') = r_2(x',r'-\Delta r) \exp\left(-j\frac{4\pi}{\lambda}r'\right) \tag{15}$$

The difference (Δr) in the path of the second image, known as *slave* image, in respect to the first one known as *master* image, exists due to the across-track function of the acquisitions. For this reason, when dealing with SAR interferometry, it is proper to co-register the

23

images with the purpose of working in the same reference geometry, thus the terms master and slave image:

$$\hat{\gamma}_2(x', r' + \delta r') = r_2(x', r')\exp[-j\frac{4\pi}{\lambda}(r' + \delta r')] \tag{16}$$

With the two images in the same geometry reference, the complex interferogram can be generated:

$$\hat{\gamma}_1(x', r')\widehat{\gamma_2^*}(x', r') = |\hat{\gamma}_1(x', r')||\hat{\gamma}_2(x', r')|\exp[j\frac{4\pi}{\lambda}\delta r' + j\angle r_1(x', r') - \angle r_2(x', r') \tag{17}$$

The (*) operator is referring to the conjugate operation, while the ∠(·) operator is referring to the full phase operation (not restricted) to the [-π, π] interval. The full phase term, assuming the same geometry between the two images and a non-changed topography scattering geometry, can be derived by

$$\Delta\Phi = \frac{4\pi}{\lambda}\delta r' \tag{18}$$

To calculate the δr', the parallel ray approximation, proposed by Zebker and Goldstein [13] is applied.

$$r' + \delta r' = \sqrt{b^2 + r'^2 - 2br'\sin(\theta' - \alpha)} = r' - b\sin(\theta' - \alpha) \tag{19}$$

and thus, the interferometric phase is

$$\Delta\Phi = \frac{4\pi}{\lambda}\delta r' = b\sin(\theta' - \alpha) = \frac{4\pi}{\lambda}b_\parallel \tag{20}$$

With the full phase term known, we can now estimate the accuracy of the topographic measurements. Assuming that ground reference is z=0, we expand the full phase term around θ'_0 (look angle of the reference surface)

$$\Delta\Phi \approx \frac{4\pi}{\lambda}b[\sin(\theta'_0 - \alpha) + \cos(\theta'_0 - \alpha)(\theta' - \theta'_0) \tag{21}$$

The height of the target point is obtained via the look angle and sensor height by

$$\frac{\partial z}{\partial \theta'} = r'\sin\theta' \rightarrow \theta' - \theta'_0 \approx \frac{z}{r'\sin\theta'_0} \tag{22}$$

The full phase term can be rewritten as

$$\Delta\Phi \approx -\frac{4\pi}{\lambda}b\sin(\theta'_0 - \alpha) - \frac{4\pi}{\lambda}b\cos(\theta'_0 - \alpha)\frac{z}{r'\sin\theta'_0} \tag{23}$$

The first term of eq. (23), is the *flat-Earth* contribution while the second term accounts to the topography profile.
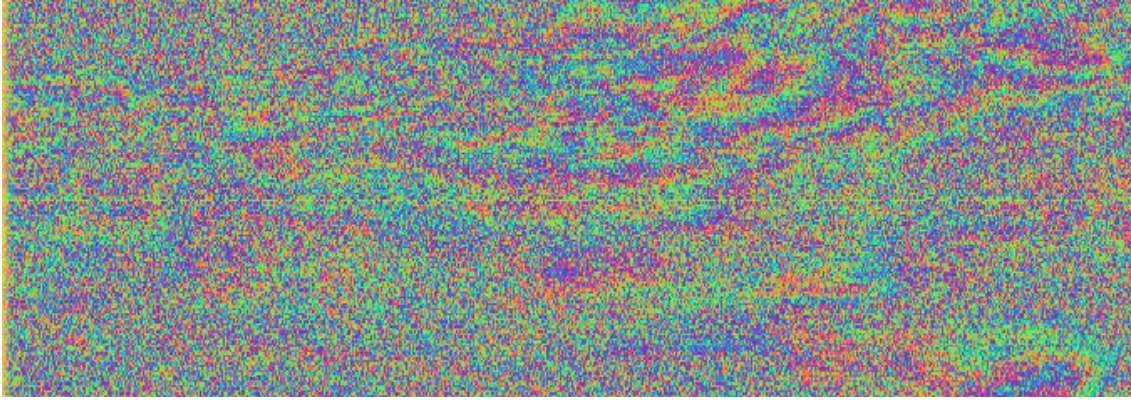

Figure 13. Interferogram of Western Crete obtained by the data obtained from Sentinel-1 satellite on 10 June 2017 and 10 July 2017. The fringe pattern is the result of the flat-Earth term calculation that takes into account only the [-π, π] interval, thus the fringes are attributed to the 2π-phase jumps.

Taking into account the Earth curvature, the phase difference in respect to the range can be written as:

$$\frac{\partial\Phi}{\partial r'} = -\frac{4\pi}{\lambda}b\cos(\theta' - \alpha)\frac{\partial\theta'}{\partial r'} \tag{24}$$

Considering a triangle between the radius of Earth, R_E, the height of the satellite, H, and r', then the following equations can be derived:

$$R_E^2 = (R_E + H)^2 + r'^2 - 2r'(R_E + H)\cos\theta'$$

$$\cos\theta'_0 = \eta = \frac{(R_E+H)^2 + r'^2 - 2r'(R_E+H)}{2r'(R_E+H)} \tag{25}$$

From equations (24), (25) the phase difference can be rewritten as:

$$\frac{\partial(\Delta\Phi)}{\partial r'} = -\frac{4\pi}{\lambda}\frac{b\cos(\theta'_0 - a)}{r'\sin\theta'_0}\left(\cos\theta'_0 - \frac{r'}{R_E + H}\right) \tag{26}$$

If we apply the approximation $\frac{r'}{R_E+H} \ll 1$, then the flat-Earth component has a different expression with respect to equation (23):

$$\Delta\Phi_{flat}(x',r') = -\frac{4\pi b_\perp}{\lambda r' \tan\theta'_0}(r' - r'_0) \tag{27}$$

With the general topography of the Earth known, we now consider the local topography of the illuminated region. Assuming a local topography slope, L, and the flat-Earth case, the fringe frequency of the localized topography can be obtained by:

$$\frac{\partial(\Delta\Phi)}{\partial r'} = -\frac{4\pi}{\lambda}\frac{b_\perp}{r' \sin\theta'}\left[\cos\theta' + \frac{\sin L}{\sin(\theta'-L)}\right] \tag{28}$$

The latter part of the equation, can be rewritten as

$$\cos\theta' + \frac{\sin L}{\sin(\theta'-L)} = \sin\theta'\frac{\cos(\theta'-L)}{\sin(\theta'-L)}$$

and so

$$\frac{\partial(\Delta\Phi)}{\partial r'} = -\frac{4\pi}{\lambda}\frac{b_\perp}{\tan(\theta'-L)} \tag{29}$$

Finally, the local fringe range frequency is obtained by

$$f_{\Delta\Phi} = \frac{1}{2\pi}\frac{\partial(\Delta\Phi)}{\partial r'} = -\frac{2b_\perp}{\lambda r' \tan(\theta'-\overline{L})} \tag{30}$$

One last factor that may result in ambiguities in the calculation of the phase term is the height accuracy. Height resolution, σ_{HR}, is directly related to the phase term:

$$\sigma_{HR} = -\frac{\lambda r' \sin\theta'_0}{4\pi b_\perp}\sigma_{\Delta\Phi} \tag{31}$$

Some solutions to these problems are presented [32-33]. One possible solution for this problem would be to use data-pairs with a large perpendicular baseline difference value. Though, a large difference between the baselines increases the possibility of ambient noise in the interferogram, thus leading to magnified phase calculations and lowering the quality of the final results. A second possible solution for accuracy estimation, is to neglect the flat-Earth term and so the topography is expressed by:

$$z = \left(\frac{r \sin \theta\prime}{b_\perp}\right) b_\parallel \tag{32}$$

Another solution is using equation (31), with the value of $\sigma_{HR}=2\pi$

$$z_{2\pi} = - \left|\frac{\lambda r\prime \sin \theta\prime_0}{4\pi b_\perp}\right| \tag{33}$$

1.4.5 Coherence Calculation

Coherence is referred to the relationship, between two or more, waves in the electromagnetic radiation. We call two waves coherent, when they vibrate in unison, meaning that they are in phase. In terms of radar, it describes systems that preserve the phase of the received signals. In Interferometry, coherence is used to measure the correlation of an interferogram. It ranges between 0, (meaning there is no useful information in the interferogram), to 1 (which is a perfect interferogram). Coherence can be affected by a number of parameters:

- Long lags between the pairs of the interferogram lead to low coherence
- Large baselines lead to low coherence
- Steep slopes in the topography lead to low coherence
- High vegetation values in the surface affect the coherence
- Mistakes in the co-registration process or in the resampling procedure lowers the coherence

Figure 14. Coherence map of part of Western Crete (interferogram for October 2017 and December 2017).

To calculate the coherence, we first assume two SAR images

$$\hat{\gamma_1}(x', r') = \iint \gamma_1(x, r) \exp\left(-j\frac{4\pi}{\lambda} r\right) sinc\left[\frac{\pi}{\Delta r}(r' - r)\right] sinc\left[\frac{\pi}{\Delta x}(x' - x)\right] \exp[j\xi_{d1}(x' - x)] \, dx dr$$

$$\hat{\gamma_2}(x' + u'_x, r' + u'_r) = \iint \gamma_2(x, r) \exp\left(-j\frac{4\pi}{\lambda}(r + \delta r)\right) sinc\left[\frac{\pi}{\Delta r}(r' - r + u'_r - \delta r)\right] sinc\left[\frac{\pi}{\Delta x}(x' - x + u'_x - \delta x')\right] \exp[j\xi_{d2}(x' - x)] \, dx dr \tag{34}$$

To simplify the above equations, the following variable changes are introduced,

$$k = x' - x$$
$$p = r' - r$$

Hence,

$$\hat{\gamma_1}(x', r') = \exp\left(-j\frac{4\pi}{\lambda} r'\right) \iint \gamma_1(x' - k, r' - p) \exp\left(-j\frac{4\pi}{\lambda} p\right) sinc\left[\frac{\pi}{\Delta r} p\right] sinc\left[\frac{\pi}{\Delta x} k\right] \exp[j\xi_{d1} k] \, dk dp$$

$$\hat{\gamma_2}(x', r') = \exp\left(-j\frac{4\pi}{\lambda}(r' + \delta r)\right) \iint \gamma_2(x' - k, r' - p) \exp\left(-j\frac{4\pi}{\lambda}(p - \delta r + \delta r')\right) sinc\left[\frac{\pi}{\Delta r}(p + u'_r - \delta r)\right] sinc\left[\frac{\pi}{\Delta x}(k + u'_x - \delta x')\right] \exp[j\xi_{d2} k] \, dk dp \tag{35}$$

The complex interferogram value is obtained by:

$$E[\gamma(x_1, y_1)\dot{\gamma}(x_2, y_2)] = |\gamma|^2 \delta(x_1 - x_2)\delta(y_1 - y_2) \tag{36}$$

Using the two SAR images we can calculate the cross-correlation factor

$$\chi = \frac{E[\gamma_1 \gamma_2]}{\sqrt{E[|\gamma_1|^2]E[|\gamma_2|^2]}} \tag{37}$$

Using equations (35), (36)

$$E[\gamma_1 \dot{\gamma}_2] = \exp\left(j\frac{4\pi}{\lambda}\delta r'\right) \iint dk dp \exp\left(j\frac{4\pi}{\lambda}(\delta r - \delta r') + (\xi_{d1} - \xi_{d2})\right) k sinc\left[\frac{\pi}{\Delta\chi}k\right] sinc\left[\frac{\pi}{\Delta\chi}(k + u'_x - \delta x')\right] sinc\left[\frac{\pi}{\Delta r}p\right] sinc\left[\frac{\pi}{\Delta r}(p + u'_r - \delta r)\right] \tag{38}$$

As stated in the start of this section, local slope directly affects the coherence estimation of the interferogram. The slant range difference in respect to the local slope is:

$$\delta r' - \delta r \approx -\frac{b_\perp}{r'}(r' - r)\frac{1}{\tan(\theta' - \bar{L})} = -p\frac{b_\perp}{r'\tan(\theta' - \bar{L})} \tag{39}$$

Now, the complex interferogram value can be rewritten as

$$E[\gamma_1 \dot{\gamma}_2] = \exp\left(j\frac{4\pi}{\lambda}\delta r'\right)\int dp \exp\left(-j\frac{4\pi}{\lambda}\frac{b_\perp}{r'\tan(\theta' - \bar{L})}p\right) sinc^2(v)\int dk \exp(j\Delta\xi_d k)sinc^2\left(\frac{\pi}{\Delta x}k\right) \tag{40}$$

With the implementation of the local slope factor in the estimation of the complex value, any mis-registration effect to the interferogram is neglected.

In the start of this section it was referred that coherence is measured between the interval [0,1]; where 0 shows that two images are not at the same phase while 1, shows that the two images are in the same phase. The factors for the coherence decrease can be described using the cross-correlation factors relevant to each noise source [34]. The cross-correlation factor is obtained by:

$$\chi = \frac{E[I_1 I_2^*]}{\sqrt{\sqrt{E[|I|^2]E[|I_2|^2]}}} = |\chi|\exp(\Phi_{int}) \tag{41}$$

With the cross-correlation factor known, the decorrelation equation is provided by:

$$\chi = \chi_{thermal} \cdot \chi_{temporal} \cdot \chi_{spatial} \cdot \chi_{doppler} \cdot \chi_{misreg} \cdot \chi_{volum} \cdot exp\left[j\frac{4\pi}{\lambda}\delta r'\right] \tag{42}$$

By implementing the local slope factor, the misregistration effect can be neglected from equation (42). Temporal decorrelation is associated with the change of the responding echo originating from the ground, due to weather conditions of the area or from human activities (especially in rural areas) and is dependent to the starting wavelength (radar). The statistical modelling of this factor is considered difficult, for the reason, that when considering an area of interest, one has to know all the local weather and climate changes, as well as all the various factors that can affect the signal.

Assuming that the thermal factor and the temporal factor as minor, equation (43) can be written as:

$$\chi = exp\left[j\frac{4\pi}{\lambda}\delta r'\right] \cdot \left(\Delta r \cdot \Lambda\left[\frac{2\Delta r}{\lambda}\frac{b_\perp}{r\tan(\theta'-\bar{L})}\right]\right) \cdot \left(\Delta x \cdot \Lambda\left[\frac{\xi_{d1}-\xi_{d2}}{4\pi}L_a\right]\right) \tag{43}$$

The first part of the function $\Delta r \cdot \Lambda$, is associated with the spatial decorrelation. The change in the incidence angle between N SAR images, leads to a shift in the range spectra which is associated to the local fringe frequency in the range domain. If the perpendicular baseline increase, then the corresponding spectral shift, may lead to non-overlapping images, which is a complete decorrelation case (coherence is equal to 0). For this reason, when using InSAR analysis, perpendicular baselines of 600m and above, are not used. The $\Delta x \cdot \Lambda$ term, refers to the Doppler decorrelation factor. It is associated with the difference of the two (or more), doppler centroids and can result to azimuth spectral shifts between the SAR images. We consider no spectral overlap when $|\xi_{d1} - \xi_{d2}| > \frac{4\pi}{L_a}$.

Finally, the last decorrelation factor is associated with the Fourier transform domain (it appears when calculating the shift from radar coordinates to geocoded coordinates).

Chapter 2

Differential Interferometry Technique (DInSAR)

Differential Interferometry is a well-established interferometric technique. In the beginning, it was used to investigate the deformation of distinctive geological and geophysical events [35-37]. In recent times, these techniques are used in larger areas and timelines, to investigate the temporal evolution of deformation by using multiple differential interferograms in the generation of deformation time-series [38-42]. These methodologies require the measurement of Line of Sight (LOS) propagation through high sensitivity SAR instruments and the implementation of those, in processing chains that require complex mathematical analysis and capable computational equipment. In the context of this thesis, of particular interest is the Small Baseline Subset (SBAS) approach [39, 42].

The processing chain that was used in this thesis is presented below and in the rest of this chapter, the analytics and mathematics used are presented. The data selection of the processing chain regards a set of N+1 complex-valued SAR images that are all in relation to the same region of interest (ROI). The steps of the processing chain are separately shown in Figure 15 and presented below:

- In each SAR acquisition, the orbital parameters are evaluated and used in the estimation of spatial resolution, the orbit file implementation is described in this step;
- Data-pairs were selected with pre-decided characteristics (i.e. time differences);
- Co-registration of each SAR image in respect to identified master images (perpendicular baselines are estimated as well);
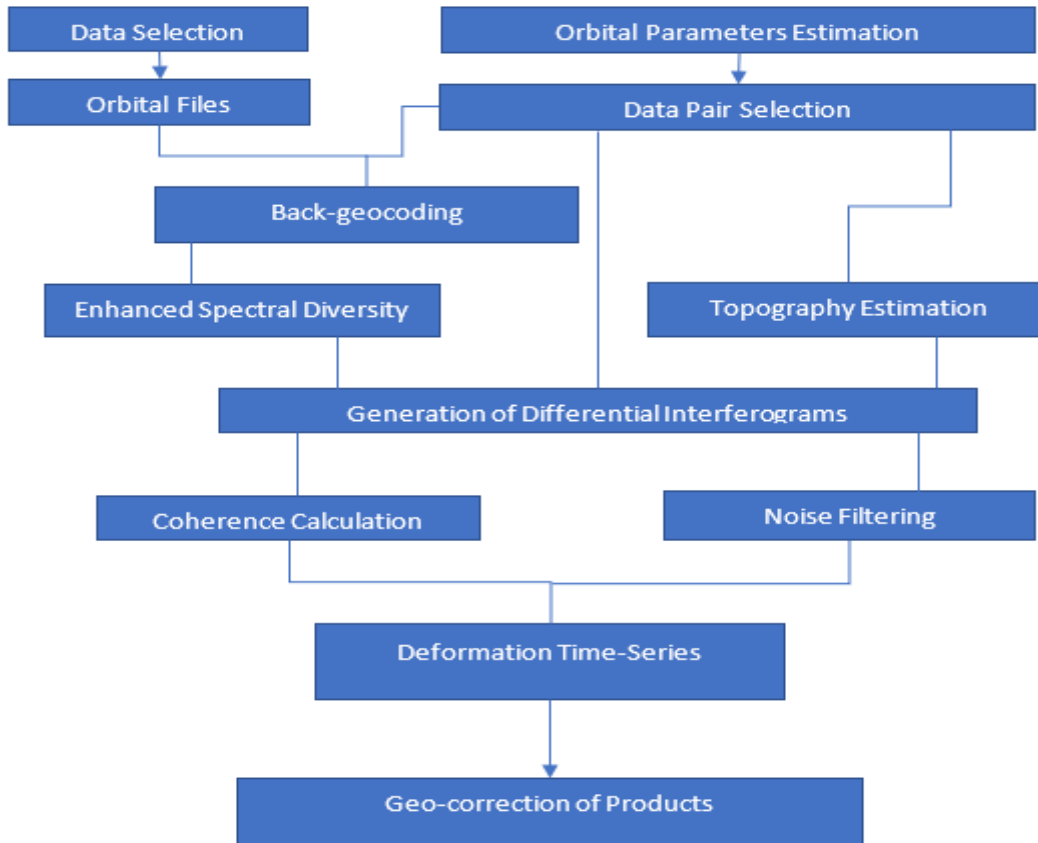
Figure 15. Processing chain of the deformation time-series generation

- Calculation of the synthetic fringes created due to the phase difference in the topography of the data-pair;

- Generation of the Differential Interferograms; in this step the synthetic fringes are subtracted from the phase difference of each interferometric pair;

- Noise Filtering using the Goldstein phase filtering operation, on each DInSAR pair;

- Coherence calculation of each DInSAR pair, from the result non-optimal (coherence value close to 0) data-pairs can be excluded from the rest of the process;

- Generation of the Deformation Time-Series, which is done by the reconstruction of the deformation evolution of the illuminated area. Calculation of the residual topographic components and atmospheric effects are also included in this step;

- Last step is the geolocalization and the projection to a cartographic grid (in our case WGS84) of the image points obtained in the deformation time-series.

2.1 Precise orbit Calibration

Knowing the flight path of the satellite is paramount in the calibration of the data included in the DInSAR processing chain. Usually, the generic orbit, represented by vectors, is supplied along the raw data file into data-bases that can be easily accessible; one of the suppliers with a rich database of orbit files is the University of Delft. Those vectors however, contain errors that are attributed to miscalculations of the true position of the radar in space, thus leading to inaccurate calculations of the topographic fringes and the flat-Earth phase terms on the interferograms. For this purpose, the characteristics of the satellite in orbit are made known from the organizations that handle them. Altitude height, angle of incidence and orbit cycle (can be seen in Chapter 1.2) are some of the characteristics that can help in the calibration of the default orbit files and subsequently in the calculation of flat-Earth phase and the topography.

Due to the high Doppler centroid variation and the non-continuous acquisition of the TOPSAR mode (burst acquisition), the data from Sentinel-1 are more prone to errors on their orbital parameters. In the burst acquisition mode of TOPSAR, there are two prominent components that can lead to phase distortion: firstly, the Doppler centroid can change very fast during the burst mode, which can lead to mis-registration becoming a phase constant that distorts the overall phase characteristics, and secondly

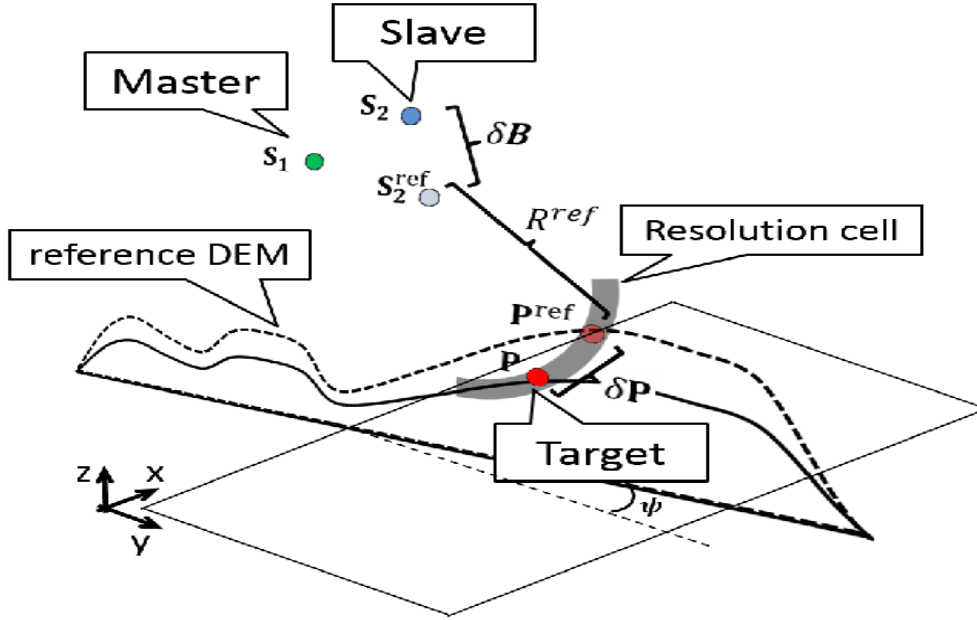the Doppler centroid can be discontinuous in bursts transitions leading to phase jumps [43].

Figure 16. Representation of the geometry used in the precise orbit calibration procedure [44].

Assuming the geometry of sensor positions S1 (master image), S2 (slave image) and the target P (figure 16), the geometric contribution can be determined as:

$$\Delta\varphi = \frac{4\pi}{\lambda}(\Delta R) = \frac{4\pi}{\lambda}(|S_2 - P| - |S_1 - P|) \tag{44}$$

With the true position of the three sensors known, (referenced positions), the geometric error between master and slave position is calculated by:

$$\Delta R = \Delta R_2 - \Delta R_1 = |S_2 - P| - |S_{2,ref} - P_{ref}| - |S_1 - P| + |S_{1,ref} - P_{ref}| \tag{45}$$

Assuming that the master image point is known and $\Delta R_1 = 0$ then eq. 45 is rewritten as

$$\Delta R = |S_2 - P| - |S_{2,ref} - P_{ref}| \tag{46}$$

The geometric errors of those three vector positions can be assumed that are the sum of two vectors. The distance between known and actual position of the slave image δS(δSx,

δSy, δSz) and the difference between reference DEM and the actual DEM δP(δPx, δPy, δPz). The phase error can be derived using those two vectors and the known geometry from the orbital characteristics (squint and look angles):

$$\Delta R(\psi, \theta_{S1}, \theta_{S2}) = \sin\psi \cdot \delta S_x(\tau_\psi) - \cos\psi \cdot \sin\theta_{S2} \cdot \delta S_y(\tau_\psi) + \cos\psi \cdot \sin\theta_{S2} \cdot \delta S_y(\tau_\psi) +$$
$$\cos\psi \cdot (\sin\theta_{S2} \cdot \cot\theta_{S1} - \cos\theta_{S2})\delta z \tag{47}$$

where ψ is the squint angle and δz is the DEM error component.

Due to the different components present in the phase, it is difficult to separate and properly calculate the contributions. One method used was proposed by A. M. Guarnieri *et al.* [44]; it exploits the Multi-Squint (MS) phase which is dependent on the orbit errors. Assuming linear orbit errors then:

$$\delta S(\tau) = \delta \hat{S}(\tau) + \tau \cdot \Delta(\delta S) \tag{48}$$

Equation (47) can now be written in respect to the squint angle:

$$\frac{\partial \Delta R}{\partial \psi} = \cos\psi \cdot \delta S_x + \sin\psi \cdot R_0 \cdot \Delta(\delta S_x) + \sin\psi \cdot \sin\theta_S \cdot \delta S_y - \sin\psi \cdot \cos\theta_S \cdot \delta S_z -$$
$$\cos\psi \cdot \sin\theta_S \cdot R_0 \cdot \Delta(\delta S) + \cos\psi \cdot \sin\theta_S \cdot R_0 \cdot \Delta(\delta S_z) + \sin\psi \cdot (\sin\theta_{S2} \cdot \cot\theta_{S1} - \cos\theta_{S2})\delta z$$
$$\tag{49}$$

The achieved equation is now only related to the squint angle and the geometric parameters between the SAR system and the illuminated target, while the InSAR derivative is related to the difference between two azimuth apertures in respect to the squint angle.

2.2 Data-pair selection

The results of the deformation estimation and time-series are all dependent on the perpendicular baseline vector values; in that respect each image can be represented in a Time/Perpendicular Baseline plane. Each image can be characterized by the azimuth spectra frequency and the squint angle; assuming u, as the velocity of the SAR system, λ, the operational wavelength and ψ the squint angle, then each image can be represented by:

$$f_{azim} = \frac{2u}{\lambda} \sin \psi \tag{50}$$

The selection of optimal data-pairs has the constraint that the decorrelation effect present after the process must be limited, or else the achievable results will not be useful (extreme decorrelation mean that the images are out of phase). This can be achieved by selecting the baseline difference between acquisitions to not be very large (not larger than 1200m) and the doppler centroid value difference must be small enough. In respect to the baseline, Sentinel-1 twin satellites already have small baseline differences between acquisitions, due to their orbital programming. As for the Doppler centroid, though there can be some difficulties as can be seen in sub-chapter 2.1, there are calibration methodologies that can compensate for them.

The criteria used for the formation of "master-slave" data-pairs, was the temporal difference between images and geological and/or atmospheric events that took place in the region of interest. It must be noted however that the largest the temporal difference between images, the more significant the effect of the decorrelation phenomena would be in the results.

As noted in the start of the thesis, the two prominent strategies in the DInSAR methodology are the Permanent Scatterers (PS) and the Small Baseline (SBAS). Though there are a lot of other methods used and proposed, they can be considered as hybrid

methodologies between those two. The key difference that separates these two strategies is the formation of the interferometric pairs. Assuming a set of N+1 data acquisitions, in the PS technique, the formation of the interferograms requires each image to be co-registered with the same reference master image.
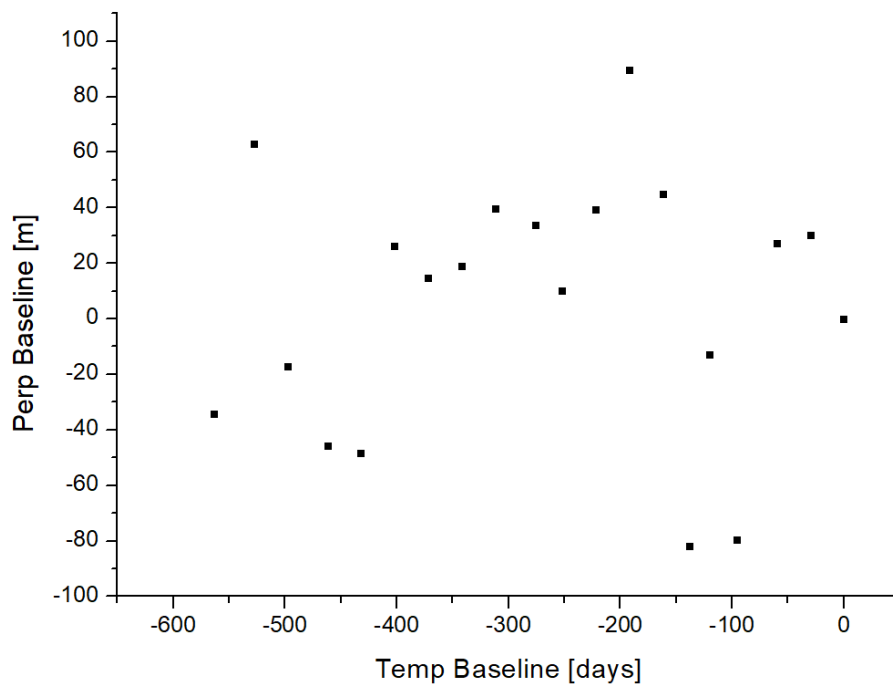

Figure 17. Scatter-plot of the selected data for the purpose of the thesis. As can be seen, the perpendicular baselines are small.

This technique is based in the proper selection of key point scatterers, that even with large perpendicular baseline differences and large temporal differences, useful information can be retrieved. However, using this technique, usage of the coherence criterion of good phase quality between images, cannot be used due to those large differences, as there would be data-pairs with high decorrelation phenomena. The key-reference point selection is done before beginning the interferometry chain, using radiometric calibration, so that the resolution of the images is preserved. The deformation linear velocity is then computed, by using the data inversion approach, pixel by pixel. The atmospheric

correction and the phase residual effects are then computed using spatial-temporal filtering [38].

The SBAS technique, used in this thesis, allows formation of data pairs, with different reference master images, that are linked to each other. The optimal data-pair selection can be obtained by imposing constraints in the perpendicular and temporal domain and the phase noise present in the interferograms [39].

2.3 Sentinel-1 Co-registration procedure

With the data-pairs selected, next step is the registration of said pair. In general for a single pair, assuming coordinates (x'_m, r'_m) for the master image and (x'_s, r'_s) for the slave image, the achieved SAR coordinates when applying the co-registration operation, in respect to a reference point with (x', r') coordinates, will be

$$x'_s = x'_m + \delta x'(x', r')$$
$$r'_s = r'_m + \delta r'(x', r') \tag{51}$$

Basically, the registration process is defined as the problem of calculating the transformation in the geometry between the two images, in respect to the master image, in a way that each ground point is in the same position in the two images.

For the Sentinel-1 (S1) images however, the interferometric processing requires special consideration due to the TOPS ScanSAR burst acquisition and the steering of the antenna beam in the azimuth domain. Due to the high Doppler rate in azimuth, the use of Enhanced Spectral Diversity is considered necessary to obtain the required azimuth accuracy in the co-registration process [41]. Before explaining the co-registration procedure for Sentinel-1, it is imperative to discuss the parameters that are created by the TOPSAR and are needed to be known for the co-registration to have minimal decorrelation effects due to them.

The Doppler rate which is introduced due to the antenna steering is obtained by

$$k_{Dop} = \frac{2v}{\lambda} \omega_r \tag{52}$$

v is the satellite velocity, ω_r the steering rate and λ the radar wavelength.

As can be seen in Fig.8, the image obtained through the TOPS mode, does not have spectral overlap between the bursts, which can lead to decorrelation effects. For this purpose, it is required to burst-synchronize the images in respect to the data acquisition timing. The Doppler shift, that exists between two bursts is given by:

$$\Delta f_{D,shift} = k_t(r) \cdot \Delta t_{acq} \tag{53}$$

where k_t is the Doppler rate at image level

$$k_t(r) = \frac{k_a(r) \cdot k_{Dop}}{k_a(r) - k_{Dop}} \tag{54}$$

k_a is the range-dependent Doppler rate. The variation of squint angle over azimuth and (in lesser extent) range can cause phase ramps in both of those domains [45]. A mis-registration of Δt seconds in the azimuth domain, leads to an azimuth phase ramp of

$$\Delta\varphi_{max} = 2\pi \frac{2v}{\lambda} \Delta\beta\Delta t \ (rad) \tag{55}$$

where $\Delta\beta$ is the change in squint angle.

There are four processes present in the interferometric flow for S1 images.

- Deramping function
- Burst-Level Processing
- Co-registration
- Spectral Shift Filtering

The Deramping function is critical in correcting the Doppler centroid in interpolation and filtering operation on the bursts. The main approaches for this function are

1. Demodulate data; where the complex data are deramped in the azimuth domain for a low-pass signal. It is required for the spectral shift filtering process.

2. Kernel Modulation; kernel is modulated in the azimuth domain in a way that its spectrum follows the local Doppler centroid.

In the Burst-level processing, the ESD technique is applied to obtain the rigid azimuth shift. An external DEM is used along with the orbital information. In this operation, kernel modulation and spectral shift filtering is required for the linear phase to be centered at the Doppler centroid frequency and the increase in coherence. Once the rigid phase is retrieved, the fine azimuth shift is applied to the slave burst by multiplying its Doppler spectra by a linear phase term.

Co-registration is performed by using an external DEM and the orbit information. The orbit information is available from ESA independently in three different products. The orbit annotation inside the SLC product, the reconstituted orbit and the precise orbit. Following the co-registration is the refinement of the shift. In the range domain, cross-correlation is applied to the patches in both master and slave images, followed by shift linear correction. In the azimuth domain, after retrieving the linear correction and along with the rigid shift obtained by ESD, use them to average the residual azimuth for correction.

Spectral Shift Filtering is associated with the correction of the spectral decorrelation that is introduced due to the difference in acquisition geometry between master and slave image. For this purpose, conventional spectral filtering is applied pixel by pixel by calculating the common Doppler bandwidth to compensate for the differences in the Doppler centroid and the burst synchronization issues [41]:

$$B_c = B_a - \left| f_{DC,p}^{mst} - \left(f_{DC,p}^{sl} + \Delta f_{orbit} \right) \right| \tag{56}$$

where B_a is the azimuth bandwidth, $f_{DC,p}^{mst}$ is the Doppler centroid of the master burst on each pixel, $f_{DC,p}^{sl}$ is the Doppler centroid of the slave burst remapped in respect to the master burst geometry and Δf_{orbit} is the spectral shift caused by the nonparallel orbits.

Sentinel-1 SLC images are divided into three sub-swaths (IW1, IW2, IW3), each containing 7 bursts of acquisitions. In the case of one sub-swath, the above operations are simple. In the case of a region of interest present in multiple sub-swaths, the above operations must be performed into each sub-swath separately. As such, the Doppler centroid rate, must always be adjusted to each range bin.

2.4 Topography Estimation

In this section, extraction of the topographic phase components is performed. For the images used in this thesis, the topographic estimation was performed by exploiting an external digital elevation model (DEM) to reconstruct the fringes present in the topography, and the extraction of the phase components, which was carried out by using the Shuttle Topography Mapping (SRTM).

The phase of the scene topography can be estimated, pixel by pixel of the co-registered SAR images, by the slant-range difference between master and slave image:

$$\Delta\varphi_{m,s} \cong \Delta\Phi_{flat} - \frac{4\pi}{\lambda} \frac{b_\perp}{\bar{r}\sin\theta'} z \tag{57}$$

$b_\perp$ is the perpendicular baseline of the data-pair, θ' the look angle and r is the slant range difference.

Topography estimation begins with the evaluation, pixel by pixel, of the DEM image onto the geometry of the master image. To accomplish that, the DEM points are transformed to a corresponding point in the cartesian system, $P(x_D, y_D, z_D)$, which is associated to a point of the master image geometry, $Q(x, y, z)$.

$$\begin{cases} \left|\vec{P} - \vec{s}_M(t_i)\right| = r_M \\ \vec{s}_M(t_i) \cdot \left[\vec{P} - \vec{s}_M(t_i)\right] = 0 \end{cases} \tag{58}$$
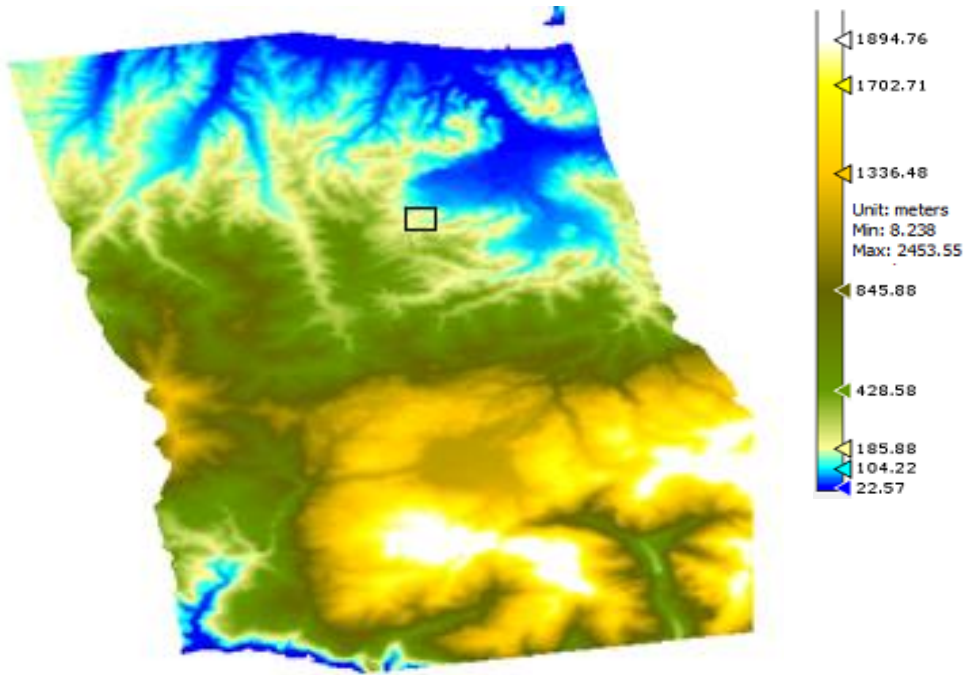
Figure 18. Digital Elevation Map of Western Crete; Blue color represents the lowest elevation (sea level) and White, represents the highest (peak of White Mountains). The black rectangle shows the Valsamiotis dam area.

P is the position of the target, t_i is the time where the target is illuminated by the SAR system, and $\vec{s}_M(t_i)$ is the position of the SAR system. To estimate the SAR position at the time of the acquisition, it must be transformed in the same cartesian system of reference as the master image, $\vec{s}_M(x, y, z)$, in respect to the starting moment t_0. The (t, r) unknowns can be estimated by

$$t_i = t_0 + \frac{i}{f_{PR}}$$
$$r_M = r_0 + \frac{c}{2f_{smp}}j \tag{59}$$

r_0 is the near range distance, c the speed of light, f_{PR} is the pulse repetition frequency and f_{smp} is the range sample frequency. The (i, j) reference system is used as an intermediate system, with which the DEM points can be converted to the selected reference geometry grid.

With all the points of DEM referenced to the selected geometry, next step is the measurement of the SAR acquisitions in the SAR coordinates. Assuming the n-th acquisition which was taken at time t_i, the position vector is estimated by:

$$\vec{s}_n = \begin{cases} x_n = \tilde{a}_0 + \tilde{a}_1(t_i - t_0) + \tilde{a}_2(t_i - t_0)^2 + \tilde{a}_3(t_i - t_0)^3 \\ y_n = \tilde{b}_0 + \tilde{b}_1(t_i - t_0) + \tilde{b}_2(t_i - t_0)^2 + \tilde{b}_3(t_i - t_0)^3 \\ z_n = \tilde{c}_0 + \tilde{c}_1(t_i - t_0) + \tilde{c}_2(t_i - t_0)^2 + \tilde{c}_2(t_i - t_0)^3 \end{cases} \tag{60}$$

Transforming the slant range distances to the reference system, can be achieved if we observe that for the azimuth line i, the slant range distance in relation to the range coordinate j can be calculated as:

$$r_k(i,j) = \sqrt{(\hat{X}_e(i,j) - x_n(i))^2 + (\hat{Y}_e(i,j) - y_n(i))^2 + (\hat{Z}_e(i,j) - z_n(i))^2} \, , for \; j-1,...N$$
$$i = (t - t_0) \cdot f_{PR} \tag{61}$$

where N symbolizes the number of samples. With equations (58-61), the estimation of the SAR topography can be achieved in respect to the topographic slant range distance matrices and as such the topographic fringes that appear in the final product of this operation can be manipulated by different reference systems.
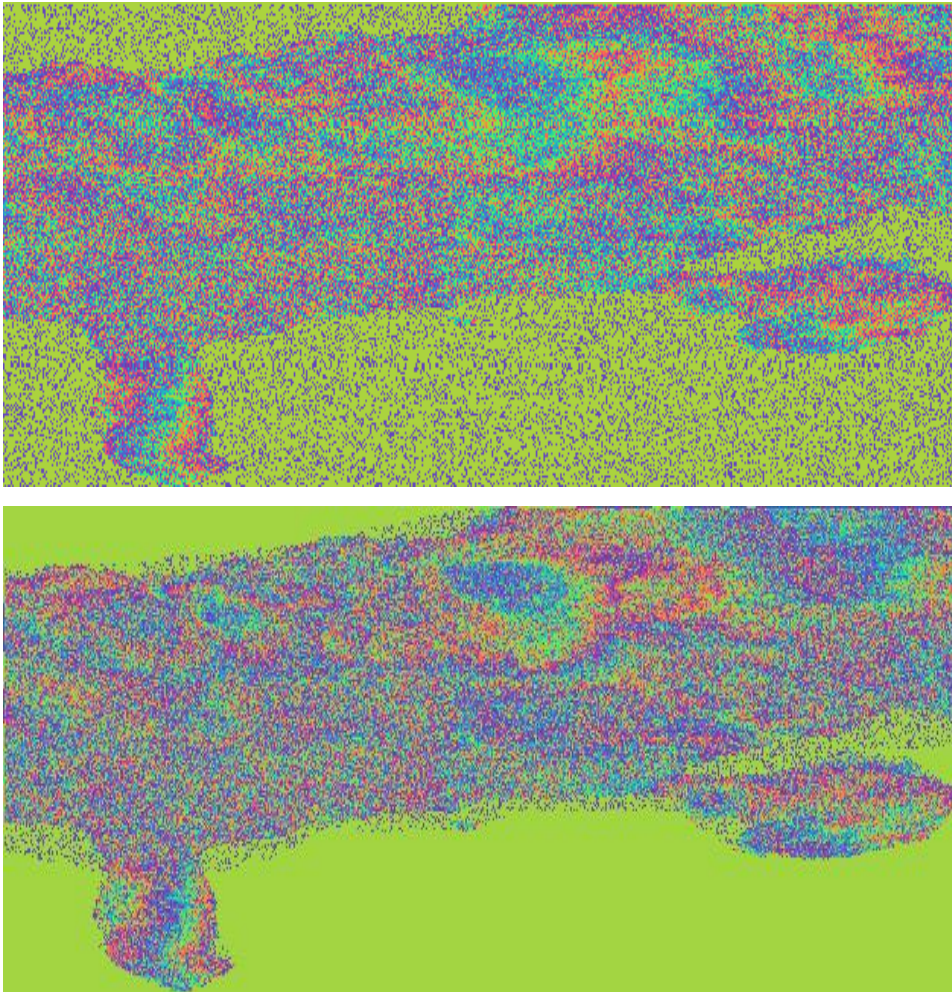
Figure 19. Phase Representation of Western Crete before (up) the topographic phase removal procedure and after (down). The White Mountain complex can be clearly seen in the top center of both images.

2.5 Differential Interferometry

Generation of Differential Interferograms is based on the exploitation of the phase difference between SAR data-pairs for the detection and estimation of the relative deformation occurred in the illuminated target area.
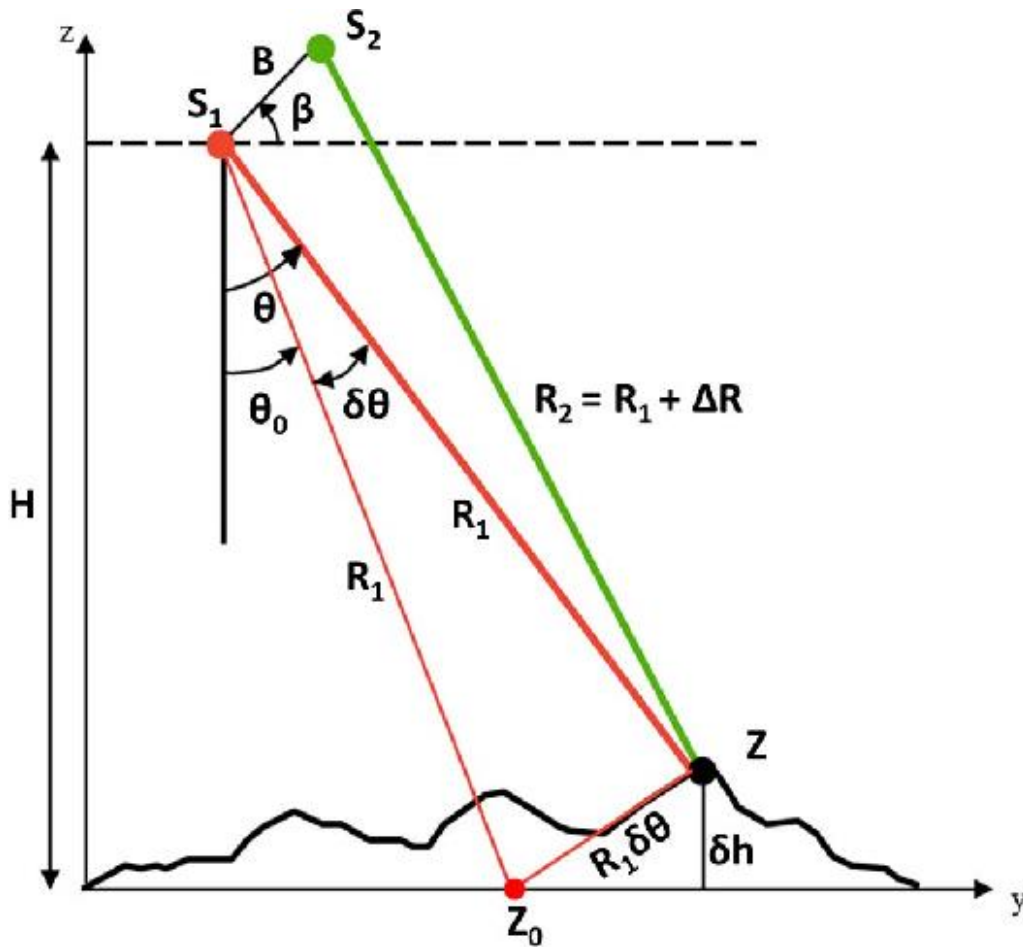
Figure 20. D-InSAR Geometry [56].

Assuming the geometry seen in Fig. 20, for a DInSAR pair, with a ground displacement d for a target point, range of R1 and R2 for master and slave images respectively, and the relevant target range being $\bar{r}$. The interferometric phase is given by

$$\varphi = \frac{4\pi}{\lambda} R_2 - \frac{4\pi}{\lambda} R_1 \tag{62}$$

and in regard to the geometry

$$\varphi = \frac{4\pi}{\lambda}(R_2 - \bar{r} + \bar{r} - R_1) = \frac{4\pi}{\lambda}(\delta r_d + \delta r) = \varphi_d + \varphi_r \tag{63}$$

where δr_d, representing the target displacement due to the path difference, and δr, the topography height profile, are distinguished.

If the two passes happen on the same exact orbit, then the topography contribution is equal to zero and the interferometric phase depends only to the δr_d

$$\varphi = \frac{4\pi}{\lambda}\delta r_d \approx \frac{4\pi}{\lambda}l_d \sin(\theta - a_d) \tag{64}$$

This is considered as an ideal situation which allows calculations with accuracy on the order of fraction of the wavelength.

In the realistic situations where the orbit is the same, the topography and displacement contributions must by estimated. A DEM of the area provides the topography information, z, of the target area. With the orbital information known, (can be seen in chapter 1), the synthetic interferogram is now given by

$$\varphi_d = \frac{4\pi}{\lambda}\delta r_d \tag{65}$$

which after the unwrapping procedure, provides the displacement component of the illuminated target area. The accuracy of this measurement is related to the achievable accuracy of the synthetic interferogram formation, which is dependent on the accuracy of the DEM.

The realistic expression of the DInSAR deformation phase is:

$$\Delta\Phi^{DInSAR} = \Delta\Phi^{deform} + \Delta\Phi^{orb} + \Delta\Phi^{top} + \Delta\Phi^{atm} + \Delta\Phi^{noise} \tag{66}$$

- $\Delta\Phi^{deform}$, refers to the deformation phase corresponding to the ground displacement that occurred between the acquisitions,

- $\Delta\Phi^{orb}$, refers to the orbital residual fringes due to the inaccurate knowledge of the SAR system position along the flight path,

- $\Delta\Phi^{top}$, is the residual topographic signal due to either incorrect DEM re-sampling into SAR coordinates and/or error in the knowledge of the topography

- $\Delta\Phi^{atm}$, is the atmospheric phase component that accounts for the troposphere inhomogeneities and its calculation can be seen later in this chapter,

- and $\Delta\Phi^{noise}$, which accounts for noise contribution.

Another important source of mis-interpretation is due to the fact that the phase retrieved from the SAR system is restricted to the [-п, п] interval. For this reason, the Phase Unwrapping (PhU) operation is used to restore phase to 2п phase jumps. However, in the PhU operation there are also errors, that are integer multiples of 2п, and as such can propagate in the data inversion process, which affect the deformation measurements.

From all the above, it is noted that to calculate and isolate only the deformation phase contribution and generate the time-series, proper processing and assumptions are needed to achieve results with no errors present.

The noise factor, $\Delta\Phi^{noise}$, comes from the observation that the power spectra of the interferograms is characterized by a component, that is generated by thermal noise and correlation loss. For this purpose, we use an adaptive filtering algorithm in the fringe spectrum, that is sensitive to fringe rate and local phase noise. The algorithm used, was proposed by Goldstein *et al.* [46], requires an interferogram to be properly divided to overlapping rectangular patches, where the power spectrum of each patch is computed by smoothing the intensity of the two-dimensional FFT. The adaptive filter is then computed from the power spectrum Z by

$$GPF(u,v) = |Z(u,v)|^a \tag{67}$$

Filter parameter a, ranges from 1 which indicates strong filtering, to 0 where no filtering occur. The achieved results of the filtering operation can be seen in Figure. 22, where $a = 0,8$ with a coherence mask of 0.2.
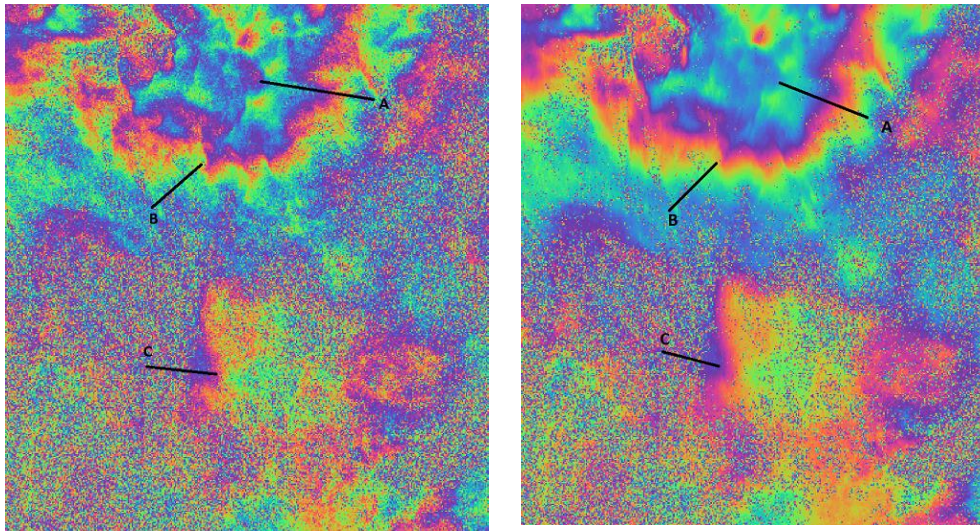
Figure 21. On the left, Representation of the phase before the filtering operation. A, B and C areas are affected by noise. On the right the same phase representation after the filtering operation. A, B and C areas after the filtering operation show no noise interference.

2.6 Deformation time-series

With the differential interferograms properly filtered, next step in the processing chain is the calculation of the deformation time-series. It is necessary for this step to be productive, to select as reference a non-deforming point in space, or a point whose deformation is known, where the estimated deformation from the interferograms will be referred to. This task can be achieved by creating a mask from the spatial coherence maps already generated. This mask, accounts for all the high coherence value pixels that are into a matrix whose dimensions are related to the multi-looked resolution cell. The purpose of point selection is to neglect the importance of areas with high decorrelation

effects that will be present in the overall analysis and most particularly in the phase unwrapping step.

Assuming a set of N+1 SAR images, which are acquired at times $(t_0,\ldots,t_N)$, and a sequence of M differential SAR interferograms, the time-series procedure can be explained in the following chain:

- Differential phases are unwrapped, so the full phase of the images can be exploited in the process.
- Estimation of the residual topography contribution after the unwrapping procedure.
- The unwrapped, corrected, phases are used in the time-series process that is carried out using either the Least-Square (LS) or the Singular Value Decomposition (SVD) algorithm. For this step to be successful, the chosen pair must satisfy the constraints that we imposed, regarding temporal and spatial baseline differences as well as the frequency shift. Furthermore, the interferograms must by properly linked.
- Calculation of the atmospheric contribution, which is then subtracted from the deformation time series.

2.6.1 Phase Unwrapping

The phase presented in the differential interferograms, is restricted to the [-π, π] interval, which hinders the exploitation of the full phase in properly extracting the deformation present in an area. To unwrap the phase to its proper value, it is required to use a non-linear operation that can achieve this goal. The unwrapping procedure has a lot of different approaches, that can range from unwrapping a single interferogram to multiple ones [47-50]. The procedure used in this step is based on the Minimum Cost Flow (MCF) network, that is applied to sparse data grid [50]. Assuming a generic point in SAR

coordinates of azimuth and slant range, (a_z, r_g), the unwrapping procedure has two parameters:

- The input, which is the wrapped phase signals $[\varphi_j(a_z, r_g)]_{i=0}^{M-1}$

- The output, which is the unwrapped phase signals $[\psi_j(a_z, r_g)]_{i=0}^{M-1}$

The procedure is explained analytically later in the chapter.

2.6.2 Residual topography contribution

Assuming a data-pair, its differential interferogram computed at times t_A and t_B with regards to its SAR coordinates (azimuth, slant range), is expressed as:

$$\psi_i = \frac{4\pi}{\lambda} \frac{b_{\perp,i}}{r \sin \theta'} \Delta z(a_z, r_g) + \frac{4\pi}{\lambda} [d(t_B, a_z, r_g) - d(t_A, a_z, r_g)] + \frac{4\pi}{\lambda} [d_{atm}(t_B, a_z, r_g) -$$
$$d_{atm}(t_A, a_z, r_g)] + \Delta n_i(a_z, r_g) \tag{68}$$

where λ is the signal wavelength (5.55 cm for Sentinel-1), θ' is the incidence angle (that can be retrieved from the orbit information), r the distance between sensor and the target, Δz is the unknown residual topography, $d(t_i, a_z, r_g)$ is the unknown deformation value of the SAR point at time t, $d_{atm}(t_i, a_z, r_g)$ is the atmospheric contribution and $\Delta n_i(a_z, r_g)$, refers to the noise. To calculate the residual topography term Δz, we exploit the linear dependency of the topographic phase component on the perpendicular phase values. Equation (64) can be rewritten as:

$$\psi_i(x, r) \cong \frac{4\pi}{\lambda} \left[\frac{b_{\perp,i}}{r \sin \theta'} \Delta z + v \Delta T \right] \tag{69}$$

which is easily solved using either the Least Squares (LS) or the Singular Value Decomposition (SVD) methodology. The evaluated residual topographic pattern, subtracted from each differential interferogram, leads to a novel system of phase (φ) equations that can be properly solved

$$\psi_i = \frac{4\pi}{\lambda}\left[d\left(t_B, a_z, r_g\right) - d\left(t_A, a_z, r_g\right) + d_{atm}\left(t_B, a_z, r_g\right) - d_{atm}\left(t_A, a_z, r_g\right)\right] + \Delta n_i\left(a_z, r_g\right) =$$

$$\varphi\left(t_B, a_z, r_g\right) - \varphi\left(t_A, a_z, r_g\right) \tag{70}$$

2.6.3. Time-series calculation

First step in the deformation time-series calculation, is to estimate the deformation present in the phase images. For this purpose, equation (66) is re-organized in a system of matrices:

$$\Omega \cdot \Phi = \Psi \tag{71}$$

Where Ω, is defined as a matrix directly related to the generated-interferograms set and is defined by:

$$\begin{cases} \Omega(i, MI_i) = 1, & MI \neq 0 \\ \Omega(i, SI_i) = -1, & SI \neq 0 \\ \quad 0, & otherwise \end{cases} \tag{72}$$

where **MI** and **SI**, represent the vectors that include the indices of the master and slave time acquisitions (t_0, …, t_N), respectively. The rank of matrix Ω, is M-1 with the requirement that all SAR acquisitions are connected. System equation (67) is considered well-determined for N=M-1, or over-determined if N>M-1. Using the Least Squares (LS) methodology, the solution of this system is:

$$\Phi = \Omega^+ \cdot \Psi = \{(\Omega^T \cdot \Omega)^{-1} \cdot \Omega^T\} \cdot \Psi \tag{73}$$

Ω^+ is the left inverse matrix. In the presence of different subsets, the rank of matrix Ω, is reduced according to the number of different subsets. In this case, the singular value decomposition (SVD) method is used to invert the system. Matrix Ω can be written as:

$$\Omega = U \cdot S \cdot V^T \tag{74}$$

Sub-matrix U is an $M \times M$ orthogonal matrix, whose first N columns are the eigenvectors that are derived from matrix $\Omega^T \cdot \Omega$. Sub-matrix S, is a diagonal $M \times M$ diagonal matrix, that is filled with the singular values and sub-matrix V is an $N \times M$ orthogonal matrix, that

is filled with the eigenvectors of matrix $\Omega^T \cdot \Omega$. The solution for Φ is now computed via equations (69, 70):

$$\Phi = \sum_{i=1}^{N-l+1} \frac{\psi^T \cdot u_i}{\sigma_i} v_i \tag{75}$$

where l, is the number of subsets present in the data pairs.

Although this solution is simplistic and can produce results in the time-series problem, due to usage of minimum norm criterion on the deformation phase Φ, it introduces large discontinuities in the final product. A solution to this problem, is by re-ordering the system (68) and introducing the mean-phase velocity between the adjacent acquisitions,

$$v = \left(v_1 = \frac{\Phi_1 - \Phi_o}{t_1 - t_0}, \dots, v_N = \frac{\Phi_N - \Phi_{N-1}}{t_N - t_{N-1}} \right) \tag{76}$$

The new system of equations is now,

$$B \cdot v_d = \Psi$$

The new matrix B dimensions are *M x N* and is filled using the following set of parameters:

$$B[i,j] = \begin{cases} t_{j+1} - t_{j,} & MI \le j \le SI \\ 0, & otherwise \end{cases} \tag{77}$$

The mean-phase velocity can be calculated using the Least-Square or the Singular Value Decomposition technique in relation to the new matrix B. The difference with the simplistic usage of matrix Ω is that in order to compute the deformation phase there is an extra integration step required:

$$\begin{array}{c} \Phi(t_i) = \sum_{n=1}^{i} v_{dn}(t_n - t_{n-1}), \quad \forall i = 1, \dots, N \\ \Phi(t_0) = 0 \end{array} \tag{78}$$

For the calculation of deformation phase, we have to take into account that using a large number of conditions (system (74)), may lead to additional deformation pattern that are inconsistent to the original fringe phase. For this purpose, an additional procedure is introduced. This procedure involves the reconstruction of the phase, pixel by pixel, using the achieved phase Φ and the residual topography:

$$\varphi_i = \frac{4\pi}{\lambda} \frac{b_{\perp i}}{r \sin \theta} \Delta z + [\Phi(t_{MI}, x, r) - \Phi(t_{SI}, x, r)] \tag{79}$$

2.6.4 Atmospheric Filtering

The next step in the deformation time-series processing chain is the atmospheric filtering (AF) operation. The operation used in this thesis can be mainly found in [51]. It is based on the observation that the atmospheric phase component is poorly correlated in time, but highly in space, and so the APC calculation can be divided into three steps:

1. Low Pass (LP) long-term deformation signal estimation,
2. High Pass (HP) temporal component estimation,
3. Atmospheric phase component retrieval.

The Low Pass component of deformation (d_{LP}) can be calculated using a moving average operation, in time domain

$$\Psi'^{LP}_i(x,r) = \frac{4\pi}{\lambda} d_{LP}(t'_i, x, r) \tag{80}$$

The High pass component can now be estimated by subtracting the LP phase component from the overall deformation phase

$$\Psi'^{HP}_i(x,r) = \Psi'(x,r) - \Psi'^{LP}_i(x,r) \tag{81}$$

The high pass component is directly related to the residual topography components and the overall atmospheric phase component

$$\Psi'^{HP}_i(x,r) = \Psi'^{\Delta z}_i(x,r) - \Psi'^{atm}_i(x,r) = \frac{4\pi}{\lambda} d^{HP}(t'_i, x, r), \quad \forall i = 0, \dots, N \tag{82}$$

where

$$\Psi'^{\Delta z}_i(x,r) = \frac{4\pi}{\lambda} \frac{b'_{\perp i} - b'_{\perp 0}}{R \sin \theta} \Delta z(x,r), \quad \forall i = 0, \dots, N \tag{83}$$
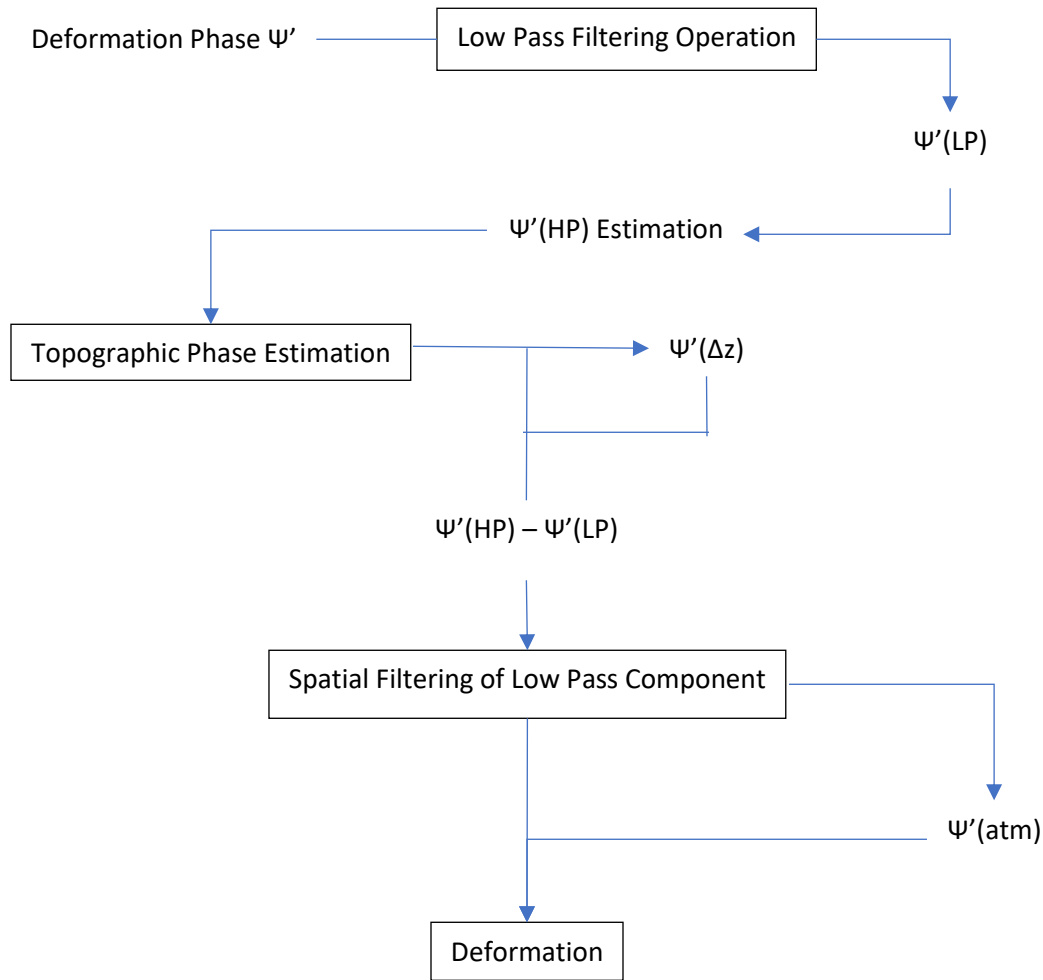
Figure 22. Calculation Chain for the retrieval of the atmospheric phase component.

The atmospheric phase component can now be retrieved

$$\Psi'^{atm}_i(x, r) = \frac{4\pi}{\lambda} d_{atm}(t'_i, x, r), \forall i = 0, \dots, N \tag{84}$$

With the APC term estimated, it can now be subtracted to the original interferograms resulting in a sequence of differential interferograms that can be re-processed via the samesteps of the processing chain.

2.7 Geocoding operation

The products of the deformation processing chain are obtained in the reference geometry coordinates of the SAR system. For this purpose, they have to be geolocalized onto a cartographic reference grid [52]. The strategy used for the Sentinel-1 products, is the Range-Doppler algorithm [53-54] and its main principles used in the process are described below.

First is the consideration of the SAR image formation, where the SAR processing algorithm is considered as a two-dimension (azimuth, slant range) compression of the echo signal using the range cell migration correction [53]. The effect of this correction is based on the fact that the distance of the illuminated target is related to the SAR system moving with time. The backscatter echo signal migration throws the adjacent range cell during this movement and thus, the azimuth signal of this target point is concentrated to a migration curve. After the range compression, the azimuth compression is performed through referencing the echo signal with a function. Second, is the relation of SAR processing in the Range-Doppler (RD) algorithm. The equation relating the migration curve with the RD domain is

$$R(f) = \frac{R\sqrt{1 - \frac{\lambda^2 f_{DC}^2}{4v_x^2}}}{\sqrt{1 - \frac{\lambda^2 f_D^2}{4v_x^2}}} \tag{85}$$

where v is the reference velocity of the system, f_{DC} is the mean Doppler frequency, f_D the azimuth Doppler frequency and R the slant range. The last principle is the multi-look processing and is based on the fact that the SAR interferograms depict the same scene taken from different trajectory segments. The procedure is done in the frequency domain, based on the fact that the whole scene can be processed in the whole of the Doppler bandwidth divided into smaller bands. The length of each band is determined by the required azimuth resolution

$$BW(\rho_x) = K_w \frac{v_x}{\rho_x} \tag{86}$$

(ρ is the azimuth resolution and K is the coefficient of the weighted window). The whole spectrum width is determined by the antenna beam width θ_α as

$$BW_A = \frac{2}{\lambda} v_x \theta_a \tag{87}$$

The number of SAR looks can now be achieved by,

$$N_o L = int \left[\frac{BW_A}{BW(\rho_x)/2} \right] - 1 \tag{88}$$

The next step is to transform each SAR pixel to its corresponding point in the reference grid system (x, y, z), using a non-linear system of equations for the N unknowns

$$\begin{cases} r = |s(t) - N| \\ v(t) \cdot (s(t) - N) = 0 \\ \frac{x^2 + y^2}{(a+h)^2} + \frac{z^2}{(b+h)^2} = 1 \end{cases} \tag{89}$$

where h is the height of the target point in respect to the ellipsoid. With the above system solved, the points can now be transformed to the cartographic projection (WGS84).
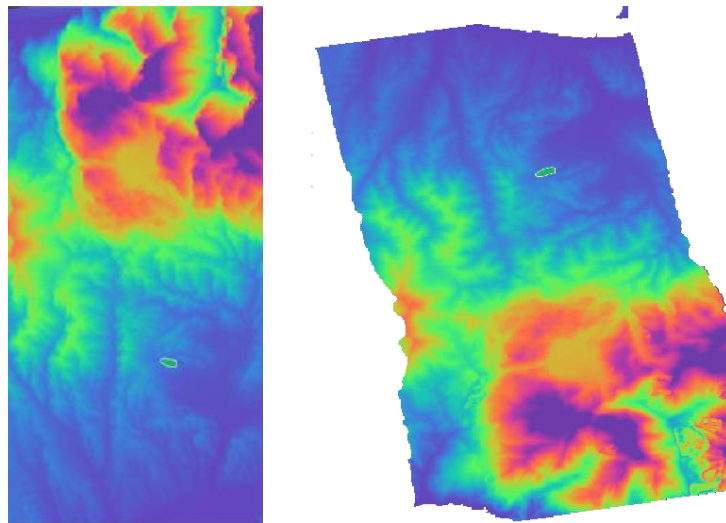
Figure 23. Topographic phase map of a wide area located in Western Crete before (left), and after (right) Range-Doppler Correction. (Polygon shows the location of Valsamiotis Dam).

2.8 Phase Unwrapping Introduction

As stated before, the measured phase of the data-pairs that form the interferograms are restricted to the [-π, π[interval, which means that an integral part of the phase cycles, attributed to the full 2π phase jumps, is lost.
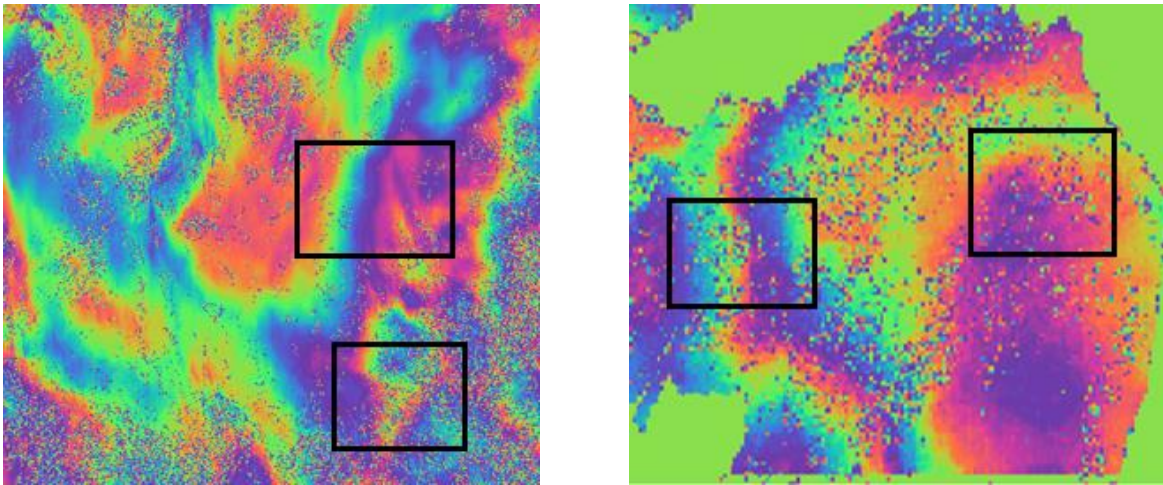
Figure 24. Wrapped phase-images of Western Crete. The fringe pattern in the images represents elevation change.

The inversion procedure of recovering the missing cycles and the reconstruction of the 2π phase jumps on the wrapped interferograms is known as Phase Unwrapping (PhU). All the existing phase unwrapping techniques key point, is the determination of the discrete "derivatives" of the unwrapped phase, namely the neighboring pixel difference, where the absolute value of these differences is less than π. Using these differences, the unwrapped phase is then reconstructed by using an additive constant. The phase-unwrapping problem is presented below, followed by the presentation of the basic algorithm methods used, and lastly the presentation and further analysis of the method used in this thesis, Minimum Cost Flow (MCF) algorithm.

2.9 Phase Unwrapping Problem

As stated before, the phase unwrapping is related with the evaluation of the full interferometric phase of a wrapped phase image. Assuming a differential interferogram with $\varphi(a_z, r_g)$ interferometric phase in SAR coordinates, the full interferometric phase $\psi(a_z, r_g)$ is directly related to the calculated deformation $d(a_z, r_g)$ by:

$$d(a_z, r_g) = \frac{\lambda}{4\pi} \psi(a_z, r_g) \tag{90}$$

where the full interferometric phase is computed from the wrapped one by integers of 2π

$$\psi(a_z, r_g) = \varphi(a_z, r_g) + 2\pi H(a_z, r_g) \tag{91}$$

To solve the problem of unwrapping, we assume that the data-pair can be translated from SAR coordinates to a function of discrete coordinates (i, j)

$$\begin{aligned} a_z &= a_{z0} + i\frac{v_S}{PRF} \\ r_g &= r_{g0} + j\frac{c}{2f_{samp}} \end{aligned} \tag{92}$$

where (a_{z0}, r_{g0}) are the coordinates of the first line, v_S is the sensor velocity, PRF the pulse repetition frequency, c the speed of light and f_{samp} is the range sampling frequency. The partial derivatives can be re-defined by using the phase gradient vector:

$$\widehat{\nabla}\psi = \langle \Delta_x \psi \rangle \hat{x} + \langle \Delta_y \psi \rangle \hat{y} \tag{93}$$

In respect to the x, y axis the two components are calculated by:

$$\begin{aligned} \langle \Delta_x \psi(i,j) \rangle_{-\pi,\pi} &= \langle \psi(i+1,j) - \psi(i,j) \rangle_{-\pi,\pi} = \langle \varphi(i+1,j) - \varphi(i,j) \rangle_{-\pi,\pi} \\ \langle \Delta_y \psi(i,j) \rangle_{-\pi,\pi} &= \langle \psi(i,+1j) - \psi(i,j) \rangle_{-\pi,\pi} = \langle \varphi(i,j+1) - \varphi(i,j) \rangle_{-\pi,\pi} \end{aligned} \tag{94}$$

The measurable phase gradient of the above operations, can be now used even for phase differences greater than π in the [-π, π] interval. We have to take into account that the phase difference may exceed this interval, due to noise level (depending on the coherence value) and the slope of the residual topography. For this reason, an operator is introduced that is not conservative and whose integration is path dependent:

$$rot(\widehat{\nabla}\psi) = \nabla \times (\widehat{\nabla}\psi) \neq 0 \tag{95}$$

The phase gradient estimation advantage is that the errors that may occur, are constrained locally and are in integer 2π multipliers and thus, they can be used to the reconstruction of the full phase term. One of the key points of the unwrapping procedure is the residue field

$$r(i,j) = \nabla \times \left(\widehat{\nabla}\psi(i,j)\right) = \Delta_x \left[\langle \Delta_x \psi(i,j)\rangle_{-\pi,\pi}\right] - \langle \Delta_y \psi(i,j)\rangle_{-\pi,\pi} \tag{96}$$

with values ranging from 2π, positive or negative residue, to 0, no residue. The residues are the result of two possible sources:

- Discontinuities in the data; they are formed in the fringe spacing on certain slopes in topography or from large-observation displacements that exceed the half-cycle spacing criterion,
- Noise present in the data-set; either from thermal and/or other noise sources, or from decorrelation that is formed due to temporal changes in the illuminated area or from baseline length.

2.10 Phase Unwrapping Algorithms

2.10.1 Branch-cut Algorithms

The branch-cut (or residue-cut) methods key point is the use of the partial derivatives to unwrap the phase. Basically, the derivatives of the unwrapped phase are integrated into paths that will give self-consistent results [47]. Those paths are limited by non-crossed paths that are made due to the local inconsistencies of the estimated discrete partial derivatives. The limitation of these method, is that it is performed locally and do not follow a global approach.
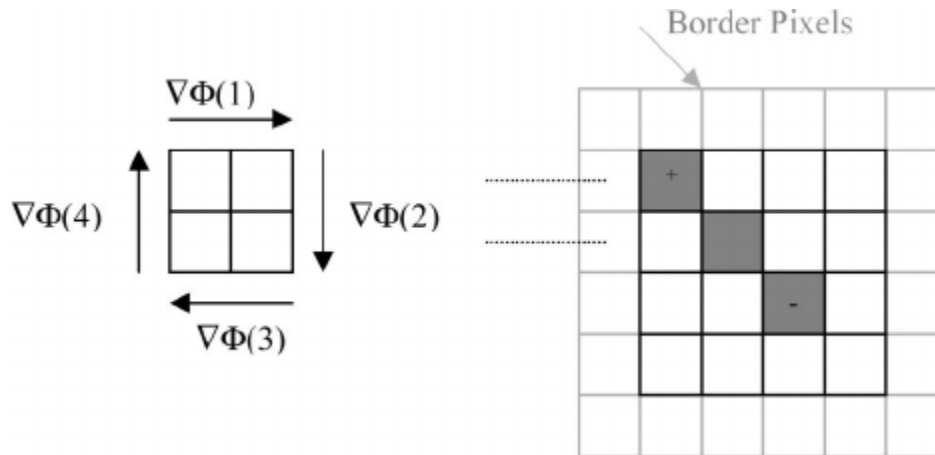
Figure 25. Representation of the residue calculation on a branch-cut [62].

The tree-growth of the residue-cut algorithm consist of the following steps:

1. Identification of residues which are then marked as negative or positive
2. Interferogram phase is scanned until location of residue
3. Surround are of residue is scanned until another residues is located. Then a cut is formed between them and the total charge is computed
4. If total charge is zero then the tree is complete and the scan jumps to step 2
5. If total charge is non-zero, the scan continues until nearby residues are located. In each residue found, the tree computes the total charge until the sum is zero and the procedure continues from step 2.

Inside the procedure, all residues that may have been previously assigned to a tree, can be assigned to a new tree which yields the dendritic approach of the cuts and the nomenclature, trees. When a boundary of the interferogram has been reached, the cut is drawn to the boundary and the tree is complete and deemed that it has no charge, a property that prevents trees from isolating areas of the image. In residue-rich regions however, the tree may grow overly dense, and thus isolating the remainder of the image and as a result no unwrapped phase estimate is calculated. In conclusion, the branch-cut algorithms provide results that can be free of mistakes and errors due to the conservative

approach in the solution of the unwrapping phase problem, but this conservative approach comes with the expense of providing incomplete unwrapping results.

2.10.2 Least-Squares Algorithms

The least-square (LS) approach on the phase unwrapping problem was proposed by Ghiglia and Romero [59], and it utilized the application of the well-known mathematical formalism in the SAR interferometry environment. This algorithm is based upon the fact that the cosine transformation permits efficient and accurate inversions, through the usage of the least-square formalism, in even very large matrices that may occur in the phase unwrapping problem. The vector gradient of the phase shift, obtained by the solution of the least-squares algorithm, is well determined and is then integrated as part of a smooth solution. The main difference between the LS and the Branch-cut approach, is that in the branch-cut algorithm only the integral numbers of phase cycles are added to the final result, while in the LS approach, any value can be added to ensure continuity and smoothness to the final result.

The LS algorithm has two main approaches, the unweighted and the weighted approach. The unweighted approach can be expressed as the discrete form of Poisson's equation and can be solved using the discrete cosine transformation,

$$\left(\varphi_{i+1,j} - 2\varphi_{i,j} + \varphi_{i-1,j}\right) + \left(\varphi_{i,j+1} - 2\varphi_{i,j} + \varphi_{i,j-1}\right) = \left(\Delta_{i,j}^x - \Delta_{i-1,j}^x\right)\left(\Delta_{i,j}^y - \Delta_{i,j-1}^y\right) \quad (97)$$

The weighted approach is used when there are known points in the interferograms that are deemed well known and reliable, and so a matrix is introduced which contains those weights, W.

$$Ws = W\Omega\varphi + n \qquad (98)$$

where s is obtained by the row and columns of the phase difference and n is a vector that represents the noise. Although equation (95) cannot be transformed to a Poisson equation

where the cosine transformation can be used, Ghiglia and Romero proposed a convergence criterion to solve the new equation,

$$\frac{\sum_{all\ i,j}\left|\varphi_{i,j}^{l+1}-\varphi_{i,j}^{l}\right|^{2}}{\sum_{all\ i,j}\left|\varphi_{i,j}^{l+1}\right|^{2}}\leq\in \tag{99}$$

where $\in$ is equal to a conservative value of 10^{-12} which ensures the limitation of round-off errors. The accuracy of this solution depends on the correct choice of weights to be applied to each points of the measured phase.

However, neither of these approaches (weighted and unweighted) uses the residue information which is inherent to any set of data-pairs and have to be accounted when applying the unwrapping procedure, as it ensures continuity and consistency and minimize the appearance of errors in the final results.
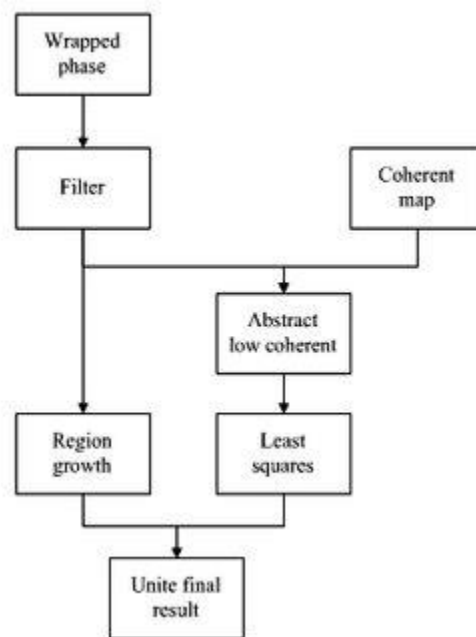
Figure 26. Least-squares flow chart [63].

2.10.3 Synthesis Algorithm

The synthesis algorithm was proposed by Zebker and Lu [60] and its main focus was to overcome the limitation of the branch-cut and the least-square algorithms. The main points of this approach are

- Utilization of the global approach present in the Least-square formalism
- Non-continuous unwrapped phase-field approach of the branch-cut algorithm
- Weighted approach (eq. 95) and,
- Tree calculation of the branch-cut; if the weight is zero then there is no constraint to the implied continuity at the points of the tree.

In this approach, results with true discontinuities and very noisy areas can be obtained, which was the problem with the conservative approach of the branch-cut algorithm. The accuracy of the synthesis algorithm lies with the correct choice of the weight accorded to each phase estimate. Zero weight is assigned along the branches and the rest of the weights are assigned to decorrelation, signal strength and noise.

2.11 Minimum Cost Flow Algorithm (MCF)

The Minimum Cost Flow (MCF) algorithm belongs to the wide branch-cut approach. It was proposed by Costantini [61] in 1998, and it suggests that the phase unwrapping problem can be formulated into a global minimization problem with integer variables; basically, it equates the PhU problem to a problem where the solution is finding the minimum cost flow network, an approach where efficient techniques for its solution already exist.

The key point of this technique is the exploitation of the fact, that the discrete derivatives are estimated with errors that are integer multiples of 2π. The weighted deviation between known and unknown discrete derivatives is minimized due to the constriction imposed by 2π differences. With the constraint in place, the spreading of any occurrent errors is

contained, which means that the unwrapped phase is identical to the wrapped phase when re-wrapped, and the unwrapped results are less sensitive in respect to the used weighting mask.

Assuming a rectangular grid S (i, j) where i ranges from 0 to N-1 and j from 0 to M-1, S_0 subset of S where i=0, …, N-2 and j=0, …, M-2, subset S_1 with i=0, …, n-2 and j=0, …, M-1 and finally subset S_2 with i=0, …, N-1 and j=0, …, M-2. Now, assuming real function F(i, j), its discrete partial derivatives are obtained by:

$$\Delta_1 F(i,j) = F(i+1,j) - F(i,j) = F_1(i,j), \quad (i,j) \in S_1$$
$$\Delta_2 F(i,j) = F(i,j+1) - F(i,j) = F_2(i,j), \quad (i,j) \in S_2 \tag{100}$$

The above equations are true when,

$$F_1(i, j+1) - F_1(i,j) = F_2(i+1,j) - F_2(i,j), \quad (i,j) \in S_0 \tag{101}$$

The function F can now be re-written using an integration formula as

$$F(i,j) = A + \sum_{i'=0}^{i-1} F_1(i',0) + \sum_{j'=0}^{j-1} F_1(0,j') \tag{102}$$

Introducing a new real function $\Phi(i, j)$ belonging to the S grid, obtained by

$$\Psi(i,j) = \Phi(i,j) + 2\pi n(i,j) \tag{103}$$

where $\Psi \in$ [-π, π). $\Phi(i,j)$ and $\Psi(i,j)$ are the unwrapped and wrapped phase functions respectively. Using the discrete partial derivatives of the unwrapped phase we now have

$$\Psi_1(i,j) = \Delta_1 \Psi(i,j) + 2\pi K_1(i,j) \tag{104}$$

$$\Psi_2(i,j) = \Delta_2 \Psi(i,j) + 2\pi K_2(i,j) \tag{105}$$

The phase unwrapping problem can now be restated from the inversion of equation (103) to finding the discrete derivative residuals:

$$K_1(i,j) = \frac{1}{2\pi}[\Delta_1 \Phi(i,j) - \Psi_1(i,j)] \tag{106}$$

$$K_2(i,j) = \frac{1}{2\pi}[2\Phi(i,j) - \Psi_2(i,j)] \tag{107}$$

Residuals K_1 and K_2 are the solutions of the following minimization problem

$$\min_{(k_1,k_2)}\left\{\sum_{i=0}^{N-2}\sum_{j=0}^{M-1}c_1(i,j)|k_1(i,j)| + \sum_{i=0}^{N-1}\sum_{j=0}^{M-2}c_2(i,j)|k_2(i,j)|\right. \tag{108}$$

where the function c(,) is the cost function that allows us to individuate the areas where the branch-cuts are likely to exist or unlikely. The solution of the minimization problem of the above equation can be obtained using the follow variable changes:

$$K_x^+ = \min[0, K_x(i,j)] \tag{109}$$

$$K_x^- = \min[0, K_x(i,j)] \tag{110}$$
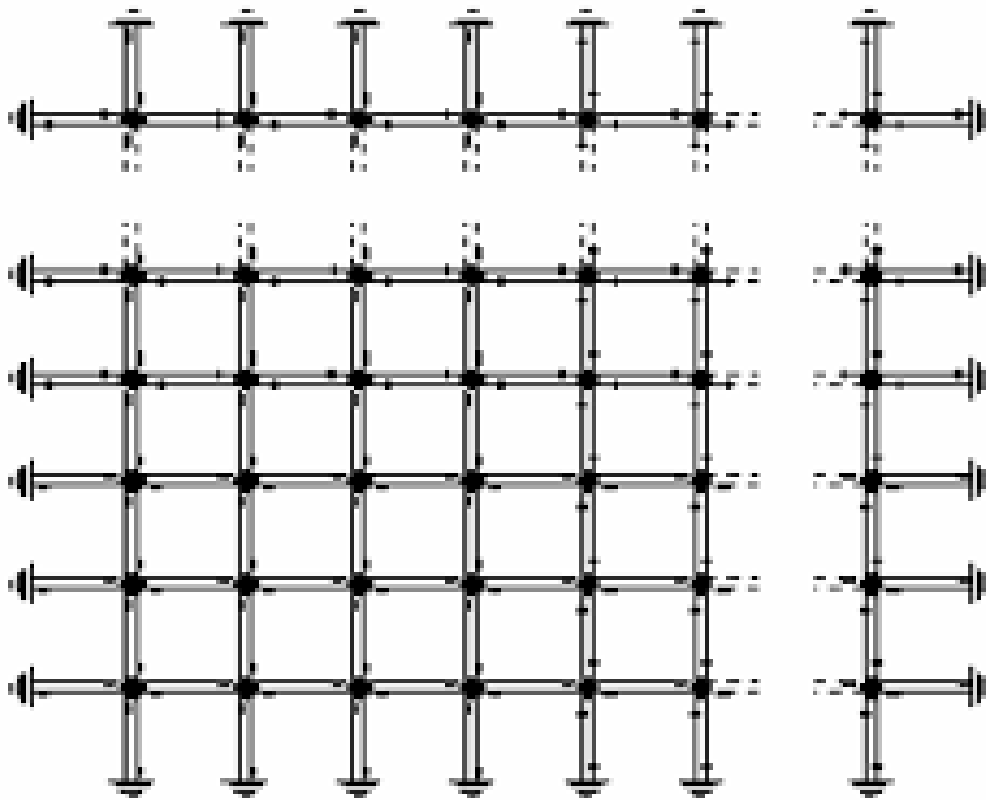
Figure 27. Representation of the 2π-multiples integer network.

$$K_y^+ = \min[0, K_y(i,j)] \tag{111}$$

$$K_y^- = \min[0, K_y(i,j)] \tag{112}$$

Equations (109)-(112) can be re-written via the following linear problem

$$min_{K_xK_y}\left\{\sum_i\sum_j\left[c_x(i,j)K_x^+(i,j) + c_y(i,j)K_y^+(i,j)\right] + \left[c_x(i,j)K_x^-(i,j) + c_y(i,j)K_y^-(i,j)\right]\right. \tag{113}$$

Equation (113) is the formulae of the minimum cost flow problem for the networks present in the unwrapping. With the network solved, the solutions can be expressed in respect to their integer 2п-multiplied functions

$$K_x(i,j)=K_x^+(i,j)-K_x^-(i,j)$$
$$K_y(i,j)=K_y^+(i,j)-K_y^-(i,j) \tag{114}$$

Using equations (103) and (114), the wrapped phase can now be unwrapped.

$$\nabla\psi = \widehat{\nabla}\psi + 2\pi K \tag{115}$$
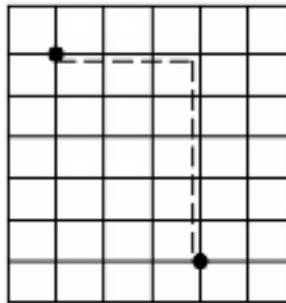
Figure 28. Formulation of the MCF unwrapping procedure via equation (100).
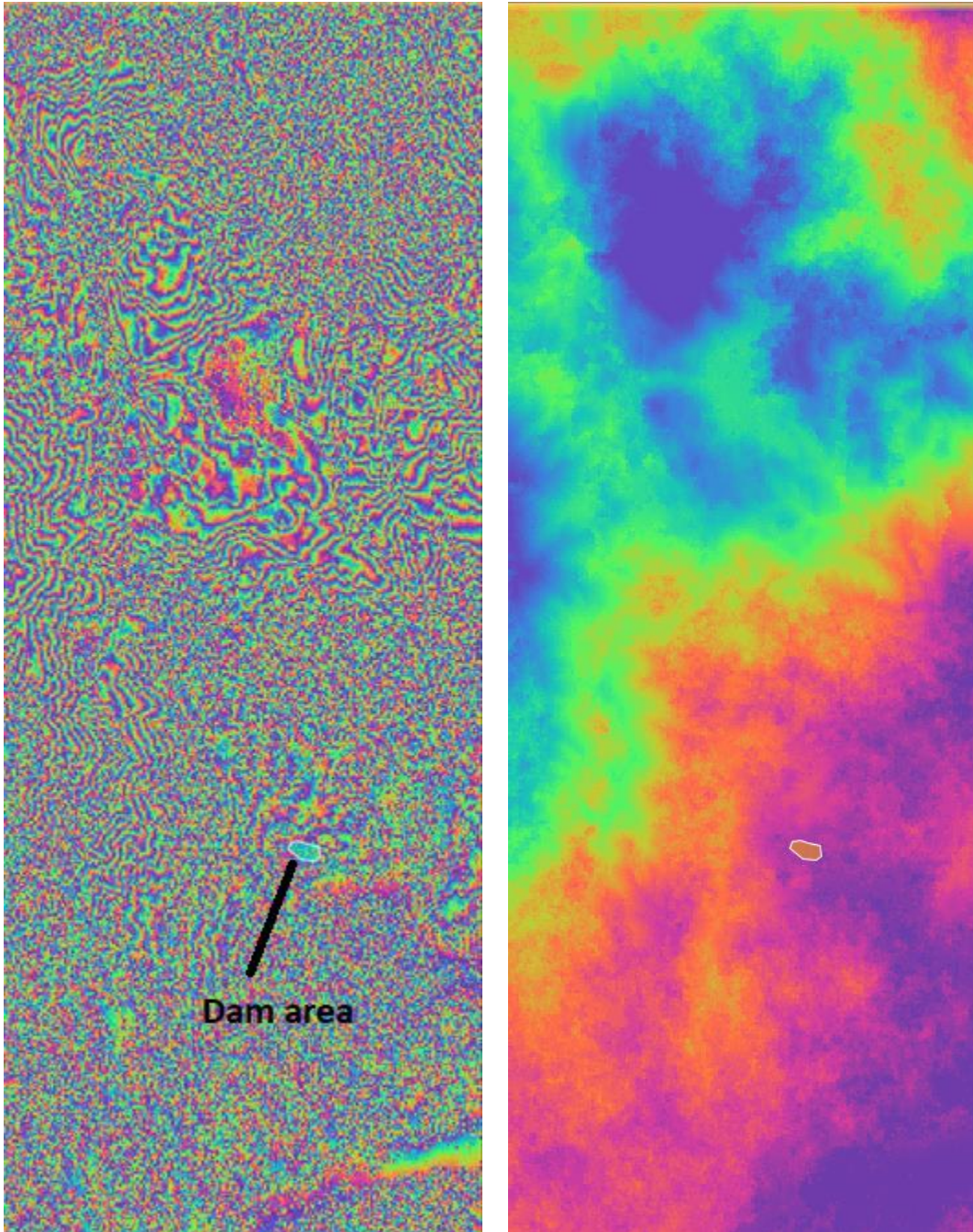
Figure 29. Wrapped (left) and Unwrapped phase image (right). MCF algorithm was used for the unwrapping (polygon shows the location of Valsamiotis dam).
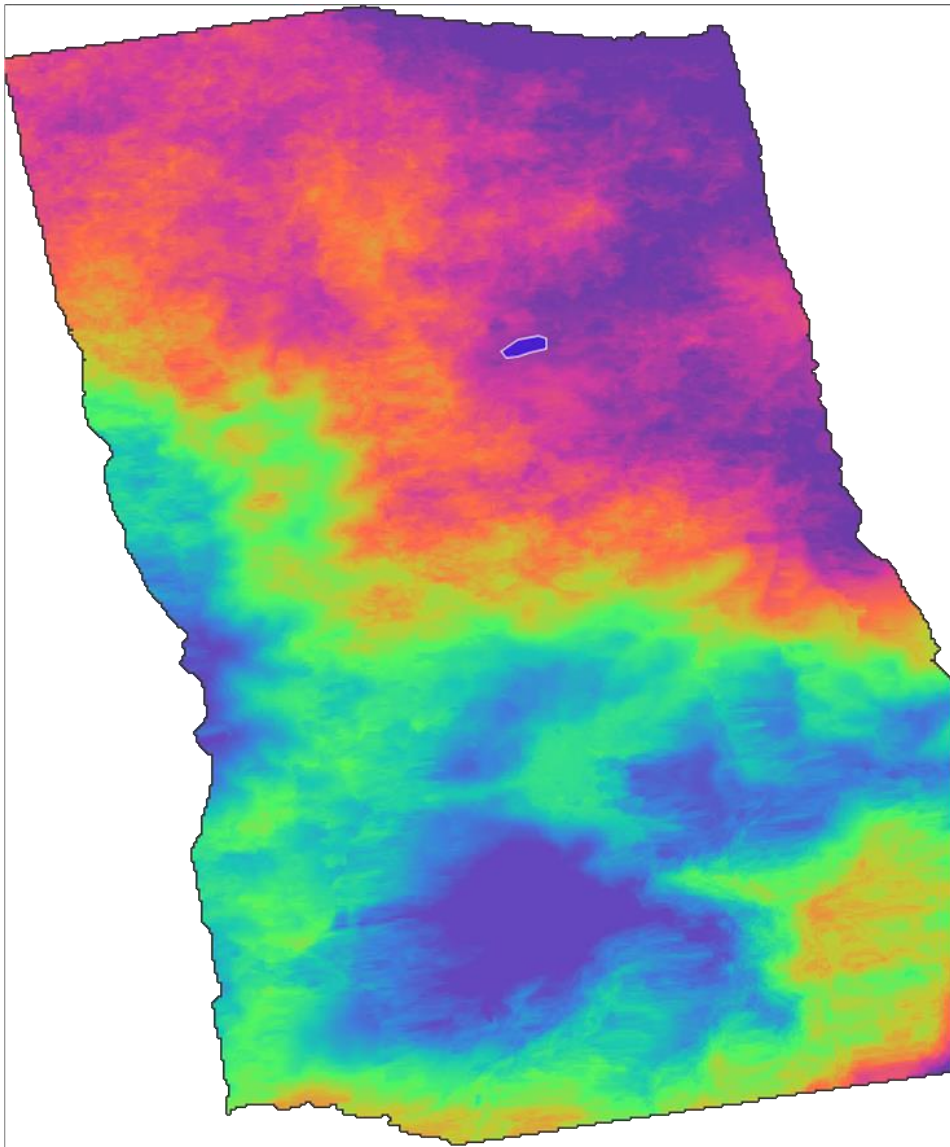
Figure 30. Unwrapped Geocoded phase image (polygon shows the location of Valsamiotis dam).

2.12 Small Baseline Differential SAR Interferometry (SBAS) on Sentinel-1 data

Sentinel-1 twin constellation of satellites -1A and -1B offers a large spatial coverage, while the images are acquired through a C-Band SAR system. By using the Differential Synthetic Aperture Radar Interferometry processing chain, we can investigate the deformation phenomena in covered areas, with a centimeter to millimeter accuracy. As stated before, Sentinel-1 is benefitted and limited by its capabilities, mostly its TOPSAR acquisition mode and the steering of the antenna in the azimuth domain. Although TOPSAR offers larger spatial coverage than other SAR acquisition methods, it is limited by the burst mode and the azimuth steering leads to changes in the Doppler centroid during the acquisition. The obtained illuminated scene of the Sentinel-1 is divided into three main swaths, with each one being further divided into multiple subswaths (figure 31).

The variation of the Doppler Centroid during the burst acquisition mode of the Sentinel-1 is one challenge that has to be solved during the analysis of the obtained images due to the:

- Fast change during the acquisition that can lead to mis-registration, and
- Discontinuous Doppler centroid in the burst transitions leading to phase jumps.

For this reason, the Enhanced Spectral Diversity procedure is critical in the opening stages of the processing chain in the DInSAR method for Sentinel-1 images, as it is used to compensate those Doppler centroid changes.
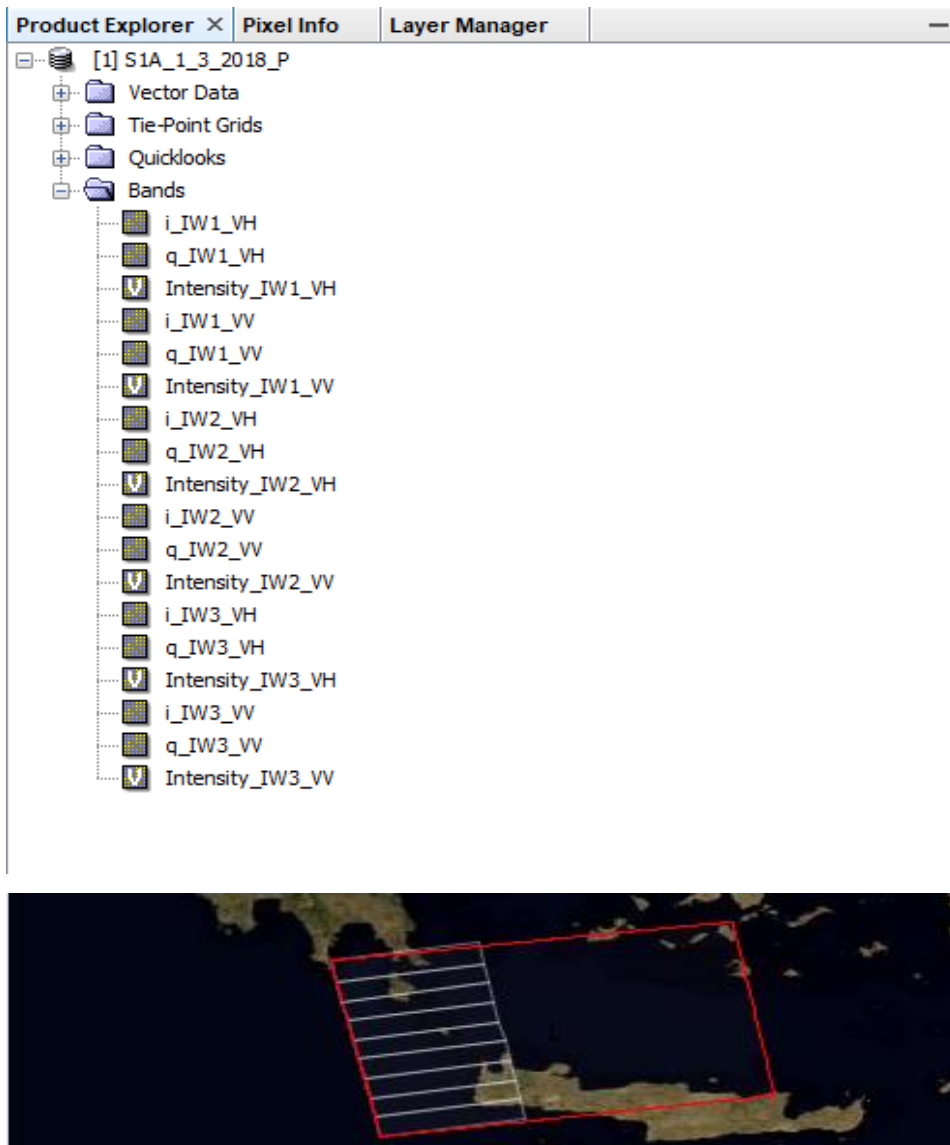
Figure 31. Top: The products of Sentinel-1 Level-1 SLC data. Bottom: One main swath is divided into further sub-swaths. (Source: ESA for the data, program used for the images SNAP-Desktop).

Another major factor is the burst existing between the sub-swaths that is depicted as a straight black line in the image (Figure 4), and so an operation, named de-bursting, must take place to remove this burst effect; this procedure can lead to phase jumps and errors in the image phase due to the procedure of the spectral overlap that removes the burst lines, errors that stay present in all the remaining steps of the procedure.

The DInSAR is also limited by two error sources; the atmospheric inhomogeneities present when the acquisition takes place and the inaccuracies of the DEM that is required in removing the topography component of the interferogram. To solve those errors, any algorithms purpose is to solve the system of linear equations, interferograms, which can be represented as

$$\hat{\psi}_{t_b,t_a} = \varphi_{t_b} - \varphi_{t_a} \tag{116}$$

It must be noted that those algorithms mainly differentiate on the selection of the interferogram generation criteria, but each one utilizes large stacks of phase images that exploit the time variable to overcome the error sources.

The interferogram selection can be described as the selection between one of the two main strategies. Considering the Temporal/Perpendicular baseline plane, we can plot our SAR acquisition distribution as can be seen in Figure 16. The larger the perpendicular and/or temporal (time domain) baseline are, the more present will be the decorrelation phenomena on the interferogram; for the Sentinel-1 the difference in the perpendicular baseline values is not an issue.

Assuming a set of *N+1* images acquired by SAR of the same target area, one of the main strategies used for DInSAR analysis is the Permanent Scatterers (PS); the idea is to generate a set of interferograms between each single SAR image with a single Master one; the system of equations is well determined in this technique. For the PS case, there may be interferograms that have perpendicular baselines with value greater than the critical one (1200m) which are strongly affected by the decorrelation noise. Due to this issue, only the phases of properly chosen point-wise Scatterers are retrieved for the interferometry chain. The pixels are selected due to their amplitude stability along a set of images, with a minimum requirement of 30 scenes, and are imposed to radiometric calibration. It is worth noting that with PS the maximum resolution of the SAR images is preserved, as the multi-look operation is not used.

The Small Baseline (SBAS) method's aim, is the preservation of the spatial and temporal correlation characteristics of the interferograms. This is done by imposing certain criteria on the allowed spatial and temporal baseline values. The result of those criteria is the mitigation of the noise effects on the interferograms, which can be achieved even by the presence of more than one independent acquisition subsets that have to be linked with each other. As a result, equation (113) is led to a non-determined system with rank deficiency. The non-invertible system is solved with the addition of the Singular Value Decomposition (SVD) method, that belong to the Least Square (LS) formalism.

The SBAS strategy provides the freedom of selecting different master images for the master-slave pairs in the generation of the interferograms, that is based on the criteria that the user imposes on the system. The number of possible generated interferograms, M, must satisfy the following inequality

$$\frac{N+1}{2} \leq M \leq N\left(\frac{N+1}{2}\right) \tag{117}$$

The two key-strategies of PS and SBAS led to the development of several algorithms that can be found in the literature. The Stanford Method for Persistent Scatterers (StaMPS) [64], the Permanent Scatterers (PrmS) [66], the Coherent Point Target Analysis (CPTA) [67], the Spatio-Temporal Unwrapping Network (STUN) [68] and many more.

Chapter 3

DInSAR Analysis of the Valsamiotis Dam

3.1 Datasets

On this chapter the DInSAR approach, discussed in the previous chapter, is applied to a data set of Sentinel -1A and -1B images. The small-time acquisition difference was exploited to select data images that overall will be of high coherence between each other. The time difference between each data image was selected to be close to 30-35 days; as can be seen in table 3.1, for October 2017 two data images were selected due to a heavy rainfall event that took place between the times of the acquisition. The final data-set consists of 20 Sentinel-1A/1B SAR images of ascending orbit that were used to generate 42 interferograms through the period between June 2017 and December 2018. The images belong to the same acquisition subset and the SBAS methodology, explained in the previous chapter, allowed the exploitation of the temporal and perpendicular baselines for the generation of the deformation time-series. The reference point was selected in the area near Agia Lake. The selection was based after conducting calculations on more than twenty points in the Keritis basin and comparing (i) the results and (ii) coherence.
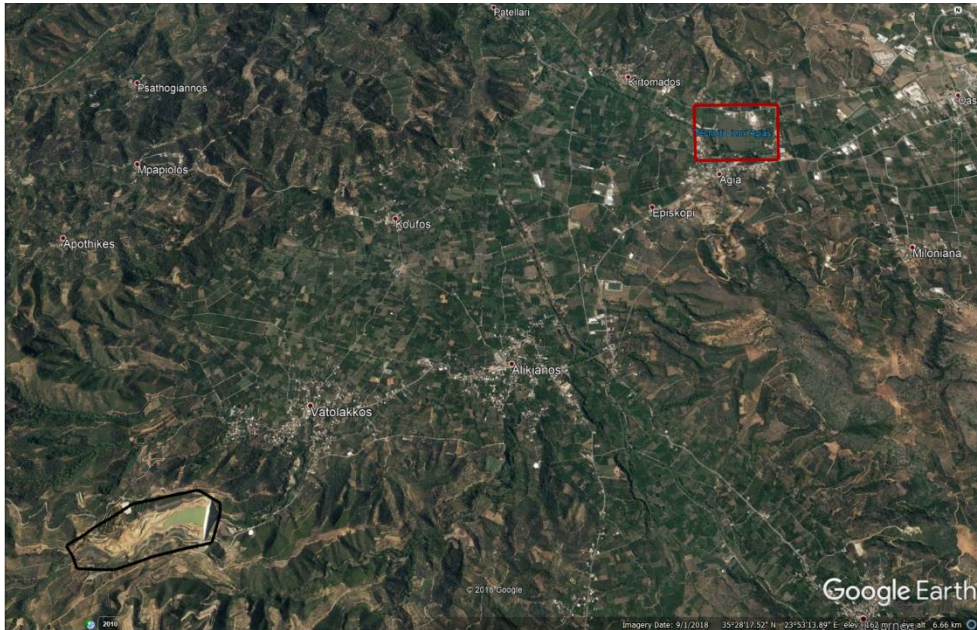
Figure 32. Valsamiotis Dam (black polygon) and Agia Lake (red rectangle).

Table 3.1, Sentinel data set used in the context of the thesis. The perpendicular and the temporal baseline differences were calculated in respect to the first acquisition.

Sentinel Mission	Orbit Nº	Perpendicular Baseline (m)	Day	Month	Year	Temporal Baseline (days)
S1A	16974	0	10	6	2017	0
S1B	6428	30.2	10	7	2017	30
S1A	17849	27.4	9	8	2017	60
S1A	18374	-79.46	14	9	2017	96
S1A	18724	-12.86	8	10	2017	120
S1B	8003	45.16	26	10	2017	138
S1B	8353	-81.96	19	11	2017	162
S1A	19774	39.31	19	12	2017	192

S1B	9228	89.84	18	1	2018	222
S1A	20649	10.05	17	2	2018	252
S1A	20999	33.79	13	3	2018	276
S1A	21524	39.6	18	4	2018	312
S1B	10978	18.9	18	5	2018	342
S1A	22399	14.89	17	6	2018	372
S1B	11853	26.24	17	7	2018	402
S1A	23274	-48.43	16	8	2018	432
S1B	12728	-45.79	15	9	2018	462
S1B	13253	-17.03	21	10	2018	498
S1A	24674	63.07	20	11	2018	528
S1A	25199	-34.23	26	12	2018	564

Table 3.2, Showcase on the Baseline differences in both spatial and temporal axis of the interferograms. Sentinel-1 interferograms consist of small spatial baseline differences (even when the temporal difference is large).

Interferometer	Perpendicular Baseline (m)	Temporal Baseline (days)
June-July 2017	30.82	-30
June - August 2017	28.12	-60
June - October 2017	-13.21	-120
July - September 2017	-112.22	-66
July - October 2017	-116.05	-108
August - October 2017	-37.8	-60

August - November 2017	17.41	-102
September - October 2017	-5.12	-42
September - December 2017	170.13	-96
October - November 2017	51.45	-42
October 2017 - January 2018	45.51	-102
October – December2017	173.65	-54
October 2017- February 2018	89.04	-114
November 2017 – December 2018	46.46	-30
November 2017 – January 2018	-6.24	-60
November 2017 – March 2018	-11.78	-114
December 2017- February 2018	-84.88	-60
December 2017 – April 2018	-50.14	-120
January – February 2018	-32.48	-30
January – March 2018	-5.86	-54
January – May 2018	-19.98	-120
February – April 2018	34.79	-60
February – June 2018	7.78	-120
March 2018 – December 2017	58.19	84
March – May 2018	-14.26	-66
March – July 2018	-7.78	-126
April – August 2018	-87.69	-120
May -July 2018	7.02	-60
May – September 2018	-62.86	-120
June- August 2018	-60.81	-60
June – October 2018	-27.07	-126
July – September 2018	-69.39	-60
July – November 2018	37.47	-126

August – October 2018	33.89	-66
August – November 2018	109.35	-96
August – December 2018	15.02	-132
September – November 2018	106.81	-66
October – September 2018	-31.34	36
October - December 2018	-20.11	-66
November – October 2018	-75.47	30
December – September 2018	-13.16	102
December – November 2018	95.03	36

3.2 Interferogram generation

As stated before, an interferogram is generated between a data-pair of two images; the master image and the slave image. The selection of the optimal data-pairs for the region of interest (ROI) was obtained with the help of the Delaunay-triangulation on the Temporal-Perpendicular baseline plane. In order to generate this triangulation, we define a ratio between the perpendicular and temporal baseline units. The ratio we imposed on our analysis is equal to $\delta T/\delta b_\perp$, representing the maximum allowed temporal and spatial baselines respectively. Both limits are introduced to avoid the generation of strongly corrupted by decorrelation phenomena interferograms. The temporal limit was set to 500 days and the perpendicular baseline was set to 500m. Note that, in the spatial area the limit is not of critical issue since the baseline of Sentinel-1 images have already small differences. Each arc connects two different points that identify the corresponding DInSAR data-pair and as such, with the help of the triangulation we can generate the sequence of identified interferograms.
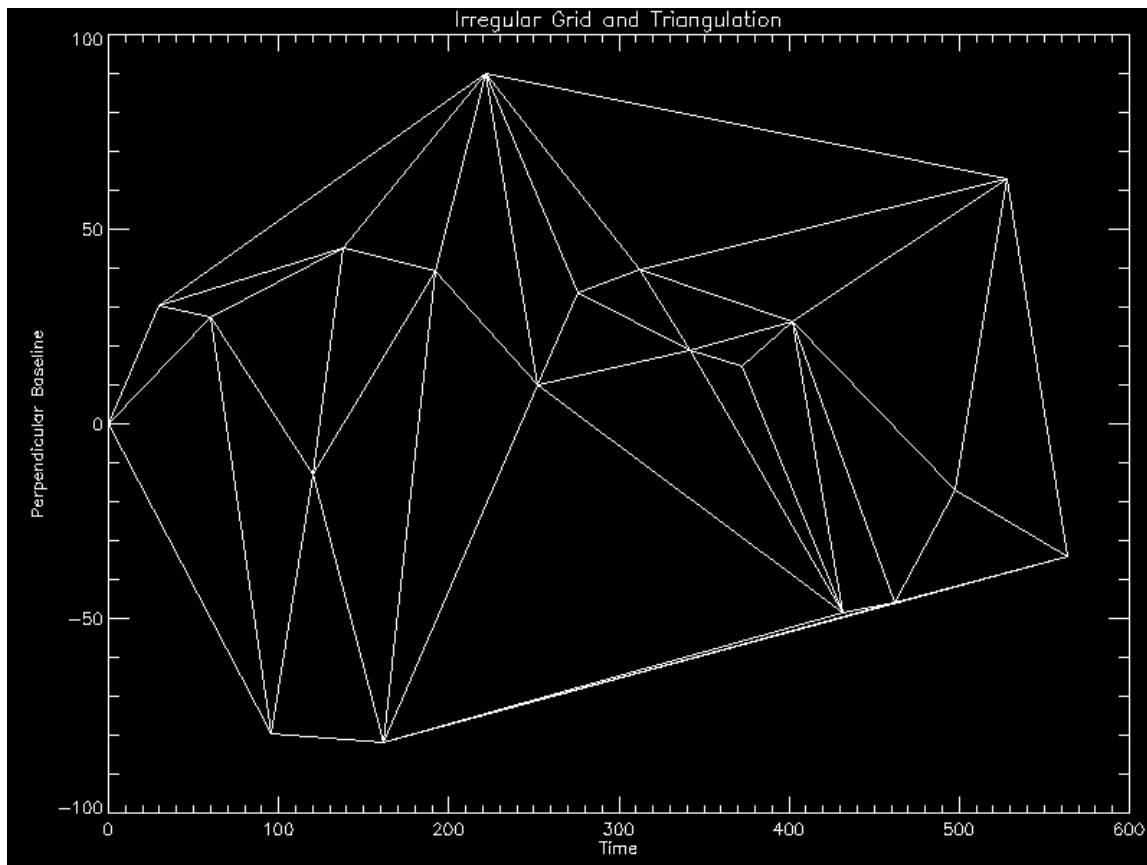
Figure 33, Delaunay Triangulation in the temporal/spatial plane.

Before proceeding to the interferogram generation, it is good to acknowledge the metadata coefficients that are useful in the calculation that are presented below. A SAR image metadata contains useful information regarding:

- Incidence angle; angle between the radar beam and the normal to the local topography,
- Look angle; angle between the direction the antenna is pointing and the nadir,
- Wavelength; Sentinel-1 wavelength is 5.55 cm,
- Spatial resolution of the radar system and
- Bandwidth

As can be seen in fig. 34, the data that we obtain from ESA contain the real (Re) part and the imaginary (Im) part of the image. Both of those parts contain useful information about the amplitude, a, and the phase, φ, of the image.

$$\varphi = arctan\frac{Im}{Re}$$
$$a = \sqrt{Im^2 + Re^2}$$

(115)
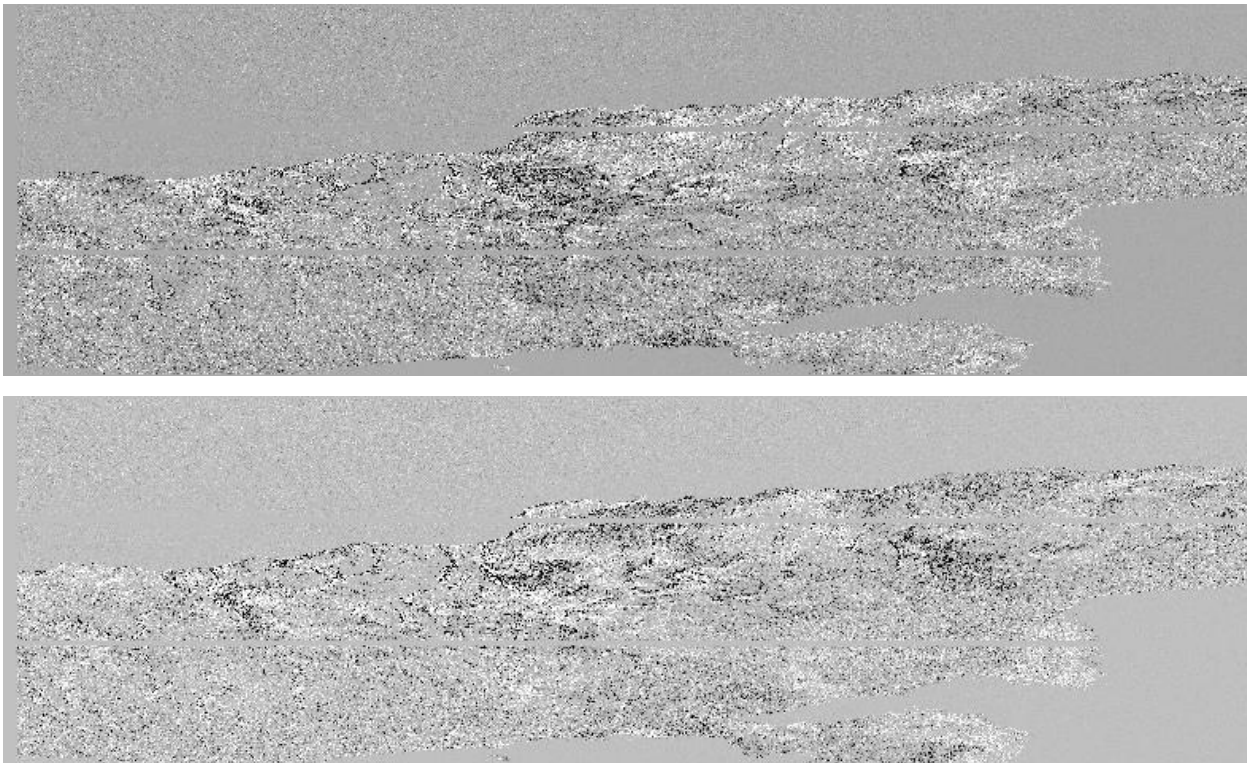
Figure 34. Real part (top) and Imaginary part (bottom) of an interferogram.

Combining the phase information of two complex radar images, we calculate the phase of the interferogram where the fringes that occur, represent the whole range of the phase from [-π, π[.
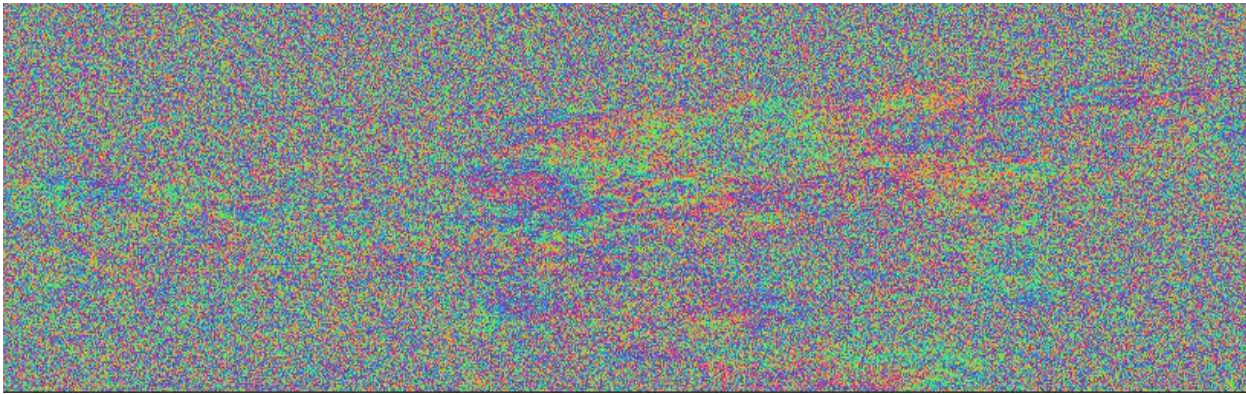
Figure 35, Phase Image of an interferogram of western Crete.

3.3 Coherence calculation

To calculate the coherence between the images that form the interferogram we correlate their phase values. The value of coherence ranges from 0 (low coherence-high decorrelation) to 1 (high coherence). The decorrelation that is present in the images is due to thermal noise, geometry changes that affect the baseline or temporal changes.

It is useful at this point to present the coherence scatter plot of the generated interferograms that were used in this thesis.
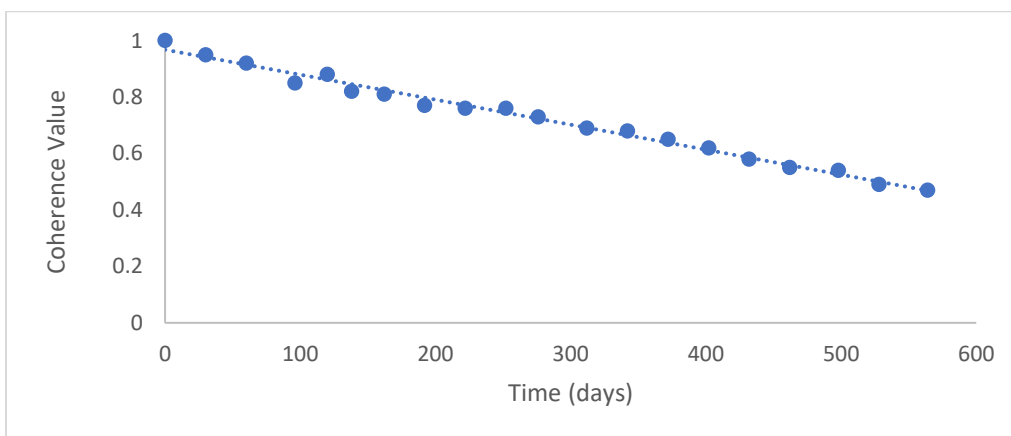
Figure 36. Plot of calculated Coherence value versus time of acquisition, single master image co-registration.
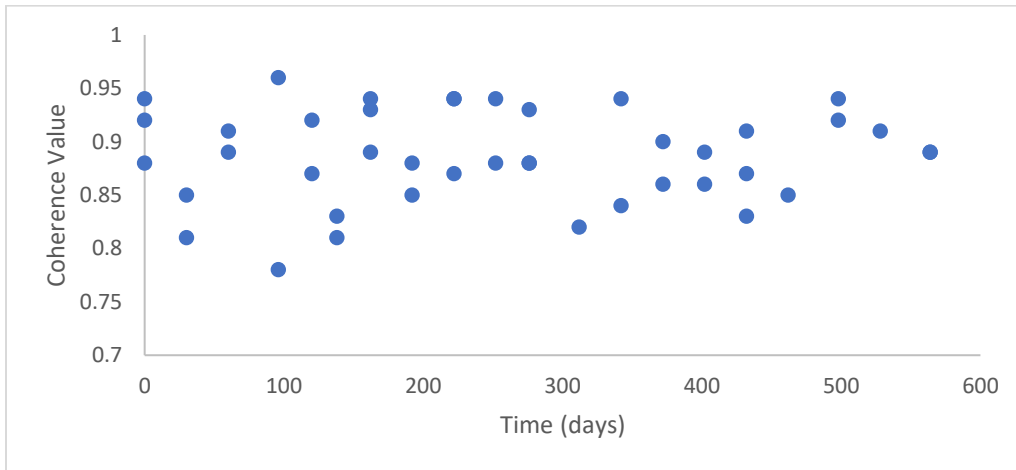
Figure 37. Scatter plot of calculated Coherence value versus time of acquisition of respective master image (different master on each master-slave pair).

In Figures 36 and 37, the coherence values of the co-registered images, with single master image and multiple master image strategy methods respectively, are presented. In the single master image, the coherence values have a declining trend (from 0.95 to 0.47); the trend is affected by the difference between the time of acquisitions of the master and slave image. In the multiple master strategy, the coherence values of all the interferograms are in the same range (between 0.94 and 0.78). For the single master image co-registration, the average coherence value is 0.676 while in the multiple master strategy the average coherence value is 0.866. Using the Delaunay triangulation in choosing the optimal master-slave pairs results in more coherence heavy interferograms.

Achieving high coherence values in the interferogram pairs is overall useful in calculating ground deformation. In our case high coherence is needed, as the area of interest consists of numerous hills and vegetation areas that in addition with the micro-climate of the region, can affect the coherence values in the time-span we are using. For this reason, the SBAS technique was deemed necessary as the generated interferograms retain a higher coherence value (0.866 average value) than the single-master method (0.676 average value).

3.4 Unwrapping Phase Images

For the purpose of this thesis, we generated 42 differential interferograms. As stated in the previous Chapter the D-InSAR phase images are constrained in the [-π, π[region and therefore we applied the MCF unwrapping procedure to reconstruct the full phase image in the integer-2π phase jumps. Presented below are selected wrapped and unwrapped phase image for each acquisition date.

In Figure 38, we can see some of the wrapped interferograms that were used in the generation of the deformation time-series. The color bar of the figure, is representing the [-π,π[range of the wrapped phase of the images. The different coloring between the images is the result of the two following main reason. First reason is the difference of acquisition times between the master-slave data pair that formed the interferogram. The second reason is the difference of the perpendicular baselines of the data-pair.
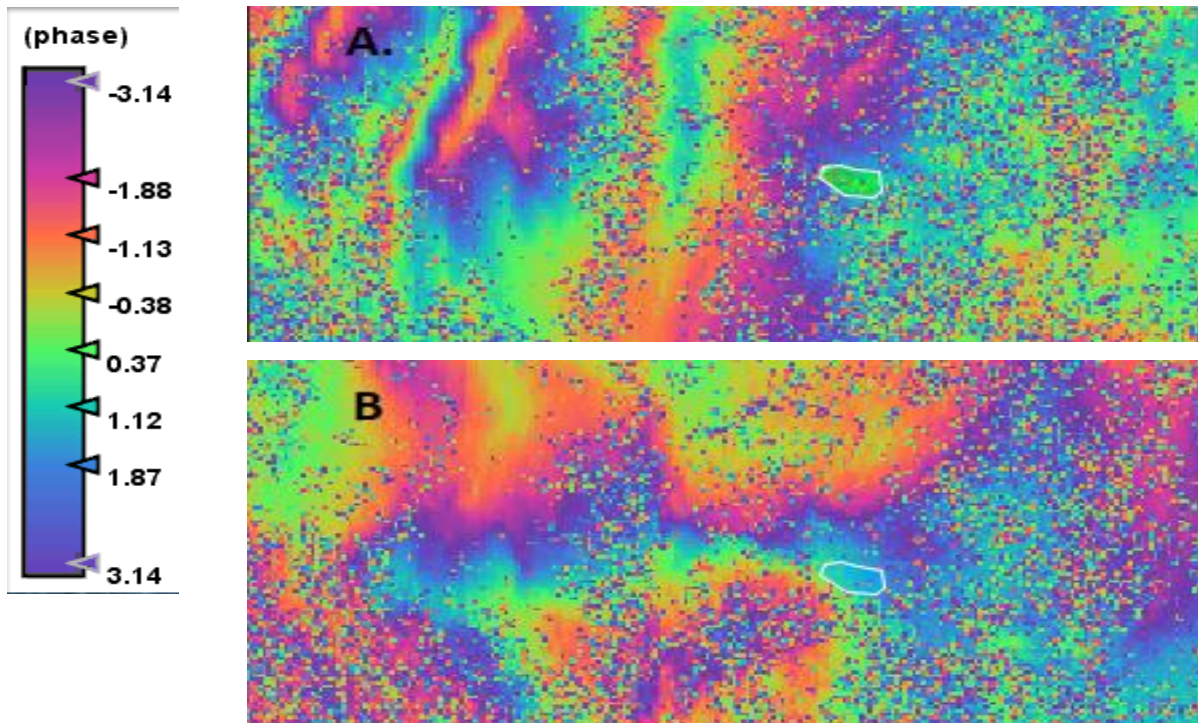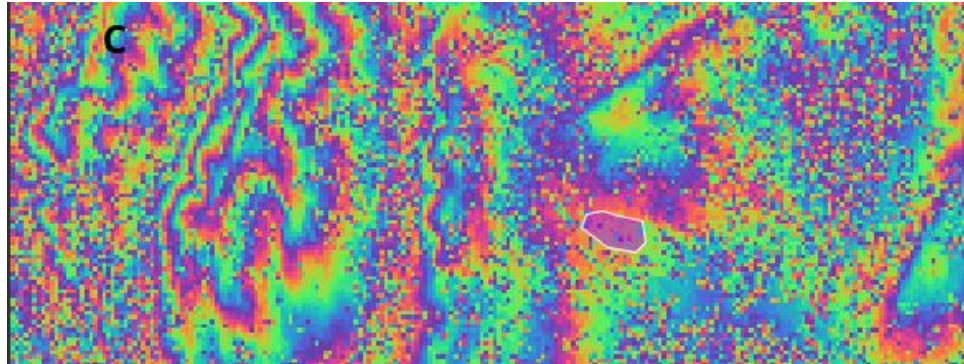
Figure 38. Wrapped phase Interferograms of Keritis Basin. The dates that were used for the 3 wrapped interferograms are: **A.** 10 June 2017 and 9 August 2017, **B.** 19 November 2017 and 18 January 2018, **C.** 18 May 2018 and 15 September 2018. In all the three images the area where the dam is located shows no elevation change (no change in the fringe pattern).
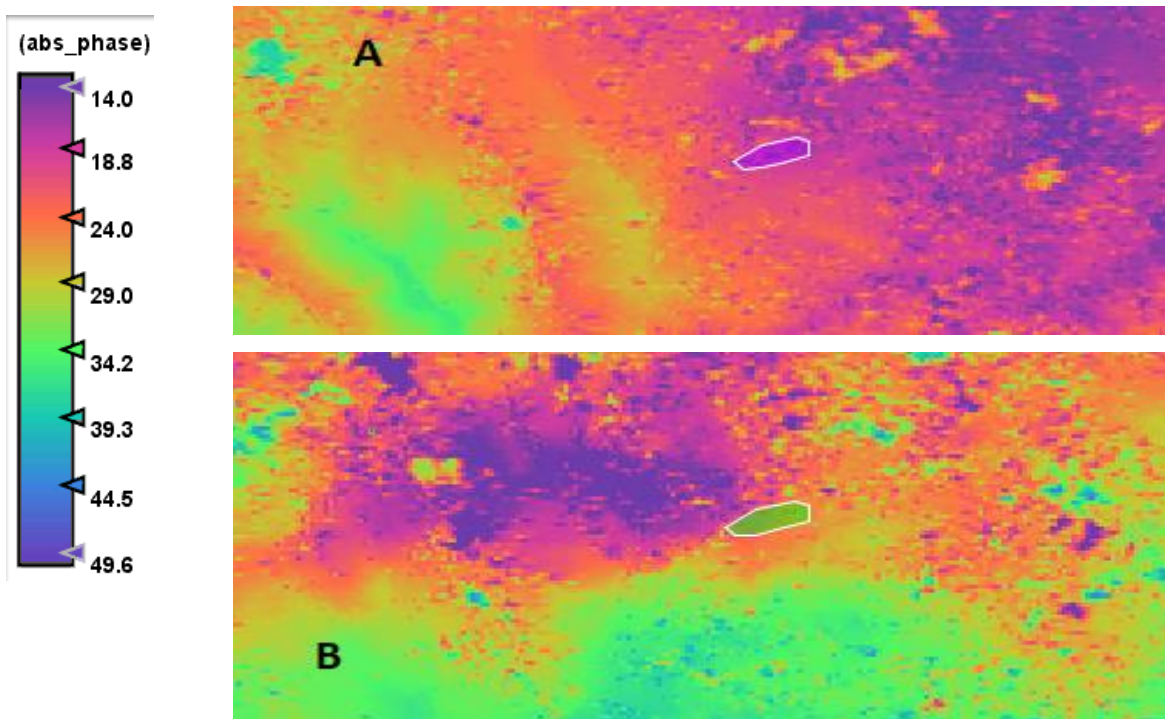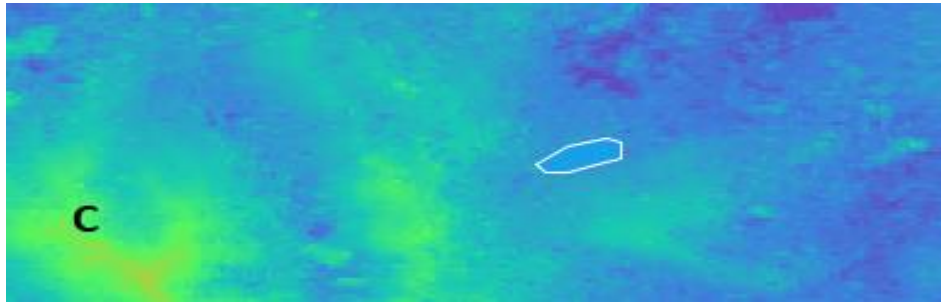
Figure 39. Unwrapped phase images of Figure 38 interferograms. As in the wrapped images, the area where the dam is located shows no elevation change (coloring remains the same).

In Figure 39, the differences in the patterns are more visible. Images A and B are affected by the small perpendicular baselines that Sentinel-1A/1B have. In the unwrapped interferograms from data-pairs with small perpendicular baselines difference, we have the appearance of irregular shapes of different color pattern (resembling patches). In unwrapped interferograms that have larger perpendicular baselines difference the color pattern is smoother in appearance. In the unwrapped interferogram of image A the perpendicular baseline is 28.12m, of image B is 6.22m and of image C is 87.69m. It must be noted that in both the wrapped and unwrapped images the area of the dam is uniformed with no change in the fringe patter (wrapped) or color pattern (unwrapped) which means that the elevation does not change. Due to the non-change in the elevation, the small perpendicular baseline differences do not affect directly the area and so all the images were considered useful and were kept for the time-series generation and the deformation calculation.

Chapter 4

Experimental Results

4.1 Time Series and Dam water Data

The SAR data-set was composed by 20 Sentinel -1A and -1B acquisitions between June 2017 to December 2018. After applying the MCF unwrapping procedure, the SBAS processing technique described in Chapter 2 was applied to the data-set. In Figure 40, the area of interest is presented and is followed by the time-series before and after the atmospheric correction procedure on Valsamiotis' Dam and its broadened area.
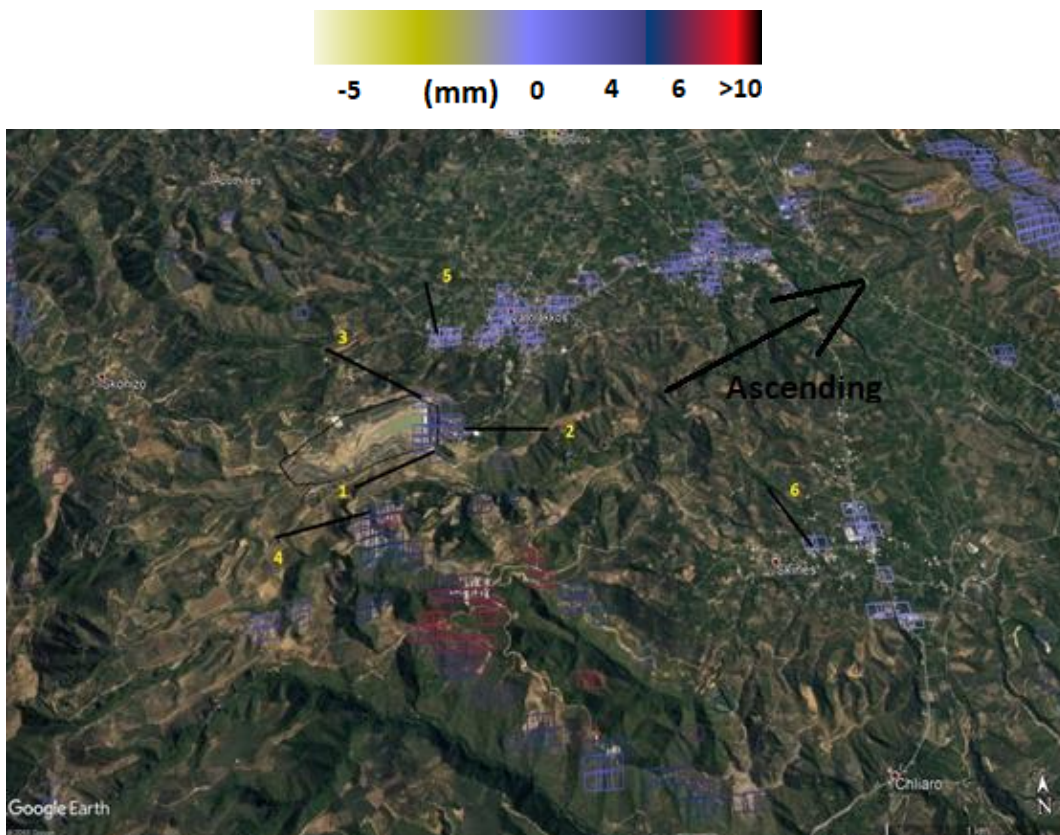
Figure 40. Valsamiotis dam and its broadened area.

1

2

3
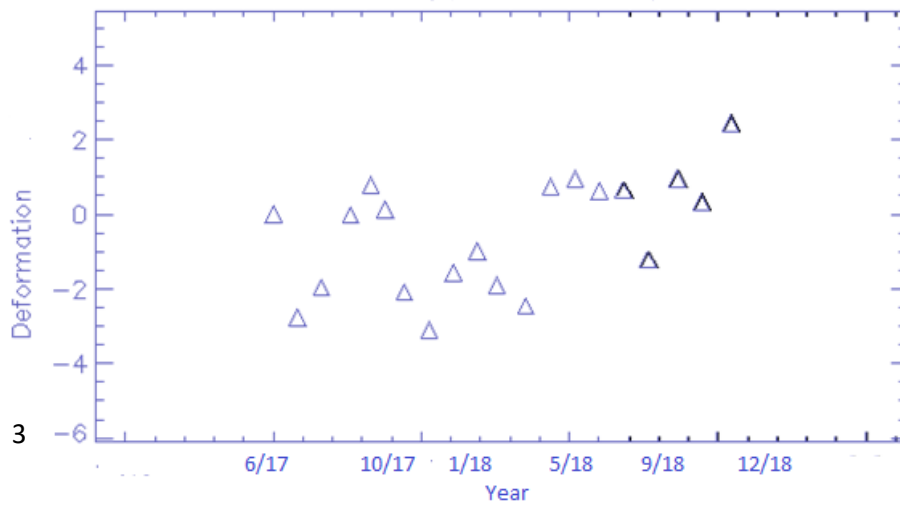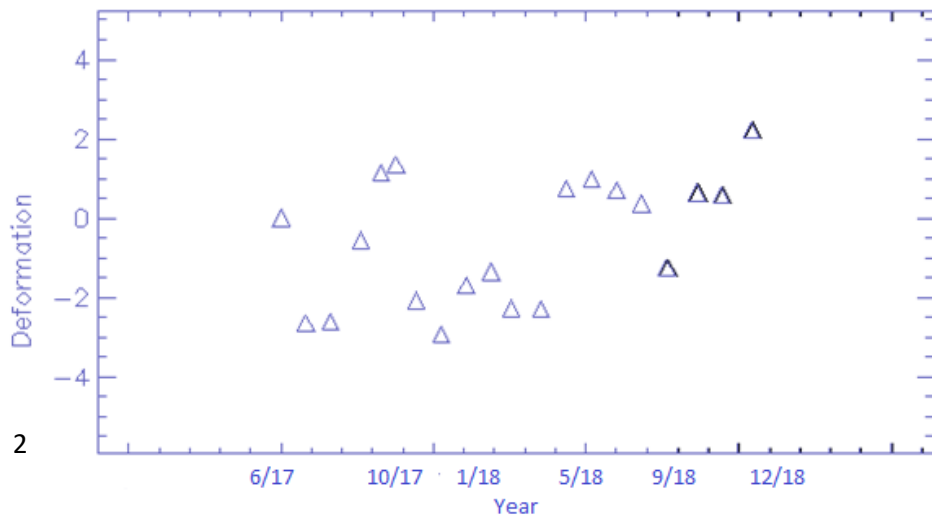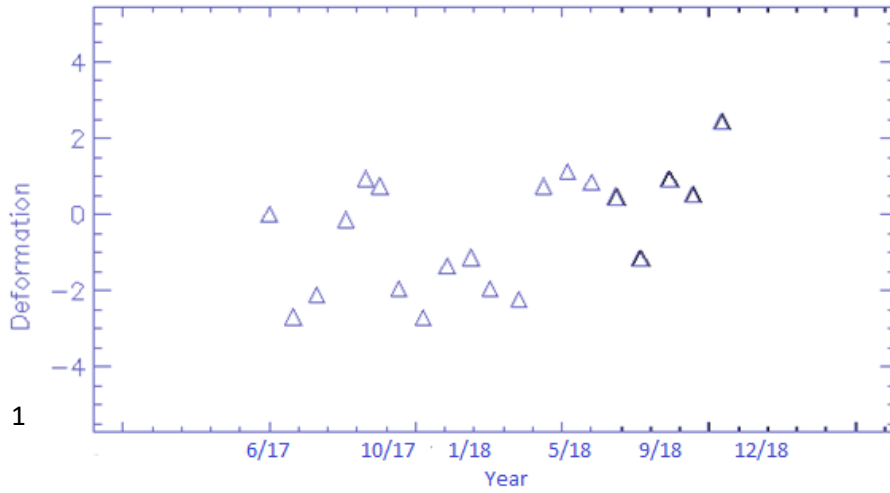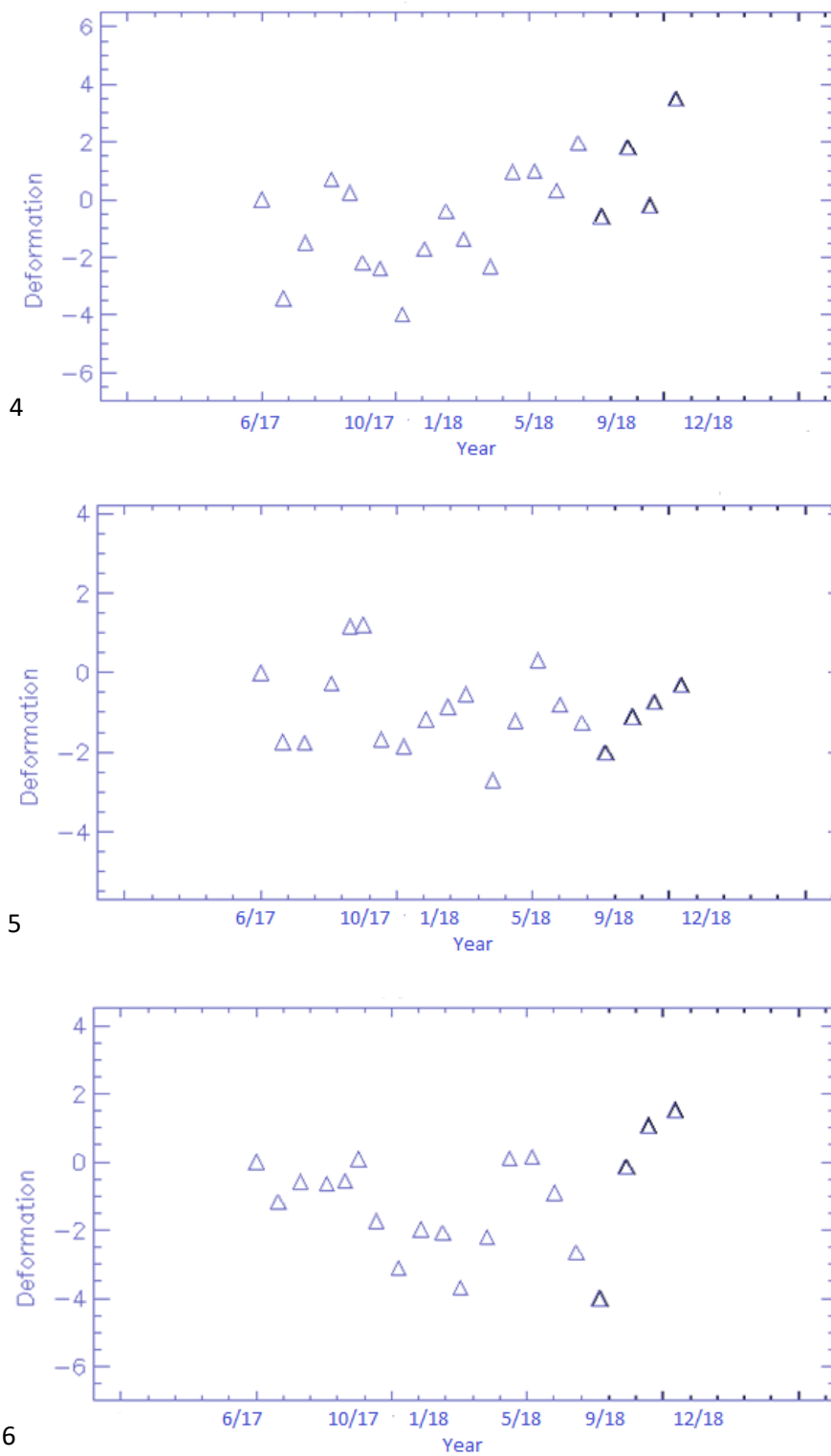
Figure 41. Unfiltered deformation (cm) time-series.1, 2, 3, Valsamiotis dam, 4. South Hill area of the dam.

5. Village of Vatolakos. 6. Village of Skines.

The region of interest is located in a mountainous area with heavy vegetation meaning that the global numerical models cannot predict the micro-climate [69]. Since the Sentinel-1A/1B SAR system is emitting C-band microwaves, the acquisitions are heavily affected by the atmospheric noise that needs to be removed. The atmospheric contribution is a result of atmospheric humidity (due to the atmospheric layers) and atmospheric pressure which delays the movement of microwave signals and echoes. Except from the atmospheric humidity, the sea humidity must be taken into account. Depending on the season, the weather conditions and the vegetation the humidity factor can be quite high.

The atmospheric filtering operation is performed in both spatial and temporal baseline axis. The values used for the filtering operation were picked in regard to the minimum timespan of the data-set time-acquisitions and in the spatial department the values used was in regard to the number of nearby pixels. The filtered time-series can be seen in the following Figures and for the three selected points in the dam the correlation with the water level and volume change is presented also.
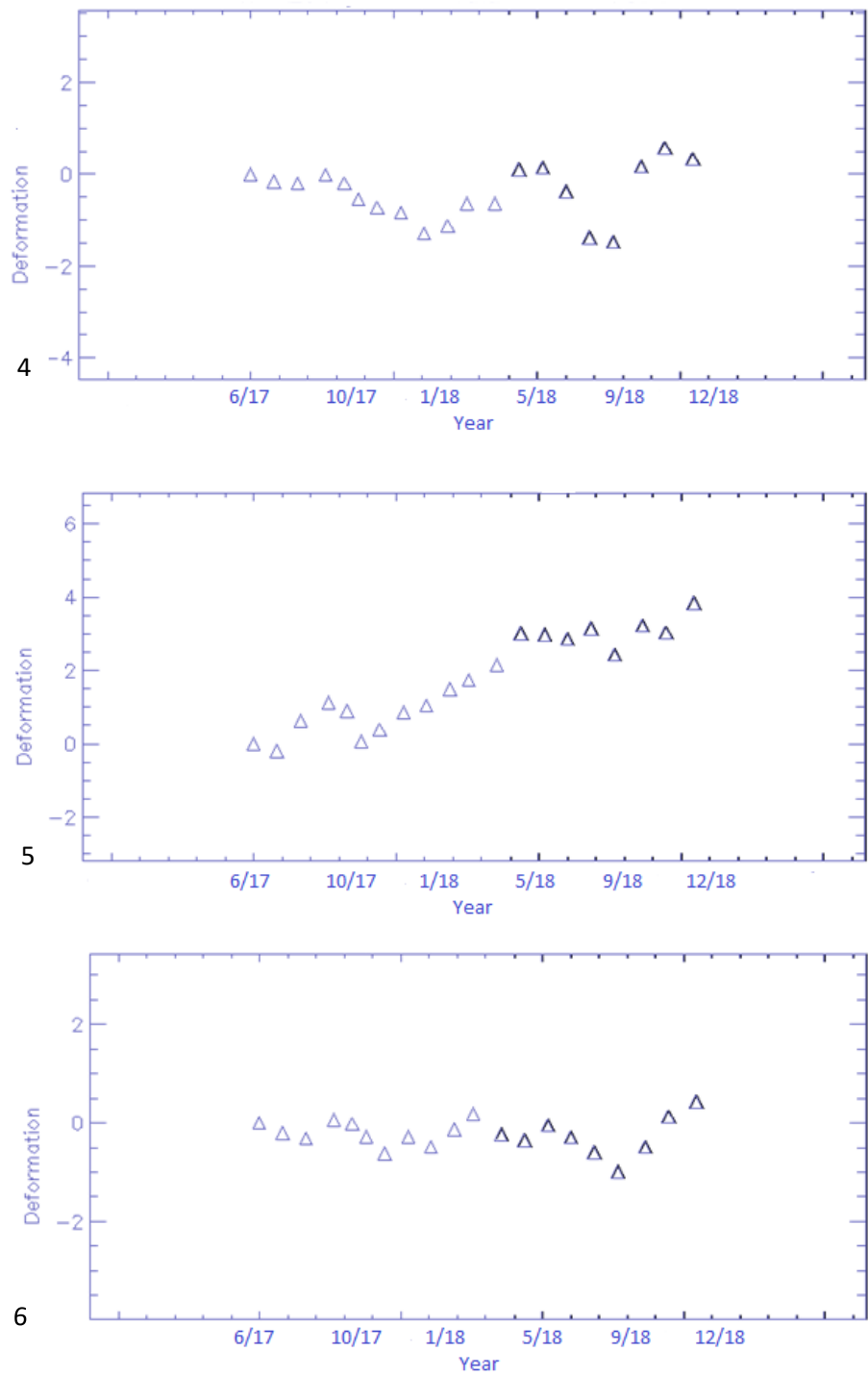
Figure 42. Filtered Deformation (cm) Time-Series for: 4. South Hill area of the dam. 5. Village of Vatolakos. 6. Village of Skines.
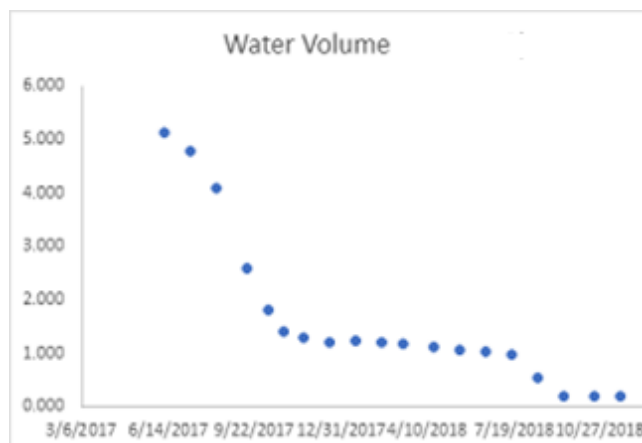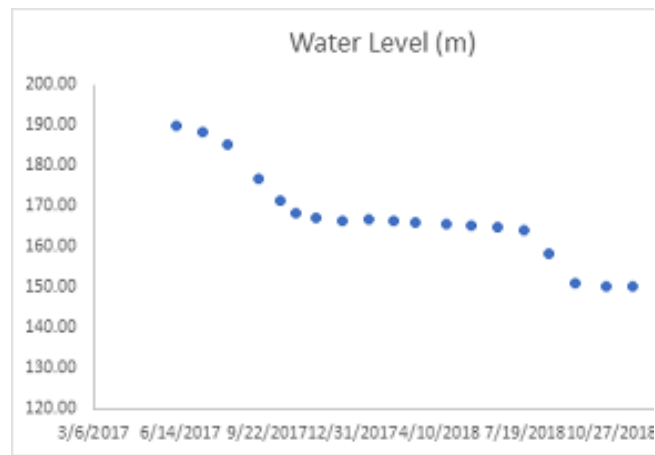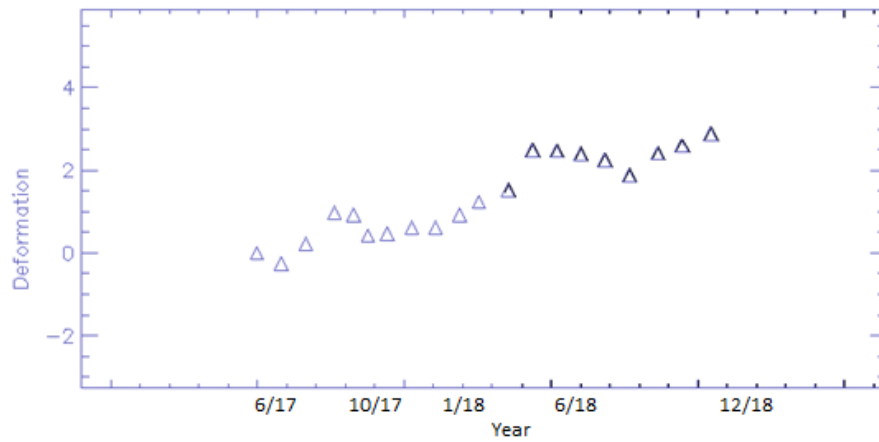
Figure 43. Up: Deformation (cm) time-series of point 1 in the dam. Middle: Water Level and Bottom: Water Volume (x10^6 m^3).
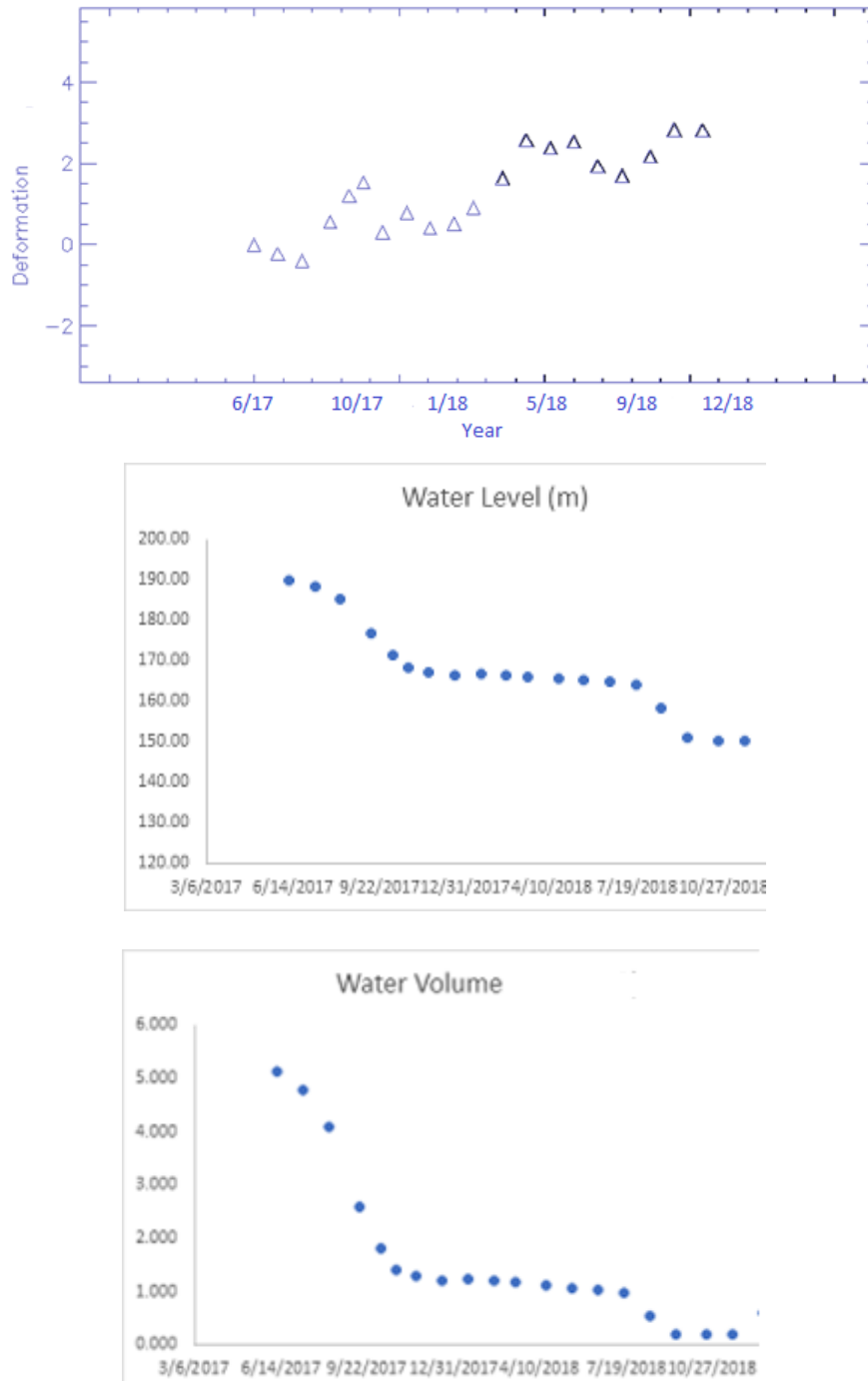
Figure 44. Up: Deformation (cm) time-series of point 2 in the dam. Middle: Water Level and Bottom: Water Volume ($\times 10^6$ m³).
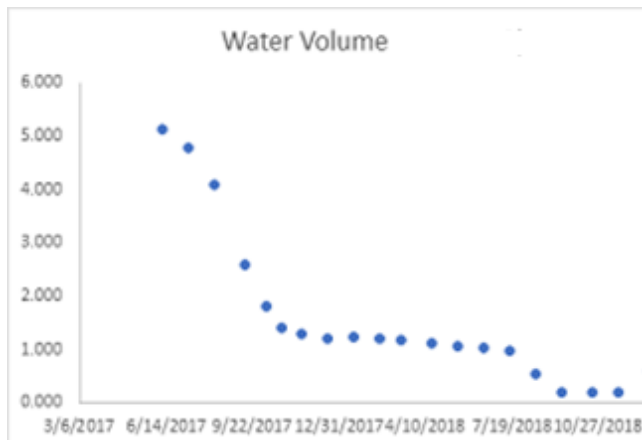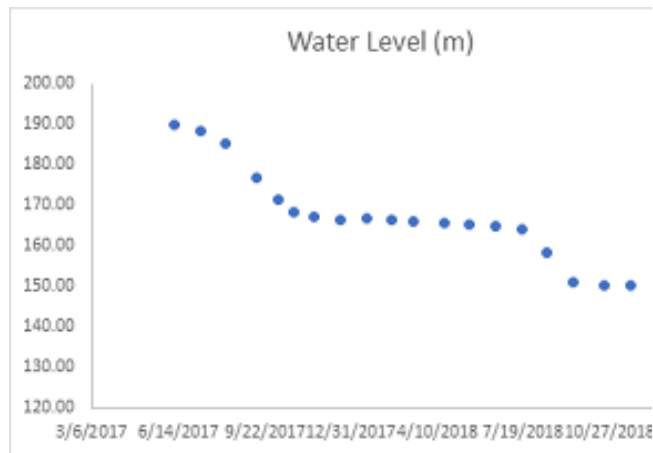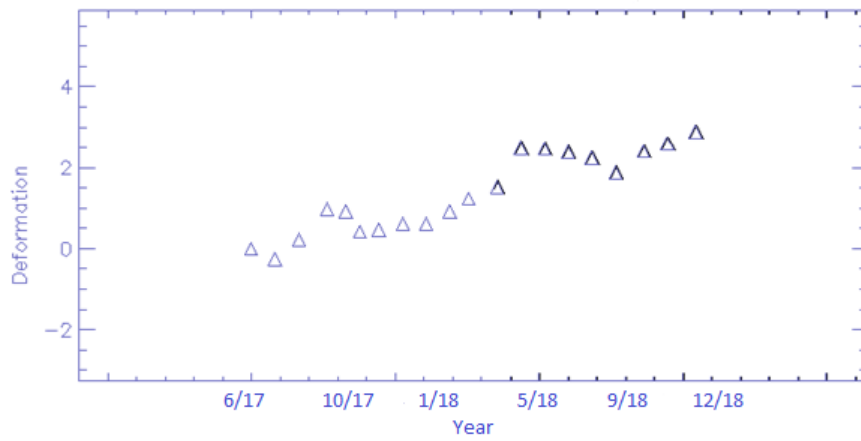
Figure 45. Up: Deformation (cm) time-series of point 3 in the dam. Middle: Water Level and Bottom: Water Volume ($\times 10^6$ m³).

4.2 Data Correlation

In water reservoirs, the intra-annual water level changes cause an elastic instantaneous response of the Earth. This response may lead to surface deformations, that are dependable on the lithology and sediment thickness. Consequently, we measured the ground deformations of Valsamiotis region by using the deformation time series of Sentinel-1 data (figure 43) for the time period 2017–2018, in which the net water level decreased by approximately 40m. We expect that these load changes on the ground lead to an uplift of the broadened area in our case where the water recessed [69].

All three mean deformation time-series (figures 44-46), in the spatial domain, reveal a LOS deformation in the east dam area. During the investigated time period, the water level and volume decreased and the reverse behavior of uplift is monitored. For point 1, the LOS deformation mean velocity is in the order of 11.60 mm/yr, for point 2 is in the order of 11.71 mm/yr and for point 3, 11.53 mm/yr.
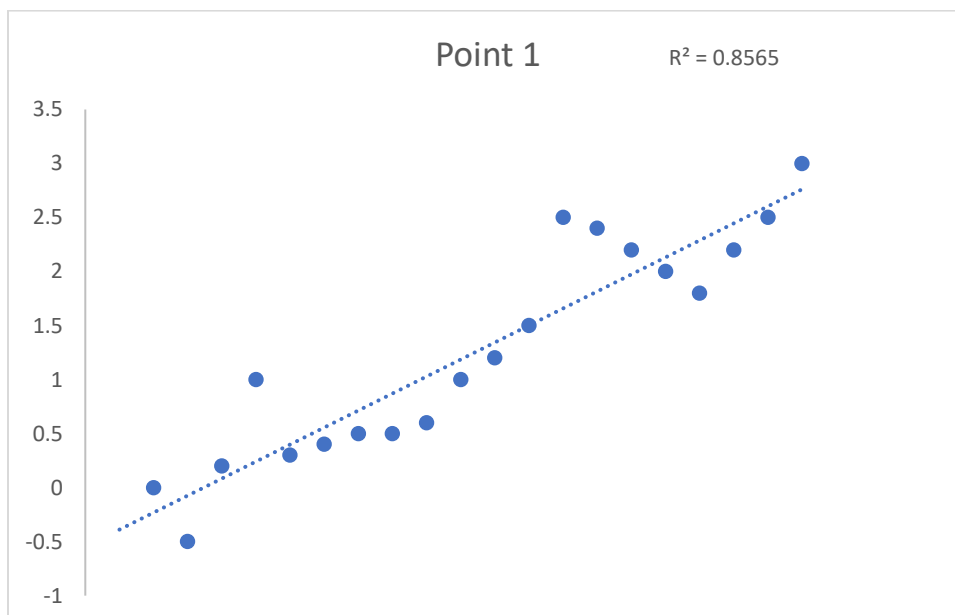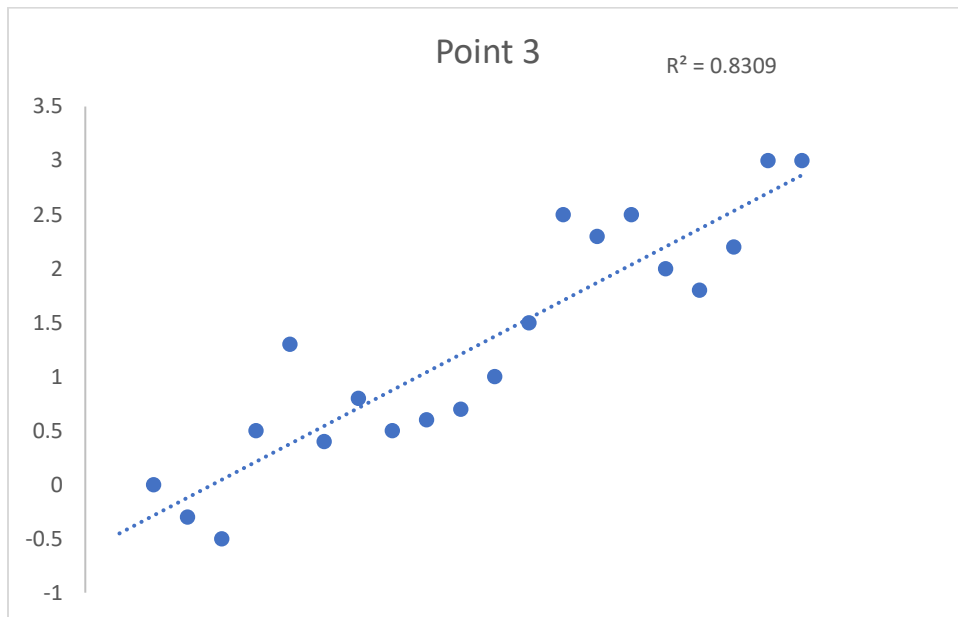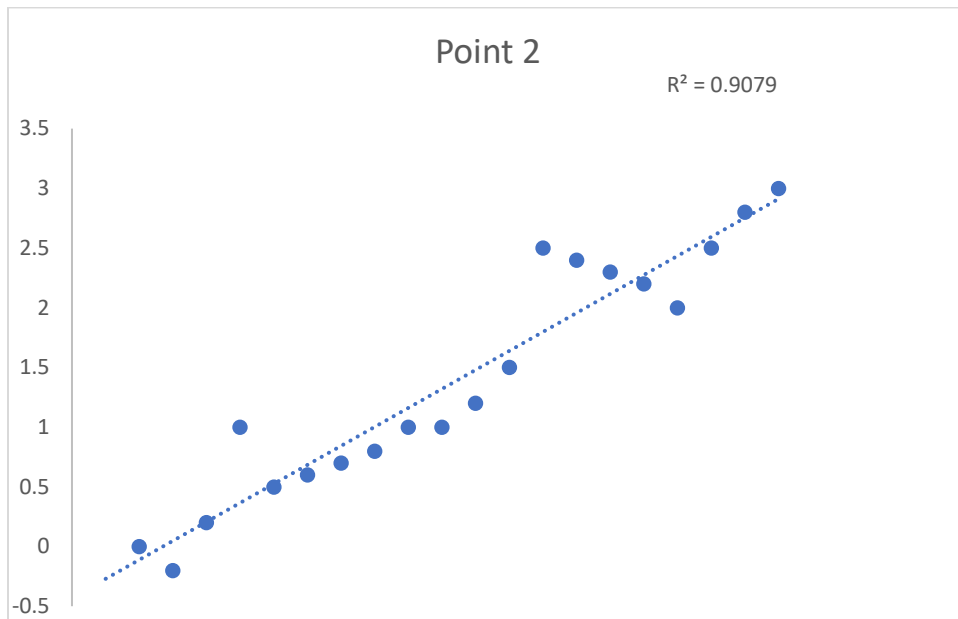
Figure 46. LOS deformation behavior of points 1, 2 and 3 with the decrease in the water level.

Between LOS deformation and water level the correlation in general is high (figure 47), with point 2 (R^2=0.9079) having the highest correlation from point 1 (R^2=0.8565) and point 3 (R^2=0.8309). From figure 47, we can observe that the deformation appears simultaneously with the changes in the water level, which is an indication of the surface elastic response.

Chapter 5

Discussion

In this chapter the experimental products of the SAR data-sets, that were carried out by the procedure shown in the previous chapter, are discussed. We have measured the deformation velocity in the Valsamiotis dam using Sentinel-1 SAR imagery. The study area is located in mountain-terrain with vegetation and thus, the acquisitions are severely affected by atmospheric noises that were removed in the deformation analysis. Although the time-period of the acquisitions is relatively small (2017-2018, figure 47), the results shows a strong correlation (R^2 between 0.8309 and 0.9079) with the decrease in water level and the uplift of the dam region. The eastern area of the dam shows a deformation rate of 11.6 mm/yr and measurable deformation was found north of the dam (deformation rate 15 mm/yr, table 5.1).

The reason of the differences in the water level trend and water volume pattern can be explained by observing the images in Figure 47. Water level changes are measured in the Dam structure while water volume changes are measured for the entirety of the dam. Despite that the three points were selected near the dam structure, the deformation time series for these points show a correlation with both water level and volume changes.

Although the dam area is in a seismically active area, in the investigated time-period no major earthquake occurred and so the measured mean deformation is not affected by tectonic events. Furthermore, the analysis of deformation – water level correlation, revealed that ground deformation occurred simultaneously with the water reservoir changes, which indicates that there is no major interference due to atmospheric factors in the final results.

Table 5.1. Mean deformation Velocity in mm/yr in regard to the reference point.

	Dam point 1	Dam point 2	Dam point 3	Vatolakos	Skines	South Hill Area
mm/yr	11.69	11.53	11.71	15.07	0.16	0.16

The data in table 6.1 shows the relative shift of the six points that were selected in the dam and in the broadened area of the dam, in regard to the reference point. Between the dam points (1,2 and 3) there is no relative shift between them. In regards to Vatolakos village, all three selected dam points shift away by 3.38 mm/yr, 3.36 mm/yr and 3.54 mm/yr respectively. In regards to Skines village, the three dam points shift towards by 11.53 mm/yr, 11.55 mm/yr and 11.37 mm/yr. In regards to the south hill area, dam point 1 shifts towards it by 11.53 mm/yr, point 2 by 11.55 mm/yr and point 3 by 11.37 mm/yr. The relative positive and negative shifts between the adjacent dam points may indicate a barrier in the groundwater system, such as permeability contrast or an unmapped fault (figure 47) [70].

The steep slopes, consequence of the mountainous areas near the dam, alongside with the vegetation of the area, were detrimental in selecting points near the west and north side of the dam. The coherence values for these areas were lower than 0.2 and were not used in the time-series. One possible solution to increase the coherence values in those areas would be to use both ascending and descending orbits coupled with X-band SAR data. Using ascending and descending orbits will help in calculating the west-east and vertical displacements and the X-band SAR data will be of help to further increase the coherence in the images. Apart from the SAR data specifics, it will be useful to investigate the area installing GPS stations in the area of the dam. Knowing the reference's point deformation and characteristics will be useful in avoiding errors in topography calculation and more

accurate DEM maps that will be helpful in avoiding mis-registrations when using the co-registration process and the topography phase removal operation.
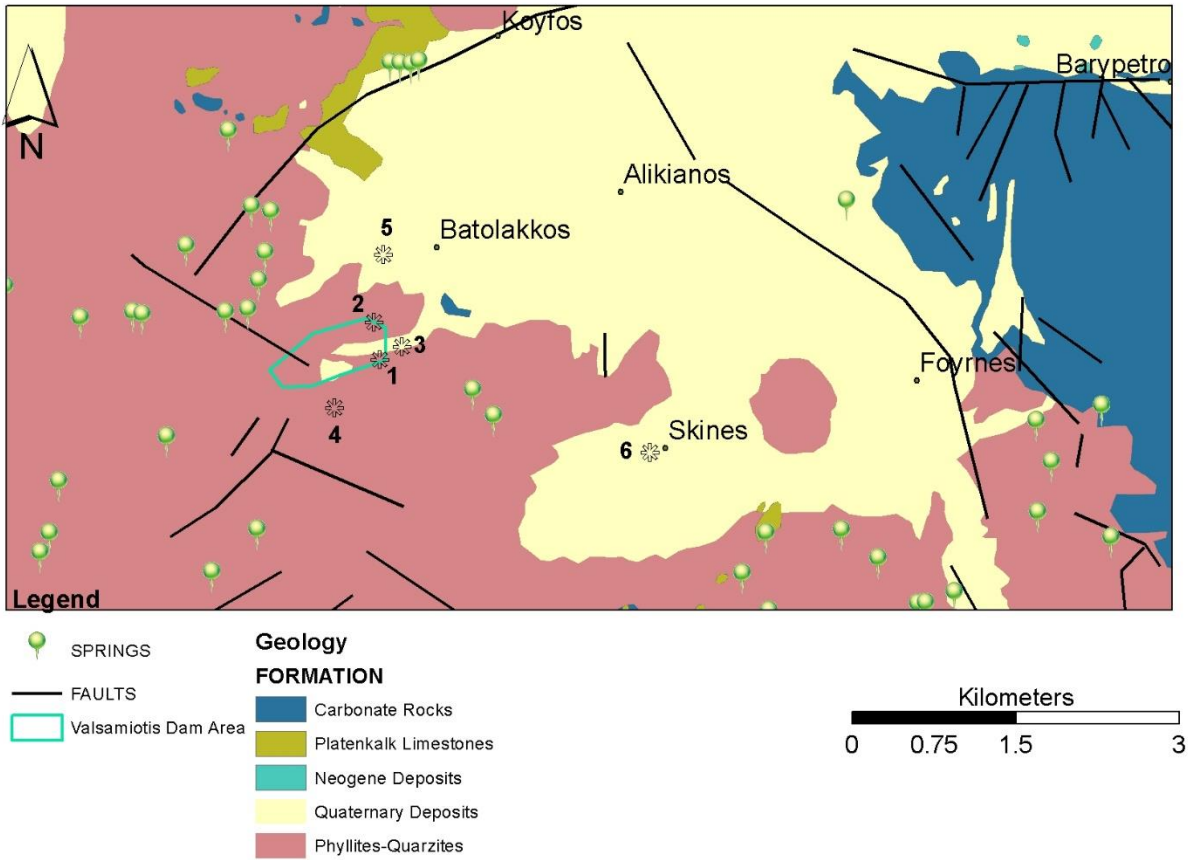
Figure 47. Geology formations of Valsamiotis dam broadened area. Point 3 is at the edge of phyllites-quartzites formation and the quaternary deposits, which indicates permeability contrast.

Figure 47. Top image: Dam on June 2017, Bottom image: Dam on September 2018 (Source: Google Earth)

Future Research

There are several avenues for future research in the study area and other areas in Greece with water reservoirs using SAR data from Sentinel-1 and/or from other SAR satellites such as Cosmos-SKYMED, TerraSAR-X, KOMPSAT-5. It is important to use extended time-periods to assess the identified deformation due to the annual water changes (i) for rural areas near the dam and investigate the potential consequences of the measured deformation, (ii) in combination with changes in other nearby water reservoirs, (iii) with continuous monitoring of the nearby mountain slopes, will help with early detection of instabilities that may lead to slope failures and collapse into the lake.

Further investigation is needed in the Crete region as well as other active tectonic areas of Greece and investigate the deformation pattern that is formed due to tectonic and/or geologic events. Apart from the Sentinel-1A/1B satellites it will prove useful to acquire X-band SAR images. Expansion in the data-set acquisition timeline to a minimum of five years, will help to distinguish patterns in the deformation time-series and the correlation with seismic and/or geologic events. Investigating the deformation patterns in tectonic areas of Greece will be beneficial in the understanding of the seismic activity of the Hellenic Arc zone and potential hazardous situations. Additionally, it would be useful for areas with micro-climates (e.g. Valsamiotis dam) to generate atmospheric models through machine-learning algorithms. This would allow atmospheric corrections through the DInSAR processing chain to be more accurate and as such, improve the quality in the generation of the deformation time-series.

References

1. P. M. Soupios, M. Kouli, F. Vallianatos, A. Vafidis, G. Stavroulakis "*Estimation of aquifer hydraulic parameters from surficial geophysical methods: A case study of Keritis Basin in Chania (Crete – Greece)*", Journal of Hydrology, vol. 338, pp. 122-131, 2007.

2. J. Angelier, "*Determination of the mean principal directions of stresses for a given fault population*", Tectonophysics, 56, T17-T26, 1979.

3. P. Huchon, N. Lyberis, J. Angelier, X. Le Pichon, V. Renard, "*Tectonics of the hellenic trench: A synthesis of sea-beam and submersible observations*", Tectonophysics, 86, 69-112, 1982.

4. S. C. Stiros, "*Identification of Earthquakes from Archaeological Data: Methodology, Criteria and Limitations*", Archaeoseismology, 1996.

5. B. Shaw, N. N. Ambraseys, P. C. England, M. A. Floyd, G. J. Gorman, T. F. G. Higham, J. A. Jackson, J-M. Nocquet, C. C. Pain, M. D. Piggot, "*Eastern Mediterranean tectonics and tsunami hazard inferred from the AD 365 earthquake*", Nature Geoscience 1, 268-276, 2008.

6. D. W. Simpson, W. Leith, C. Scholz, "*Two types of reservoir-induced seismicity*", Bull. Seismol. Soc. Am., vol 78, pp. 2025-2040, 1988.

7. Meier T. Rische, M. Endrun, B. Vafidis, A. Harjers H.-P., "*Seismicity of the Hellenic subduction zone in the area of western and central Crete observed by temporary local seismic networks* ", Tectonphysics, 383, 149-169, 2004.

8. R. Torres *et al.*, "*GMES Sentinel-1 missiom*", Remote Sens. Environ., vol 120, pp. 9-24, May 2012.

9. F. De Zan, A. Monti Guarnieri, "*TOPSAR: Terrain observation by progressive scan*", IEEE Trans. Geosci. Remote Sens., vol. 44, no. 9, pp. 2352-2360, Sep. 2006.

10. C.A Wiley, "*Pulsed Doppler radar methods and apparatus*", U.S. Patent 3.196.436, filed in 1954.

References

11. K. B. Katsaros, R. A. Brown, "*Legacy of the Seasat Mission for Studies of the Atmosphere and Air-Sea-Interactions*", BAMS (Bulletin of the American Meteorological Society), Volume 72, No 7, July 1991, pp. 967-981.

12. D. L. Evans, W. Alpers, A. Cazenave, C. Elachi, T. Farr, D. Glacking, B. Holt, L. Jones, W. Timothy Liu, W. McCandless, Y. Menard, R. Moore, Eni Njoku, "*Seasat – A 25-year legacy of success*", Remote sensing of Environment, Vol 94, No 3, Feb. 15, 2005, pp. 384-404, ISSN 0034-4257.

13. H. A. Zebker, R. M. Goldstein, "*Topographic mapping from synthetic aperture radar observations*", J. Geophys. Res., 91, 4993, 1986.

14. K. Gabriel, R. M. Goldstein, H. A. Zebker, "*Mapping small elevation changes over large areas: Differential interferometry*", J. Geophys., Res., 94, 1989.

15. J. Way, D. Evans, C. Elachi, "*The SIR-C/X-SAR mission*", Proceedings of IGARSS'93 (International Geoscience and Remote Sensing Symposium), Tokyo, Japan, Aug. 18-21, 1993, Vol 2.

16. S. D'Elia, S. Jutz, "*SAR Mission Planning for ERS-1 and ERS-2*", ESA Bulletin, No 90, May 1997.

17. A. Pope, G. Rees, A. J. Fox, A. H. Fleming, "*Open Access Data in Polar and Cryospheric Remote Sensing*", Remote Sensing 2015, 6, 6183-6220; doi:10.3390/rs6076183.

18. M. Daily, T. Bicknell, "*SAR squint analysis of directional extended targets*", Proc. Int. Geosci. Remote Sensing Symp., June 1981.

19. A. Freeman, "*SAR calibration: an overview*", IEEE Trans. Geosci. Remote Sensing, vol. 30, no. 6, pp. 1107-1121, November 1992.

20. G. Franceschetti, R. Lanari, "*Synthetic Aperture Radar Processing*", CRC PRESS, New York, 1999.

21. J. S. Curlander, R. McDonough, "*Synthetic Aperture Radar and Signal Processing*", New York, Wiley.

22. C. Elachi, "*Spaceborne radar remote sensing: applications and techniques*", Institute of Electrical and Electronics Engineers, 1998.

23. A. Moreira, P. Prats-Iraola, M. Younis, G. Krieger, I. Hajnsek, K. P. Papathanassiou, "*A tutorial on Synthetic Aperture Radar*", IEEE Geosc. And Remote Sensing Magazine, March 2013.

24. D. Massonnet, K. I. Feigl, "*Radar interferometry and its application to changes in the Earth's surface*", Rev. Geophys., vol 36, no. 4, pp. 441-500, 1998.

25. R. F. Hanssen, "*Radar Interferometry: Data Interpretation and Error Analysis*", The Netherlands: Kluwer, 2001.

26. Y. Dong, B. Fu, Y. Ninomiya, "*DEM generation methods and applications in revealing of topographic changes caused by coal mining activities*", ICEODPA, 2008

27. A. L. Gray, P. J. Farris-Manning, "*Repeat-pass interferometry with airborne synthetic aperture radar*", IEEE Trans, Geosci., Remote Sensing, vol. 31, no. 1, pp. 180-191, Jan. 1993.

28. J. Askne, J. O. Hagberg, "*Potential of interferometric SAR for classification of land surface*", in Proc. IEEE Int. Geoscience and Remote Sensing Symp. (IGARSS), Tokyo, 1993

29. S. R. Cloude, K. P. Papathanassiou, "*Polarimetric SAR interferometry*", IEEE Trans. Geosci. Remote Sensing, vol. 36, no.5, pp.1551-1565, Sept. 1998.

30. R. Romeiser, H. Breit, M. Eineder, H. Runge, P. Flament, J. de Karin, J. Vogelzang, "*Current measurements by SAR along-track interferometry from a space shuttle*", IEEE Trans. Geosci. Remote Sensing, vol 43, no. 10, pp. 2315-2324, 1995.

31. E. Rodriguez, J. Martin, "*Theory and design of interferometric synthetic aperture radars*", Radar and Signal Processing, IEE Proc. F (1988-1993), vol. 139, no. 2, pp. 147-159, 1992.

32. P. A. Rosen, S. Hensley, I. R. Joughin, F. K. Li, S. N. Madsen, E. Rodriguez, R. M. Goldstein, "*Synthetic aperture radar interferometry*, Proc. IEEE, vol. 88, no. 3, pp. 333-382, Mar. 2000

33. R. Bamler, P. Hartl, "*Synthetic aperture radar interferometry*", Inverse Problems, vol. 14, pp. R1-R54, Aug. 1998.

34. Zebker, J. Villasenor, "*Decorrelation in interferometric radar echoes*", IEEE Trans., 30, pp. 950-959, 1992.

35. D. P. Schwartz, K. J. Coppersmith, "*Fault behavior and characteristic earthquakes: Examples from the Wasatch and San Andreas Fault Zones*", J. Geophys. Res., 89(B7), pp. 5681-5698, 1984.

36. A. K. Gabriel, R. M. Goldstein, H. A. Zebker, "*Mapping small elevation changes over large areas: Differential radar interferometry*", J. Geophys. Res., 94(B7), pp. 9183-9191, 1989.

37. R. Michel, J. P. Avouac, J. Taboury, "*Measuring ground displacements from SAR amplitude images: Application to the Landers Earthquake*", J. Geophys. Res., 26(B7), pp. 875-878, 1999.

38. A. Ferretti, C. Prati, F. Rocca, "*Permanent scatterers in SAR interferometry*", IEEE Trans. On geoscience and remote sens., 38 (5), pp. 2202-2212, 2000.

39. R. Lanari, O. Mora, M. Manunta, J. J. Mallorqui, P. Berardino, E. Sansosti, "*A small Baseline Approach for Investigating Deformations on Full Resolution Differential SAR Interferograms*", IEEE Transaction on Geoscience and remote sens. 42 (7), 2004.

40. S. Usai, "*A Least Squares Database Approach for SAR Interferometric Data*", IEEE Transaction on Geoscience and remote sens., 41 (4), pp. 2243-2253, 2003.

41. N. Yague-Martinez, P. Prats-Iraola, F. R. Gonzalez, R. Brcic, D. Geudtner, M. Eineder, R. Bamler, "*Interferometric Processing of Sentinel-1 TOPS Data*", IEEE Transaction on Geoscience and remote sens., 54 (4), pp. 2220-2234, 2016.

42. A. Pepe, A. B. Ortiz, P. R. Lundgren, P. A. Rosen, R. Lanari, "*The Stripmap-ScanSAR SBAS Approach to fill gaps in STRIPMAP Deformation Time Series with ScanSAR Data*", IEEE Transaction on Geoscience and remote sens., 49 (12), pp. 4788-4804, 2011.

43. P. Prats-Iraola, R. Scheiber, L. Marotti, S. Wollstadt, A. Reigber, "*TOPS Interferometry with TerraSAR-X*", IEEE Transactions on Geoscience and remote sensing, 50(8), pp. 3179-3188, 2012.

44. A. M. Guarnieri, S. Mancon, S. Tebaldini, *"Sentinel-1 precise orbit calculation and validation"*, Conference Proceedings, 2015.

45. M. Bara, R. Schreiber, A. Broquetas, *"Interferometric SAR signal analysis in the presence of squint"*, Proc. IEEE IGARSS, 1, pp. 2179-2191, Sep. 2000.

46. R. M. Goldstein, C. L. Werner, *"Radar interferogram filter for geophysical application"*, Geophysical Research Letters, vol. 25, pp. 4035-4038, 1998.

47. R. M Goldstein, H. A. Zebker, C. L. Werner, *"Satellite radar interferometry: two-dimensional phase unwrapping "*, Radio Sci. vol. 23, 1988.

48. G. Fornaro, G. Franceschetti, R. Lanari, *"Interferometric SAR Phase Unwrapping Using Green's Formulation"*, IEEE Trans. Geosci. Remote Sens., 34, 1996.

49. D. C. Ghiglia, M. D. Pritt, *"Two-Dimensional Phase Unwrapping: Theory, Algorithms and Software"*, John Wiley and Sons, New York, 1998.

50. M. Constantini and P. Rosen, *"A generalized phase unwrapping approach for sparse data"*, In Proc. Int. Geoscience and Remote Sensing Symposium, Hamburg, Germany, 1999.

51. A. Pepe, A. B. Ortiz, P. R. Lundgren, P. A. Rosen, R. Lanari, *"The Stripmap-ScanSAR SBAS Approach to Fill Gaps in Stripmap Deformation Time Series with ScanSAR Data"*, IEEE Transaction on Geoscienc and Rem. Sens., vol 49 (12), pp. 4788-4804, 2011.

52. G. Schreier, *"SAR Geocoding-Data System"*, Karlshrue, Wichmann, 1993.

53. O. O. Bezvesilniy, I. Gorovyi, V. Vinogradov, D. M. Vavriv, *"Range-Doppler Algorithm with Extended Number of Looks"*, Conference: Microwave Radar Rem. Sens. Sump., 2011.

54. I. Gorovyi, O. O. Bezvesilniy, D. M. Vavriv, *"Modifications of Range-Doppler Algorithm for Compensation of SAR Platform Motion Instabilities"*, INTL. Journal of Electr. And Telec., vol 60 (3), pp. 225-231, 2014.

55. W. G. Carrara, R. S. Goodman, R. M. Majewski, *"Spotlight Synthetic Aperture Radar: Signal Processing Algorithms"*, Boston; London, Artech House, 1995.

56. N. D. Cagatay, M. Datcu, *"FrFT-Based Scene Classification of Phase-Gradient InSAR Images and Effective Baseline Dependence"*, IEEE Geoscience and Rem. Sens. Letters, vol. 12, pp. 1131-1135, 2015.

57. R. H. Hudgin, *"Wave-front reconstruction for compensated imaging"*, Journal Opt. Soc. Amer., vol 67, pp. 375-378, Mar. 1977.

58. B. R. Hunt, *"Matrix formulation of the reconstruction of phase-values from phase differences"*, Journal Opt. Soc. Amer., vol. 69, pp. 393-399, Mar. 1979.

59. D.C. Ghiglia, L. A. Romero, *"Robust two-dimensional weighted and unweighted phase unwrapping that uses fast transforms and iterative methods"*, J. Opt. Soc. Am. A 11, pp. 107-11, 1994.

60. H. A. Zebker, Y. Lu, *"Phase unwrapping algorithms for radar interferometry: residue-cut, least-squares and synthesis algorithms"*, J. Opt. Soc. Am. A, vol.15, pp. 586-598, 1998.

61. M. Costantini, *"A Novel Phase Unwrapping Method Based on Network Programming"*, IEEE Transactions on Geoscience and Rem. Sens., vol. 36 (3), pp. 813-821, 1998.

62. S. Karout, M. Gdeisat, D. R. Burton, M. J. Lalor, *"Two-dimensional phase unwrapping using a hybrid genetic algorithm"*, Applied optics, vol. 46, pp. 730-743, 2007.

63. G. Yao, J. Duan, J. Mu, *"A new Algorithm of Phase Unwrapping"*, Proceedings of the 2006 Intern. Conf. on Image Processing, vol. 1, pp. 314-320, 2006.

64. P. Berardino, G. Fornaro, R. Lanari, E. Sansosti, *"A New Algorithm for Surface Deformation Monitoring based on Small Baseline Differential SAR Interferograms"*, IEEE Transactions on Geoscience and Rem. Sens., vol 40 (11), pp. 2375-2383.

65. A. Hooper, H. Zebker, P. Segall, B. Kampes, *"A new method for measuring deformation on volcanoes and other natural terrains using InSAR persistent Scatterers"*, Geophys. Res. Lett., vol. 31, 2004.

66. A. Ferretti, C. Prati, F. Rocca, *"Permanent scatterers in SAR interferometry"*, IEEE Transaction on Geoscience and Remote Sensing, vol 39 (1), pp. 8-20, 2001.

67. O. Mora, J. J. Mallorqui, A. Broquetas, *"Linear and Nonlinear Terrain Deformation Maps from a reduced set of Interferometric SAR images"*, IEEE Transaction on Geoscience and Remote Sensing, vol. 41 (10), pp. 2243-2253, 2003.

68. B. M. Kampes, N. Adam, *"The STUN algorithm for Persistent scatterer interferometry"*, Fringe 2005 Workshop, Frascati, Italy.

69. J. Neelmeijer, T. Schone, R. Dill, V. Klemann, M. Motagh, *"Ground Deformations around the Toktogul Reservoir, Kyrgyzstan, from Envisat ASAR and Sentinel-1 Data – A case study about the impact of Atmospheric Corrections on InSAR time-series"*, Remote Sensing, 10, 462, 2018.

70. E. Cabral-Cano, B. Osmanoglu, T. Dixon, S. Wdowinski, C. DeMets, F. Cigna, O. Diaz-Molina, *"Subsidence and fault hazard maps using PSI and permanent GPS networks in central Mexico"*, In Proceedings of the Eighth International Symposium of Land Subsidence, Queretaro, Mexico, pp. 17-22, 17-22 October 2010.

Unwrapped Interferograms

June 2017 - July 2017
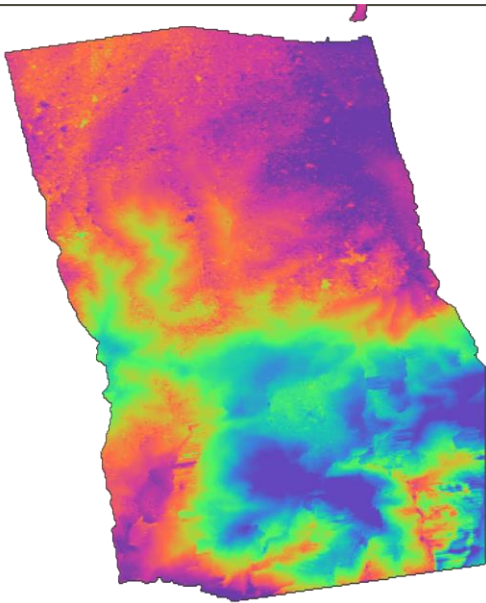
June 2017 - August 2017
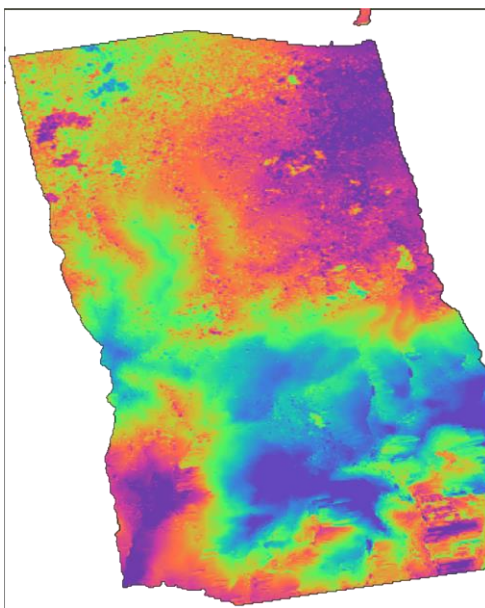

June 2017 - October 2017
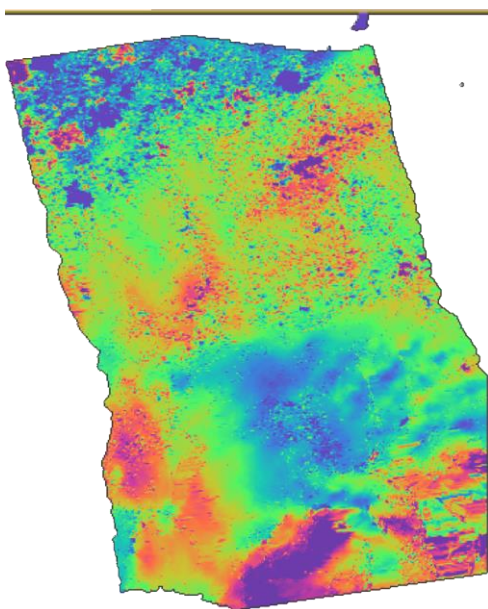
July 2017 - September 2017
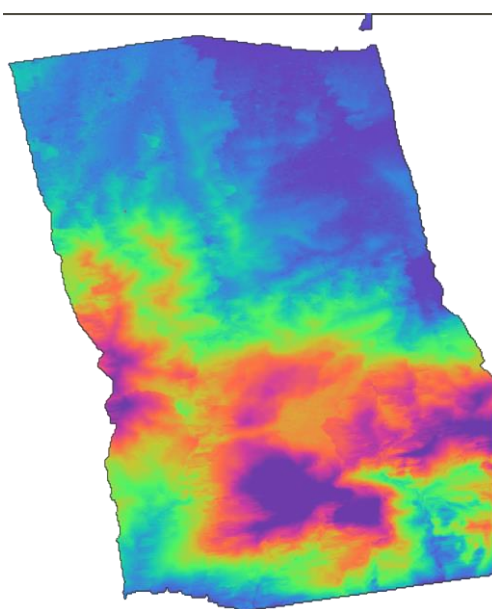
July 2017 - October 2017
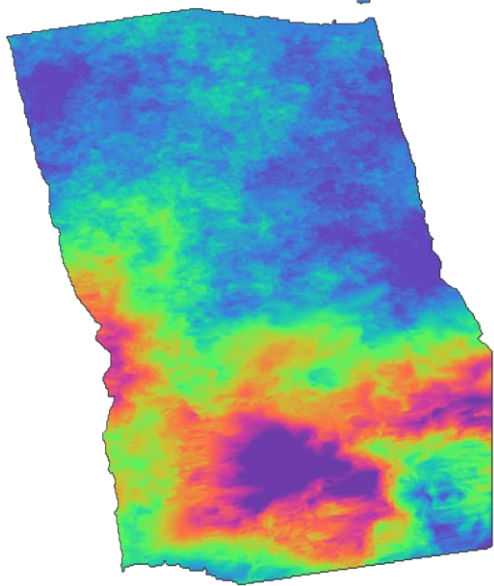
August 2017 - October 2017
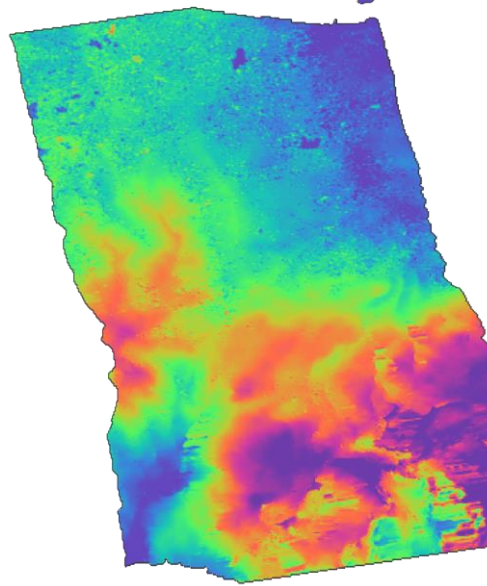
August 2017 - November 2017
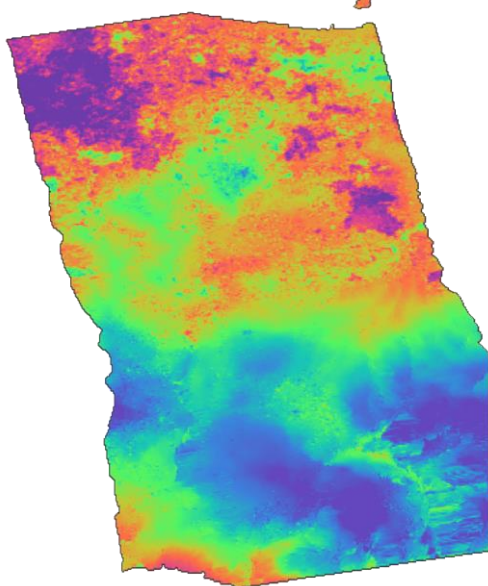
September 2017 - October 2017
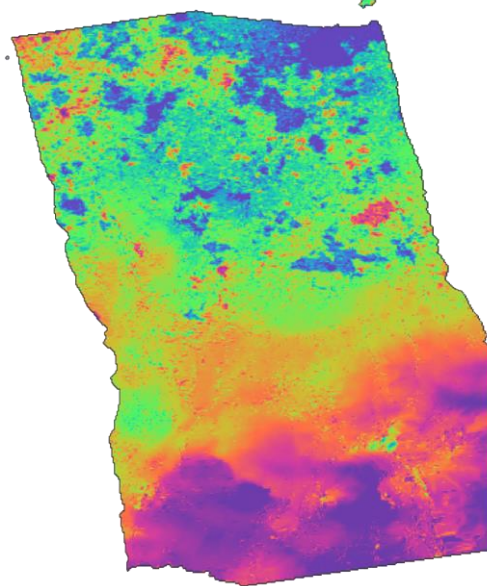
September 2017 - December 2017
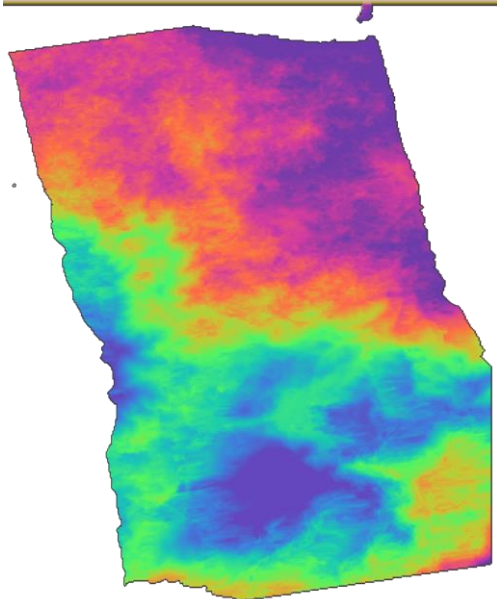
8 October 2017 - November 2018
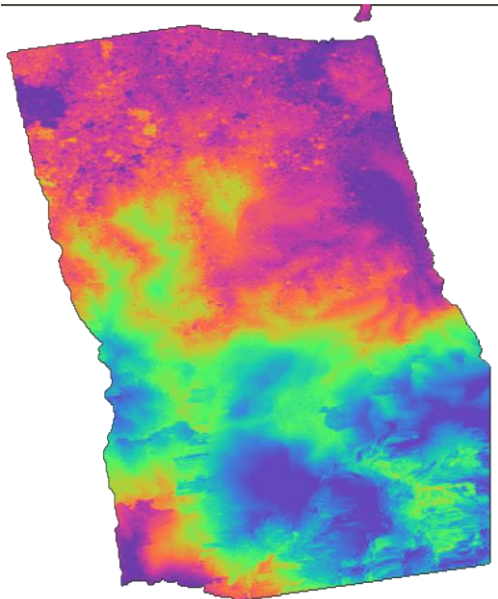
8 October 2017 - January 2018
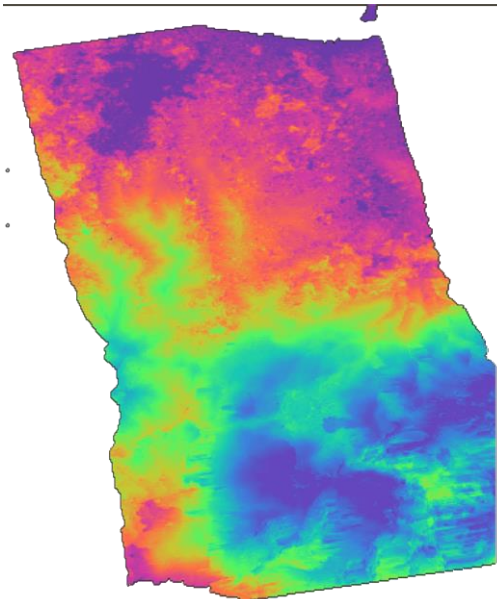
26 October 2017 – December 2017
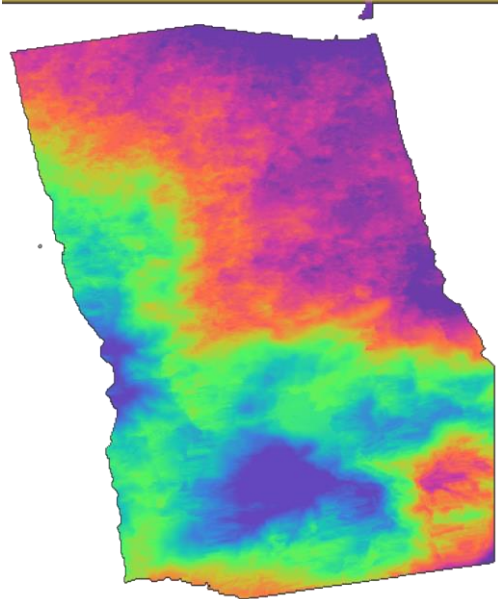
26 October 2017- February 2018
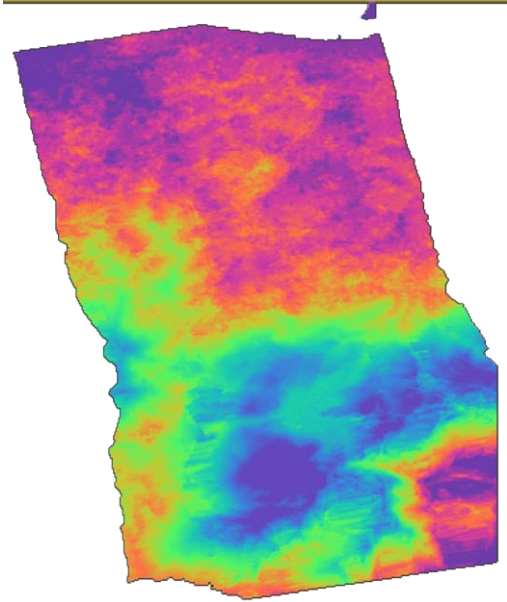
November 2017 – December 2018
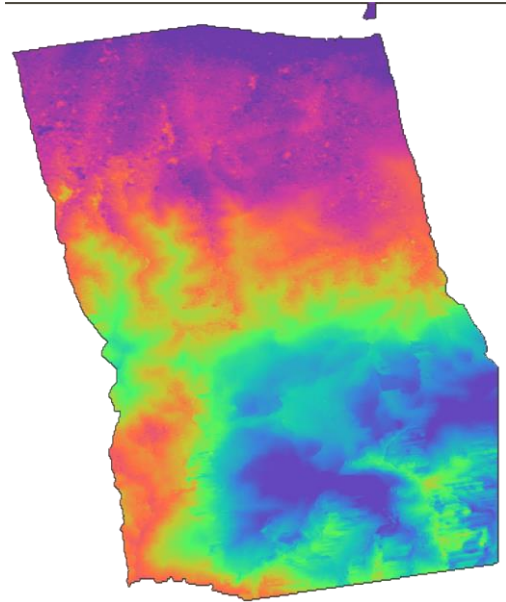
November 2017 – January 2018
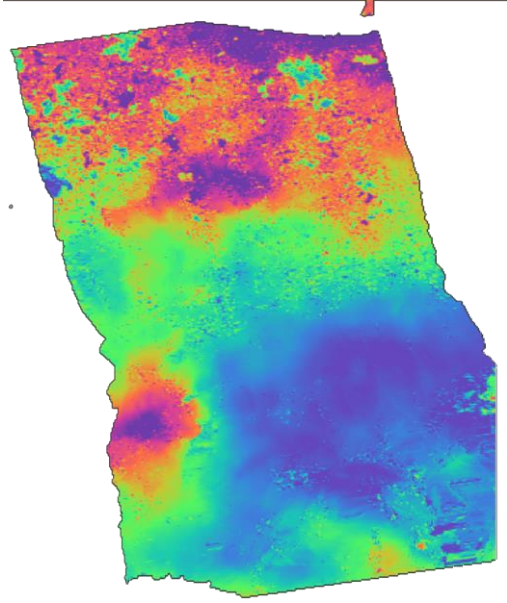
November 2017 – March 2018
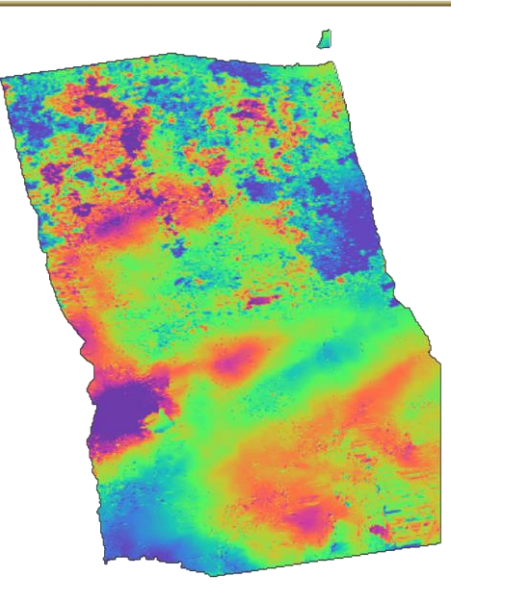
December 2017- February 2018
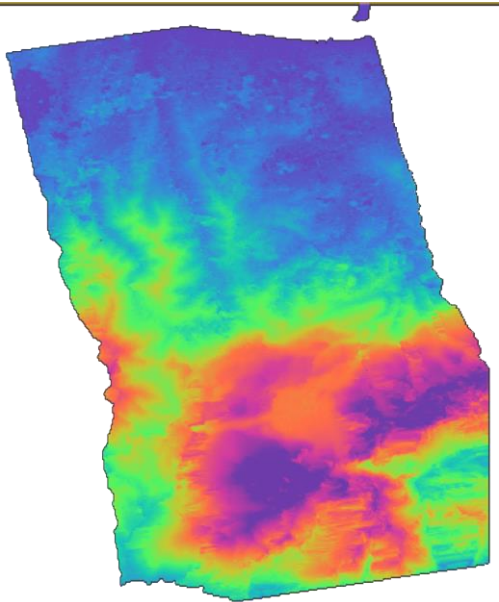
December 2017 – April 2018
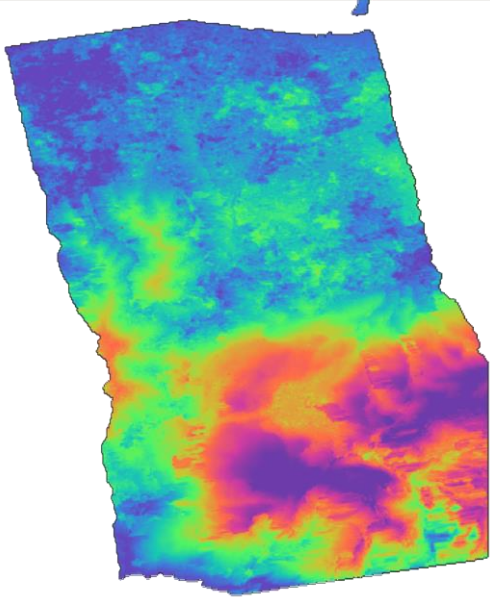
January 2018 – February 2018
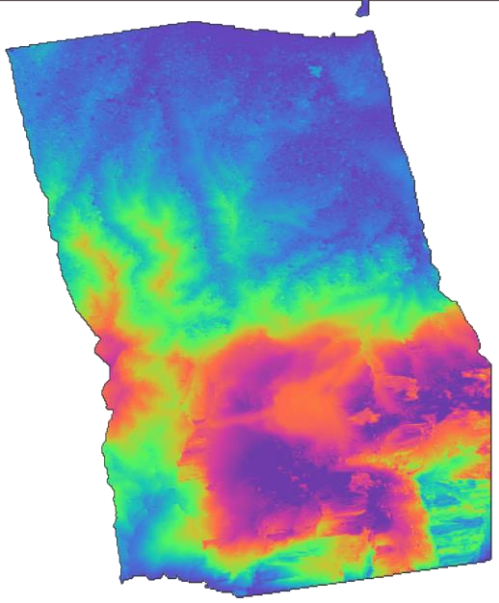
January 2018 – March 2018
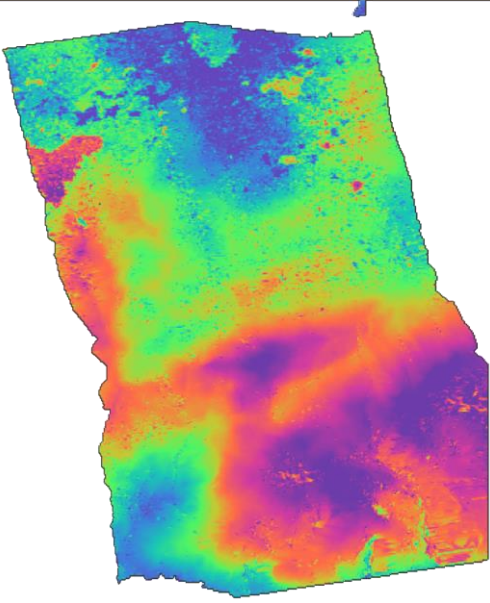
January 2018 – May 2018
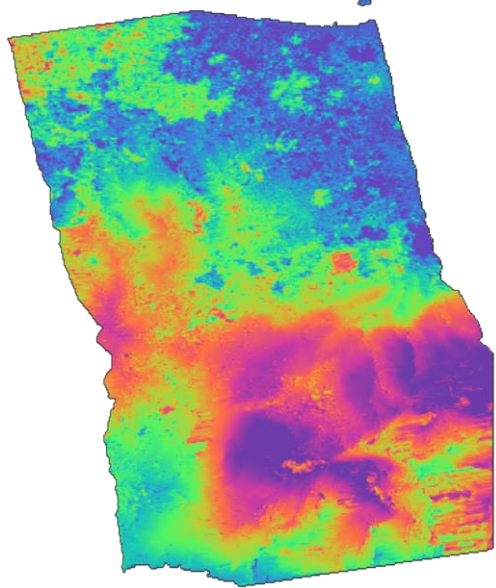
February 2018 – April 2018
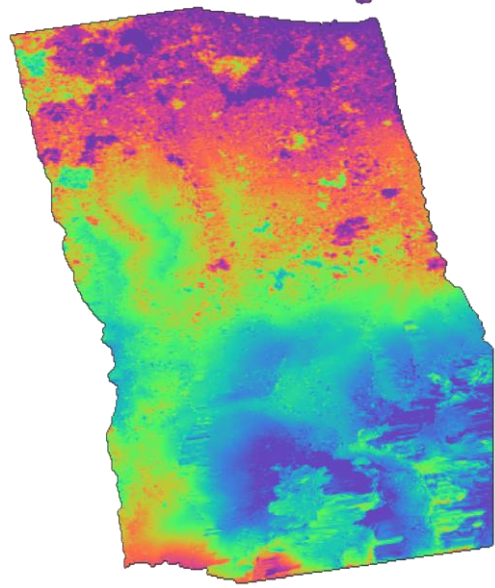
February 2018 – June 2018
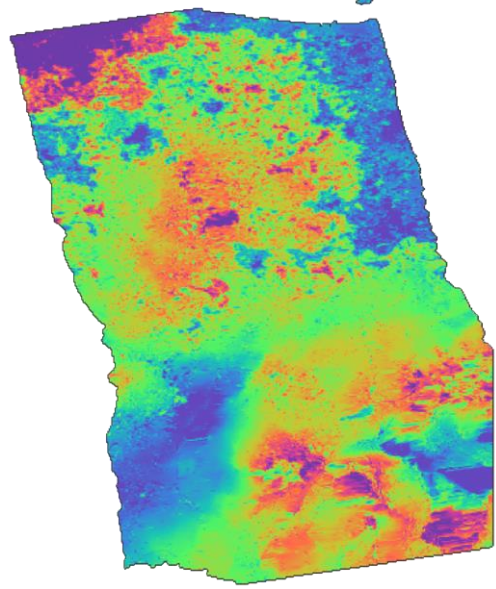
March 2018 – December 2017
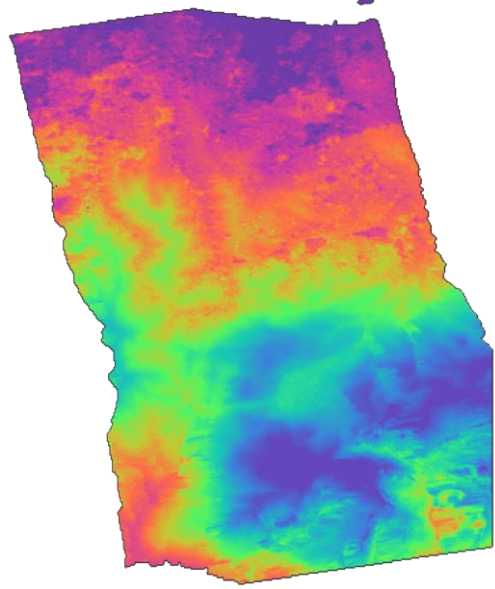
March 2018 – May 2018
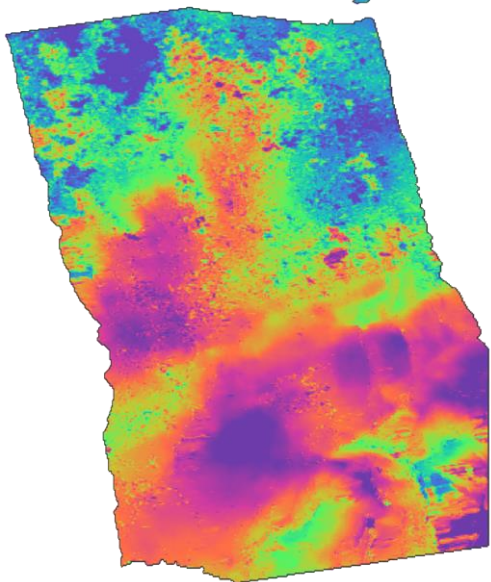
March 2018 – July 2018
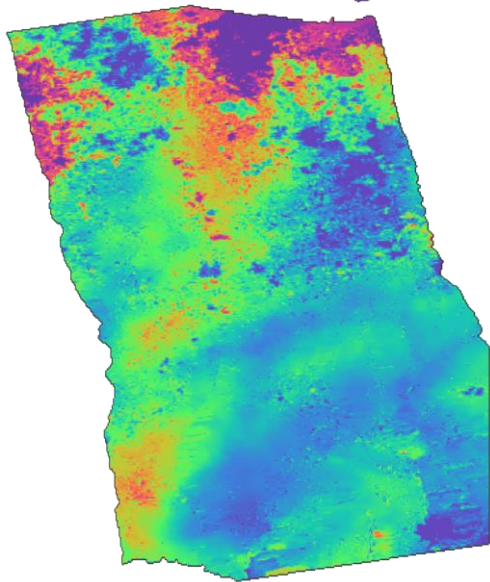
April 2018 – August 2018
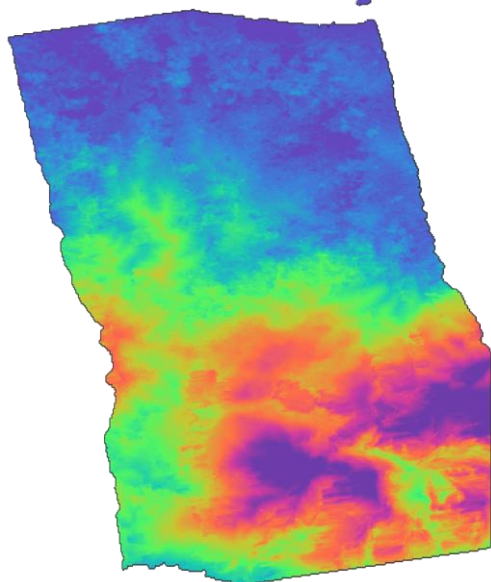
May 2018 -July 2018
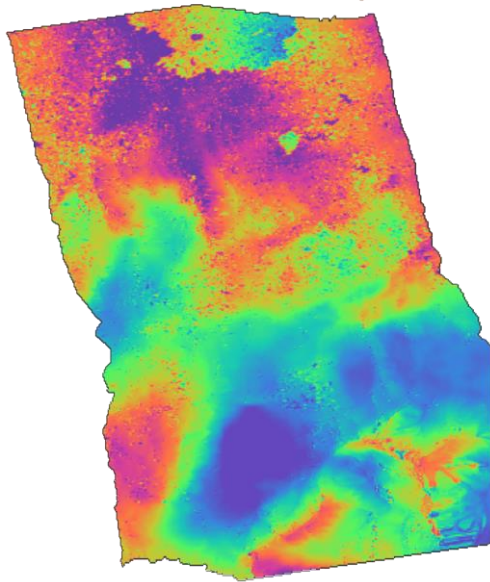
May 2018 – September 2018
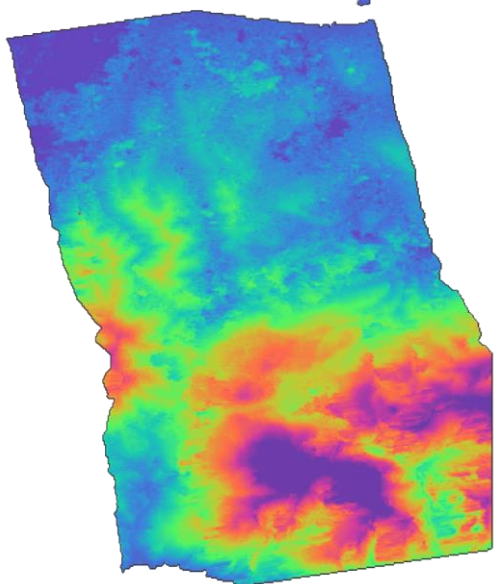
June 2018 - August 2018
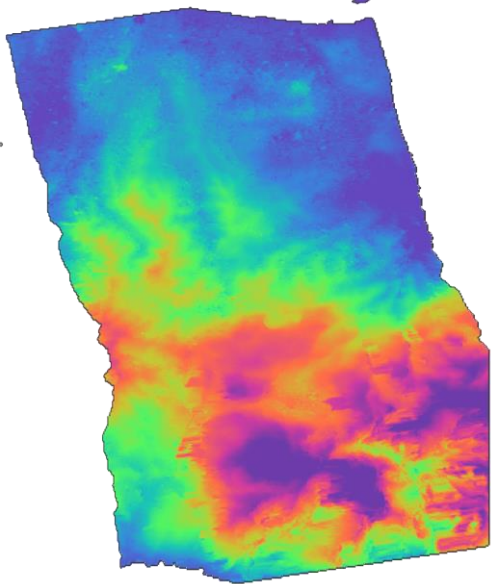
June 2018 – October 2018
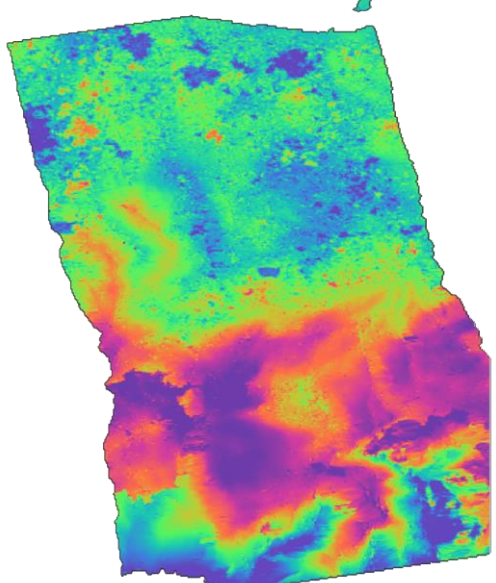
July 2018 – September 2018
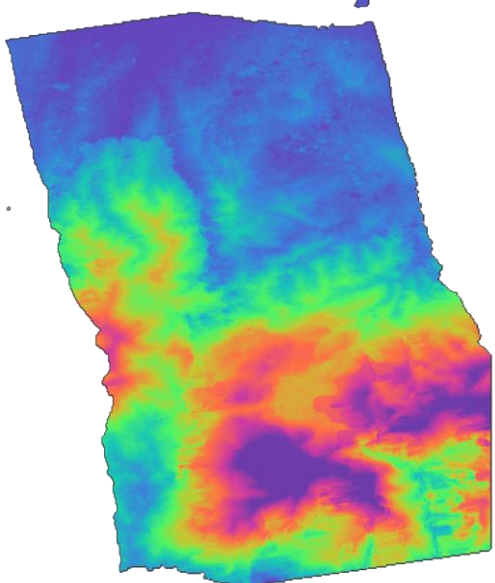
July 2018 – November 2018
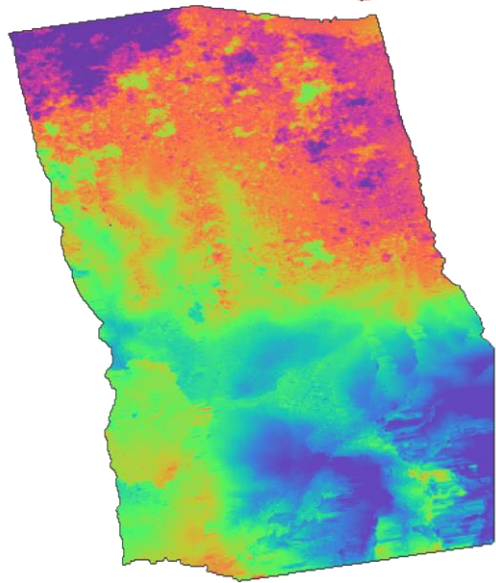
August 2018 – October 2018
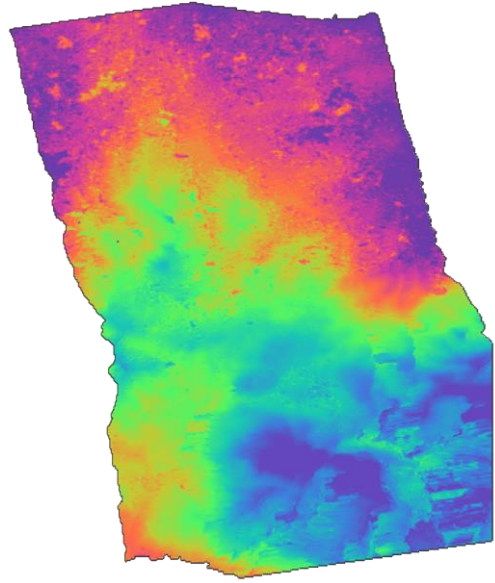
August 2018 – November 2018
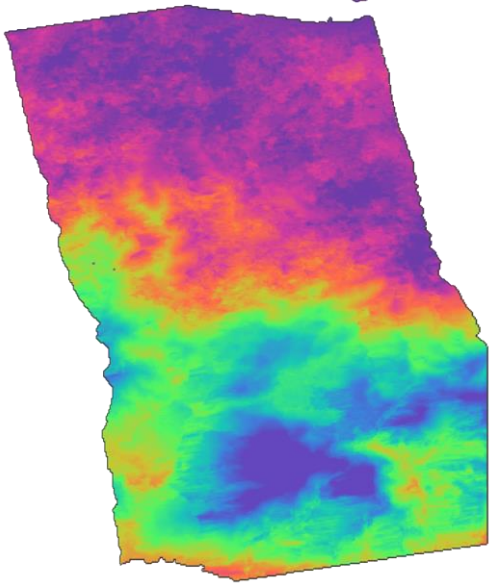
August 2018 – December 2018
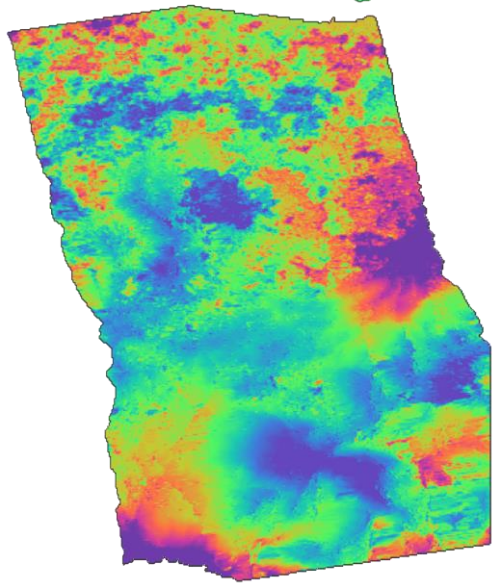
September 2018 – November 2018
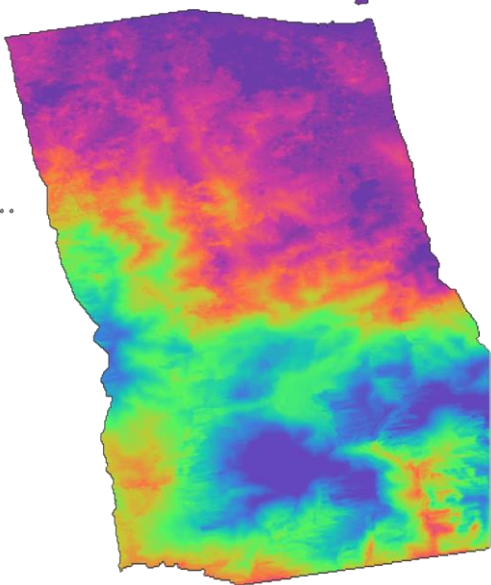
October 2018 – September 2018
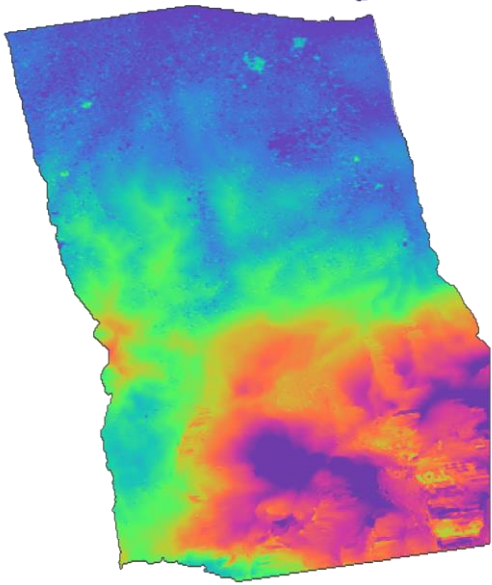
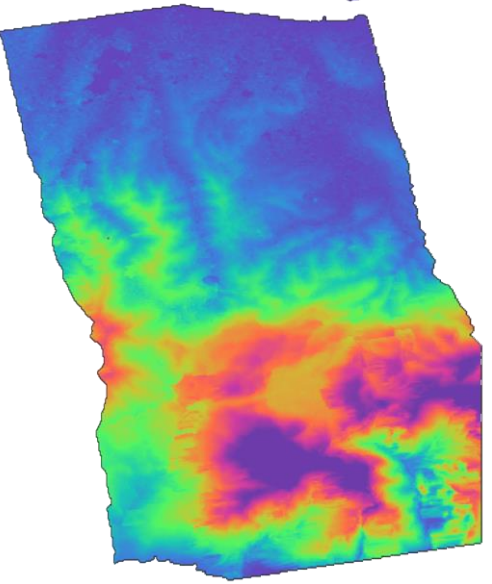## October 2018 - December 2018
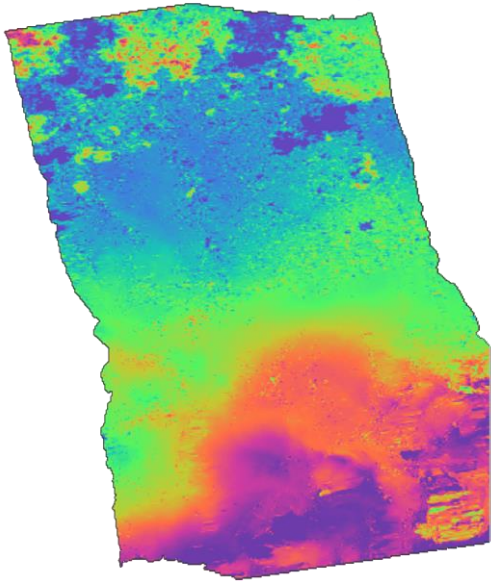
November 2018 – October 2018
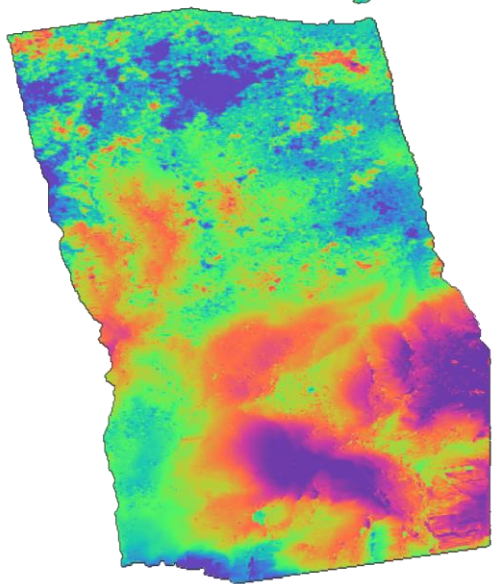
December 2018 – September 2018   December 2018 – November 2018